

The Molecular Biophysics of Evolutionary and Physiological Adaptation

Thesis by
Griffin Daniel Chure

In Partial Fulfillment of the Requirements for the
Degree of
Doctor of Philosophy in Biochemistry and Molecular Biophysics

The Caltech logo, consisting of the word "Caltech" in a bold, orange, sans-serif font.

CALIFORNIA INSTITUTE OF TECHNOLOGY
Pasadena, California

2020
Defended June 1, 2020

© 2020

Griffin Daniel Chure
ORCID: 0000-0002-2216-2057

Some rights reserved. This thesis is distributed under a Creative Commons
Attribution License CC-BY 4.0.

ACKNOWLEDGEMENTS

This is a placeholder file to not release the real acknowledgements into the world too early

ABSTRACT

This is a test abstract file.

PUBLISHED CONTENT AND CONTRIBUTIONS

Chure, G., Kaczmarek, Z.A., and Phillips, R. (2019b). Physiological Adaptability and Parametric Versatility in a Simple Genetic Circuit. *BioRxiv* 2019.12.19.878462.

Hirokawa, S., Chure, G., Belliveau, N.M., Lovely, G.A., Anaya, M., Schatz, D.G., Baltimore, D., and Phillips, R. (2019). Sequence-Dependent Dynamics of Synthetic and Endogenous RSSs in V(D)J Recombination. *BioRxiv* 791954.

Chure, G., Razo-Mejia, M., Belliveau, N.M., Einav, T., Kaczmarek, Z.A., Barnes, S.L., and Phillips, R. (2019a). Predictive Shifts in Free Energy Couple Mutations to Their Phenotypic Consequences. *Proceedings of the National Academy of Sciences* 116.

Phillips, R., Belliveau, N.M., Chure, G., Garcia, H.G., Razo-Mejia, M., and Scholes, C. (2019). Figure 1 Theory Meets Figure 2 Experiments in the Study of Gene Expression. *Annu. Rev. Biophys.* 48, 121–163.

Chure, G.* , Lee, H.J.* , Rasmussen, A., and Phillips, R. (2018). Connecting the Dots between Mechanosensitive Channel Abundance, Osmotic Shock, and Survival at Single-Cell Resolution. *Journal of Bacteriology* 200. * contributed equally

Razo-Mejia, M.* , Barnes, S.L.* , Belliveau, N.M.* , Chure, G.* , Einav, T.* , Lewis, M., and Phillips, R. (2018). Tuning Transcriptional Regulation through Signaling: A Predictive Theory of Allosteric Induction. *Cell Systems* 6, 456-469.e10. * contributed equally

TABLE OF CONTENTS

Acknowledgements	iii
Abstract	iv
Published Content and Contributions	v
Table of Contents	vi
List of Illustrations	vii
List of Tables	viii
Chapter I: Kneel Before the Janus-Faced Protein: Adaptive Processes Across The Biological Scales	1
1.1 Introduction	1
Chapter II: Through the Intramolecular Grape Vine: Signal Processing Via Allosteric Transcription Factors	2
2.1 Introduction	2
2.2 Theoretical Model	4
2.3 Results	9
2.4 Discussion	18
2.5 Methods	22
2.6 Data Curation	27
2.7 References	27
Chapter III: Unknown Knowns, Known Unknowns, and Unforeseen Conse- quences: Using Free Energy Shifts To Predict Mutant Phenotypes	28
3.1 Introduction	28
3.2 Theoretical Model	29
3.3 Results	34
3.4 Discussion	44
3.5 References	53
Chapter IV: Ignorance Is Bliss: Physiological Adaptability of a Simple Ge- netic Circuit	54
4.1 Introduction	54
Chapter V: 'Water, Water Everywhere, Nor Any Drop to Drink': How Bacte- ria Adapt To Changes in Osmolarity	57
5.1 Introduction	57
5.2 Results	59
5.3 Discussion	69
5.4 Materials & Methods	73
5.5 Acknowledgements	80
References	86
Chapter VI: Questionnaire	96
Chapter VII: Consent Form	97

LIST OF ILLUSTRATIONS

<i>Number</i>	<i>Page</i>
2.1 Transcriptional regulatory architectures involving an allosteric repressor.	5
2.2 States and statistical weights for the simple repression motif.	7
2.3 An experimental pipeline for high-throughput fold-change measurements.	12
2.4 Predicting induction profiles for different biological control parameters.	14
2.5 Comparison of predictions against measured and inferred data.	15
2.6 Predictions and experimental measurements of key properties of induction profiles.	17
3.1 Summary of Chapter 2. A predictive framework for dissection of the simple repression motif	31
3.2 Parametric changes due to mutations and their corresponding free-energy shifts.	35
3.3 Induction profiles and free-energy differences of DNA binding domain mutations in the <i>lac</i> repressor.	38
3.4 Induction profiles and free-energy differences of inducer binding domain mutants.	41
3.5 Induction and free-energy profiles of DNA binding and inducer binding double mutants.	45
5.1 Role of mechanosensitive channels during hypo-osmotic shock.	60
5.2 Control of MscL expression and calculation of channel copy number.	63
5.3 Experimental approach to measuring survival probability	64
5.4 Distributions of survival and death as a function of effective MscL channel number.	65
5.5 Probability of survival as a function of MscL copy number.	68

LIST OF TABLES

Chapter 1

KNEEL BEFORE THE JANUS-FACED PROTEIN: ADAPTIVE PROCESSES ACROSS THE BIOLOGICAL SCALES

1.1 Introduction

Chapter 2

THROUGH THE INTRAMOLECULAR GRAPE VINE: SIGNAL PROCESSING VIA ALLOSTERIC TRANSCRIPTION FACTORS

A version of this chapter originally appeared as Razo-Mejia, M.* , Barnes, S.L.* , Belliveau, N.M.* , Chure, G.* , Einav, T.* , Lewis, M., and Phillips, R. (2018). Tuning Transcriptional Regulation through Signaling: A Predictive Theory of Allosteric Induction. *Cell Systems* 6, 456-469.e10. M.R.M, S.L.B, N.M.B, G.C., and T.E. contributed equally to this work from the theoretical underpinnings to the experimental design and execution. M.R.M, S.L.B, N.M.B, G.C, T.E., and R.P. wrote the paper. M.L. provided extensive guidance and advice.

2.1 Introduction

Understanding how organisms sense and respond to changes in their environment has long been a central theme of biological inquiry. At the cellular level, this interaction is mediated by a diverse collection of molecular signaling pathways. A pervasive mechanism of signaling in these pathways is allosteric regulation, in which the binding of a ligand induces a conformational change in some target molecule, triggering a signaling cascade (Lindsley and Rutter, 2006). One of the most important examples of such signaling is offered by transcriptional regulation, where a transcription factor's propensity to bind to DNA will be altered upon binding to an allosteric effector.

Despite allostery's ubiquity, we lack a formal, rigorous, and generalizable framework for studying its effects across the broad variety of contexts in which it appears. A key example of this is transcriptional regulation, in which allosteric transcription factors can be induced or corepressed by binding to a ligand. An allosteric transcription factor can adopt multiple conformational states, each of which has its own affinity for the ligand and for its DNA target site. *In vitro* studies have rigorously quantified the equilibria of different conformational states for allosteric transcription factors and measured the affinities of these states to the ligand (Harman, 2001; Lanfranco et al., 2017). In spite of these experimental observations, the lack of a coherent quantitative model for allosteric transcriptional regulation has made it impossible to predict the behavior of even a simple genetic circuit across a range of regulatory parameters.

The ability to predict circuit behavior robustly—that is, across both broad ranges of parameters and regulatory architectures—is important for multiple reasons. First, in the context of a specific gene, accurate prediction demonstrates that all components relevant to the gene’s behavior have been identified and characterized to sufficient quantitative precision. Second, in the context of genetic circuits in general, robust prediction validates the model that generated the prediction. Possessing a validated model also has implications for future work. For example, when we have sufficient confidence in the model, a single data set can be used to accurately extrapolate a system’s behavior in other conditions. Moreover, there is an essential distinction between a predictive model, which is used to predict a system’s behavior given a set of input variables, and a retroactive model, which is used to describe the behavior of data that has already been obtained. We note that even some of the most careful and rigorous analysis of transcriptional regulation often entails only a retroactive reflection on a single experiment. This raises the fear that each regulatory architecture may require a unique analysis that cannot carry over to other systems, a worry that is exacerbated by the prevalent use of phenomenological functions (e.g. Hill functions or ratios of polynomials) that can analyze a single data set but cannot be used to extrapolate a system’s behavior in other conditions (Poelwijk et al., 2011; Rogers et al., 2015; Rohlhill et al., 2017; Setty et al., 2003; Vilar and Saiz, 2013).

This work explores what happens when theory takes center stage, namely, we first write down the equations governing a system and describe its expected behavior across a wide array of experimental conditions, and only then do we set out to experimentally confirm these results. Building upon previous work (Brewster et al., 2014; Garcia and Phillips, 2011; Weinert et al., 2014) and the work of Monod, Wyman, and Changeux (Monod et al., 1965), we present a statistical mechanical rendering of allosteric regulation in the context of induction and corepression (shown schematically in Fig. 2.1 and henceforth referred to as the MWC model) and use it as the basis of parameter-free predictions which we then test experimentally. More specifically, we study the simple repression motif—a widespread bacterial genetic regulatory architecture in which binding of a transcription factor occludes binding of an RNA polymerase, thereby inhibiting transcription initiation. The MWC model stipulates that an allosteric protein fluctuates between two distinct conformations—an active and inactive state—in thermodynamic equilibrium (Monod et al., 1965). During induction, for example, effector binding increases the probability that a repressor will be in the inactive state, weakening its ability to bind

to the promoter and resulting in increased expression. To test the predictions of our model across a wide range of operator binding strengths and repressor copy numbers, we design an *E. coli* genetic construct in which the binding probability of a repressor regulates gene expression of a fluorescent reporter.

In total, the work presented here demonstrates that one extremely compact set of parameters can be applied self-consistently and predictively to different regulatory situations including simple repression on the chromosome, cases in which decoy binding sites for repressor are put on plasmids, cases in which multiple genes compete for the same regulatory machinery, cases involving multiple binding sites for repressor leading to DNA looping, and induction by signaling (Boedicker et al., 2013a, 2013b; Brewster et al., 2012, 2014; Garcia and Phillips, 2011; Garcia et al., 2011). Thus, rather than viewing the behavior of each circuit as giving rise to its own unique input-output response, the MWC model provides a means to characterize these seemingly diverse behaviors using a single unified framework governed by a small set of parameters.

2.2 Theoretical Model

Inducible Transcriptional Repression Via The MWC Model of Allostery

We begin by considering a simple repression genetic architecture in which the binding of an allosteric repressor occludes the binding of RNA polymerase (RNAP) to the DNA (Ackers and Johnson, 1982; Buchler et al., 2003). When an effector (hereafter referred to as an “inducer” for the case of induction) binds to the repressor, it shifts the repressor’s allosteric equilibrium towards the inactive state as specified by the MWC model (Monod et al., 1965). This causes the repressor to bind more weakly to the operator, which increases gene expression. Simple repression motifs in the absence of inducer have been previously characterized by an equilibrium model where the probability of each state of repressor and RNAP promoter occupancy is dictated by the Boltzmann distribution (Ackers and Johnson, 1982; Bintu et al., 2005a; Brewster et al., 2014; Buchler et al., 2003; Garcia and Phillips, 2011; Vilar and Leibler, 2003) [we note that non-equilibrium models of simple repression have been shown to have the same functional form that we derive below (Phillips, 2015)]. We extend these models to consider allostery by accounting for the equilibrium state of the repressor through the MWC model.

Thermodynamic models of gene expression begin by enumerating all possible states of the promoter and their corresponding statistical weights. As shown in

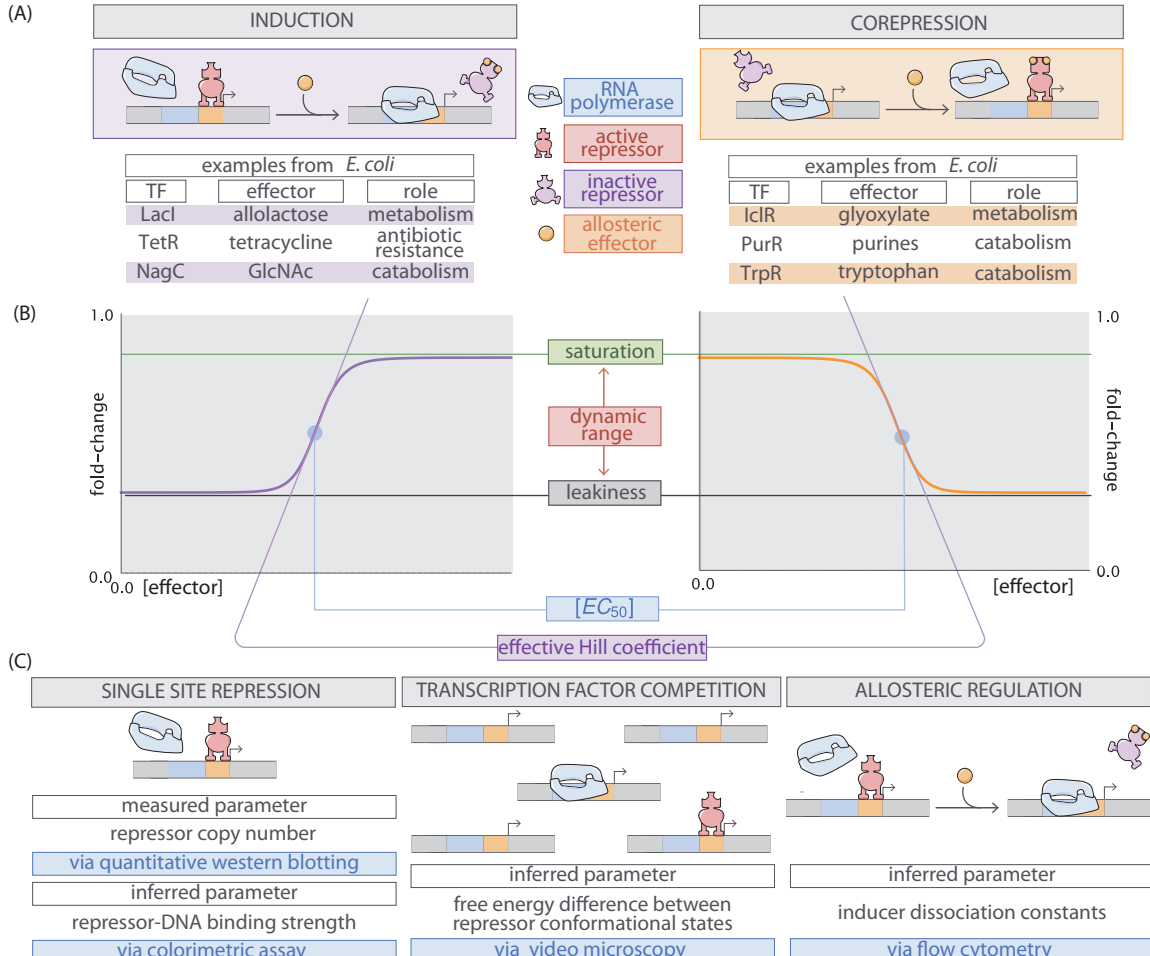


Figure 2.1: We consider a promoter regulated solely by an allosteric repressor. When bound, the repressor prevents RNAP from binding and initiating transcription. Induction is characterized by the addition of an effector which binds to the repressor and stabilizes the inactive state (defined as the state which has a low affinity for DNA), thereby increasing gene expression. In corepression, the effector stabilizes the repressor's active state and thus further reduces gene expression. We list several characterized examples of induction and corepression that support different physiological roles in *E. coli*. A schematic regulatory response of the two architectures shown in Panel plotting the fold-change in gene expression as a function of effector concentration, where fold-change is defined as the ratio of gene expression in the presence versus the absence of repressor. We consider the following key phenotypic properties that describe each response curve: the minimum response (leakiness), the maximum response (saturation), the difference between the maximum and minimum response (dynamic range), the concentration of ligand which generates a fold-change halfway between the minimal and maximal response ($[EC_{50}]$), and the log-log slope at the midpoint of the response (effective Hill coefficient). (C) Over time we have refined our understanding of simple repression architectures. A first round of experiments used colorimetric assays and quantitative Western blots to investigate how single-site repression is modified by the repressor copy number and repressor-DNA binding energy. A second round of experiments used video microscopy to probe how the copy number of the promoter and presence of competing repressor binding sites affect gene expression, and we use this data set to determine the free energy difference between the repressor's inactive and active conformations. Here we used flow cytometry to

Fig. 2.2 (A), the promoter can either be empty, occupied by RNAP, or occupied by either an active or inactive repressor. The probability of binding to the promoter will be affected by the protein copy number, which we denote as P for RNAP, R_A for active repressor, and R_I for inactive repressor. We note that repressors fluctuate between the active and inactive conformation in thermodynamic equilibrium, such that R_A and R_I will remain constant for a given inducer concentration (Monod et al., 1965). We assign the repressor a different DNA binding affinity in the active and inactive state. In addition to the specific binding sites at the promoter, we assume that there are N_{NS} non-specific binding sites elsewhere (i.e. on parts of the genome outside the simple repression architecture) where the RNAP or the repressor can bind. All specific binding energies are measured relative to the average non-specific binding energy. Thus, $\Delta\epsilon_P$ represents the energy difference between the specific and non-specific binding for RNAP to the DNA. Likewise, $\Delta\epsilon_{RA}$ and $\Delta\epsilon_{RI}$ represent the difference in specific and non-specific binding energies for repressor in the active or inactive state, respectively.

Thermodynamic models of transcription (Ackers and Johnson, 1982; Bintu et al., 2005a, 2005b; Brewster et al., 2014; Buchler et al., 2003; Daber et al., 2011; Garcia and Phillips, 2011; Kuhlman et al., 2007; Vilar and Leibler, 2003; Weinert et al., 2014) posit that gene expression is proportional to the probability that the RNAP is bound to the promoter p_{bound} , which is given by

$$p_{\text{bound}} = \frac{\frac{P}{N_{NS}} e^{-\beta\Delta\epsilon_P}}{1 + \frac{R_A}{N_{NS}} e^{-\beta\Delta\epsilon_{RA}} + \frac{R_I}{N_{NS}} e^{-\beta\Delta\epsilon_{RI}} + \frac{P}{N_{NS}} e^{-\beta\Delta\epsilon_P}}, \quad (2.1)$$

with $\beta = 1/k_B T$ where k_B is the Boltzmann constant and T is the temperature of the system. As $k_B T$ is the natural unit of energy at the molecular length scale, we treat the products $\beta\Delta\epsilon_j$ as single parameters within our model. Measuring p_{bound} directly is fraught with experimental difficulties, as determining the exact proportionality between expression and p_{bound} is not straightforward. Instead, we measure the fold-change in gene expression due to the presence of the repressor. We define fold-change as the ratio of gene expression in the presence of repressor relative to expression in the absence of repressor (i.e. constitutive expression), namely,

$$\text{fold-change} \equiv \frac{p_{\text{bound}}(R > 0)}{p_{\text{bound}}(R = 0)}. \quad (2.2)$$

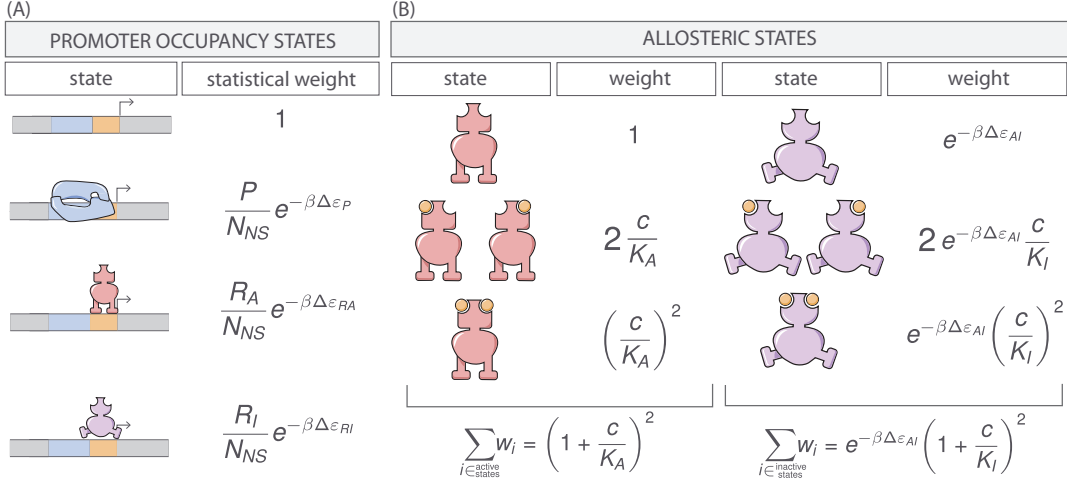


Figure 2.2: States and weights for the simple repression motif. (A) Occupancy states of the promoter. RNAP (light blue) and a repressor compete for binding to a promoter of interest. There are R_A repressors in the active state (red) and R_I repressors in the inactive state (purple). The difference in energy between a repressor bound to the promoter of interest versus another non-specific site elsewhere on the DNA equals $\Delta\varepsilon_{RA}$ in the active state and $\Delta\varepsilon_{RI}$ in the inactive state; the P RNAP have a corresponding energy difference $\Delta\varepsilon_P$ relative to non-specific binding on the DNA. N_{NS} represents the number of non-specific binding sites for both RNAP and repressor. (B) Allosteric states of the repressor. A repressor has an active conformation (red, left column) and an inactive conformation (purple, right column), with the energy difference between these two states given by $\Delta\varepsilon_{AI}$. The inducer (orange circle) at concentration c is capable of binding to the repressor with dissociation constants K_A in the active state and K_I in the inactive state. The eight states for a dimer with $n = 2$ inducer binding sites are shown along with the sums of the active and inactive states.

We can simplify this expression using two well-justified approximations: firstly, $(P/N_{NS})e^{-\beta \Delta \varepsilon_P} \ll 1$ implying that the RNAP binds weakly to the promoter ($N_{NS} = 4.6 \times 10^6$, $P \approx 10^3$ (Klumpp and Hwa, 2008), $\Delta\varepsilon_P \approx -2$ to $-5 k_B T$ (Brewster et al., 2012), so that $(P/N_{NS})e^{-\beta \Delta \varepsilon_P} \approx 0.01$) and (2) $(R_I/N_{NS})e^{-\beta \Delta \varepsilon_{RI}} \ll 1 + (R_A/N_{NS})e^{-\beta \Delta \varepsilon_{RA}}$ which reflects our assumption that the inactive repressor binds weakly to the promoter of interest. Using these approximations, the fold-change reduces to the form

$$\text{fold-change} \approx \left(1 + \frac{R_A}{N_{NS}} e^{-\beta \Delta \varepsilon_{RA}}\right)^{-1} \equiv \left(1 + p_{\text{act}}(c) \frac{R}{N_{NS}} e^{-\beta \Delta \varepsilon_{RA}}\right)^{-1}, \quad (2.3)$$

where in the last step we have introduced the fraction $p_{\text{act}}(c)$ of repressors in the

active state given a concentration c of inducer, such that $R_A(c) = p_{\text{act}}(c)R$. Since inducer binding shifts the repressors from the active to the inactive state, $p_{\text{act}}(c)$ grows smaller as c increases .

We use the MWC model to compute the probability $p_{\text{act}}(c)$ that a repressor with n inducer binding sites will be active. The value of $p_{\text{act}}(c)$ is given by the sum of the weights of the active repressor states divided by the sum of the weights of all possible repressor states see 2.2, namely,

$$p_{\text{act}}(c) = \frac{\left(1 + \frac{c}{K_A}\right)^n}{\left(1 + \frac{c}{K_A}\right)^n + e^{-\beta\Delta\varepsilon_{AI}} \left(1 + \frac{c}{K_I}\right)^n}, \quad (2.4)$$

where K_A and K_I represent the dissociation constant between the inducer and repressor in the active and inactive states, respectively, and $\Delta\varepsilon_{AI} = \varepsilon_I - \varepsilon_A$ is the free energy difference between a repressor in the inactive and active state [the quantity $e^{-\Delta\varepsilon_{AI}}$ is sometimes denoted by L (Marzen et al., 2013; Monod et al., 1965) or K_{RR^*} (Daber et al., 2011)]. In this equation, c/K_A and c/K_I represent the change in free energy when an inducer binds to a repressor in the active or inactive state, respectively, while $e^{-\beta\Delta\varepsilon_{AI}}$ represents the change in free energy when the repressor changes from the active to inactive state in the absence of inducer. Thus, a repressor which favors the active state in the absence of inducer ($\Delta\varepsilon_{AI} > 0$) will be driven towards the inactive state upon inducer binding when $K_I < K_A$. The specific case of a repressor dimer with $n = 2$ inducer binding sites is shown in Fig. 2.2 (B).

Substituting $p_{\text{act}}(c)$ from into yields the general formula for induction of a simple repression regulatory architecture (Phillips, 2015), namely,

$$\text{fold-change} = \left(1 + \frac{\left(1 + \frac{c}{K_A}\right)^n}{\left(1 + \frac{c}{K_A}\right)^n + e^{-\beta\Delta\varepsilon_{AI}} \left(1 + \frac{c}{K_I}\right)^n} \frac{R}{N_{NS}} e^{-\beta\Delta\varepsilon_{RA}} \right)^{-1}. \quad (2.5)$$

While we have used the specific case of simple repression with induction to craft this model, the same mathematics describe the case of corepression in which binding of an allosteric effector stabilizes the active state of the repressor and decreases gene expression (see Fig. 2.1). Interestingly, we shift from induction (governed by $K_I < K_A$) to corepression ($K_I > K_A$) as the ligand transitions from preferentially binding to the inactive repressor state to stabilizing the active state. Furthermore, this general approach can be used to describe a variety of other motifs such as

activation, multiple repressor binding sites, and combinations of activator and repressor binding sites (Bintu et al., 2005a; Brewster et al., 2014; Weinert et al., 2014).

The formula presented in Eq. 2.5 enables us to make precise quantitative statements about induction profiles. Motivated by the broad range of predictions implied by Eq. 2.5, we designed a series of experiments using the *lac* system in *E. coli* to tune the control parameters for a simple repression genetic circuit. As discussed in Fig. 2.1 (C), previous studies from our lab have provided well-characterized values for many of the parameters in our experimental system, leaving only the values of the MWC parameters (K_A , K_I , and $\Delta\varepsilon_{AI}$) to be determined. We note that while previous studies have obtained values for K_A , K_I , and $L = e^{-\beta\Delta\varepsilon_{AI}}$ (Daber et al., 2011; O’Gorman et al., 1980), they were either based upon biochemical experiments or *in vivo* conditions involving poorly characterized transcription factor copy numbers and gene copy numbers. These differences relative to our experimental conditions and fitting techniques led us to believe that it was important to perform our own analysis of these parameters. After inferring these three MWC parameters (see , Section “ ” for details regarding the inference of $\Delta\varepsilon_{AI}$, which was fitted separately from K_A and K_I), we were able to predict the input/output response of the system under a broad range of experimental conditions. For example, this framework can predict the response of the system at different repressor copy numbers R , repressor-operator affinities $\Delta\varepsilon_{RA}$, inducer concentrations c , and gene copy numbers (see Chapter 7.2).

2.3 Results

Experimental Design

We test our model by predicting the induction profiles for an array of strains that could be made using previously characterized repressor copy numbers and DNA binding energies. Our approach contrasts with previous studies that have parameterized induction curves of simple repression motifs, as these have relied on expression systems where proteins are expressed from plasmids, resulting in highly variable and unconstrained copy numbers (???: Daber et al., 2009, 2011; Murphy et al., 2007; Sochor, 2014). Instead, our approach relies on a foundation of previous work as depicted in Fig. ??types (C). This includes work from our laboratory that used *E. coli** constructs based on components of the *lac* system to demonstrate how the Lac repressor (LacI) copy number R and operator binding energy $\Delta\varepsilon * RA$ affect gene expression in the absence of inducer (Garcia and Phillips, 2011). Rydenfelt et al. (2014a) extended the theory used in that work to the case of multiple promoters

competing for a given transcription factor, which was validated experimentally by Brewster et al. (2014), who modified this system to consider expression from multiple-copy plasmids as well as the presence of competing repressor binding sites.

The present study extends this body of work by introducing three additional biophysical parameters – $\Delta\epsilon_{AI}$, K_A , and K_I – which capture the allosteric nature of the transcription factor and complement the results shown by Garcia and Phillips (2011) and Brewster et al. (2014). Although the current work focuses on systems with a single site of repression, in the Materials and Methods, we utilize data from Brewster et al. (2014), in which multiple sites of repression are explored, to characterize the allosteric free energy difference $\Delta\epsilon_{AI}$ between the repressor’s active and inactive states. This additional data set is critical because multiple degenerate sets of parameters can characterize an induction curve equally well, with the $\Delta\epsilon_{AI}$ parameter compensated by the inducer dissociation constants K_A and K_I (see Chapter 7, Supplementary Information). After fixing $\Delta\epsilon_{AI}$ as described in the Materials and Methods, we can use data from single-site simple repression systems to determine the values of K_A and K_I .

We determine the values of K_A and K_I by fitting to a single induction profile using Bayesian inferential methods (Sivia and Skilling, 2006). We then use Eq. ?? to predict gene expression for any concentration of inducer, repressor copy number, and DNA binding energy and compare these predictions against experimental measurements. To obtain induction profiles for a set of strains with varying repressor copy numbers, we used modified *lacI* ribosomal binding sites from Garcia and Phillips (2011) to generate strains with mean repressor copy number per cell of $R = 22 \pm 4$, 60 ± 20 , 124 ± 30 , 260 ± 40 , 1220 ± 160 , and 1740 ± 340 , where the error denotes standard deviation of at least three replicates as measured by Garcia and Phillips (2011). We note that R refers to the number of repressor dimers in the cell, which is twice the number of repressor tetramers reported by Garcia and Phillips (2011); since both heads of the repressor are assumed to always be either specifically or non-specifically bound to the genome, the two repressor dimers in each LacI tetramer can be considered independently. Gene expression was measured using a Yellow Fluorescent Protein (YFP) gene, driven by a *lacUV5* promoter. Each of the six repressor copy number variants were paired with the native O1, O2, or O3 *lac* operator (Oehler et al., 1994) placed at the YFP transcription start site, thereby generating eighteen unique strains. The repressor-operator binding

energies ($O1 \Delta\varepsilon * RA = -15.3 \pm 0.2 k * BT$, $O2 \Delta\varepsilon * RA = -13.9 k * BT \pm 0.2$, and $O3 \Delta\varepsilon * RA = -9.7 \pm 0.1 k * BT$) were previously inferred by measuring the fold-change of the *lac* system at different repressor copy numbers, where the error arises from model fitting (Garcia and Phillips, 2011). Additionally, we were able to obtain the value $\Delta\varepsilon * AI = 4.5 k * BT$ by fitting to previous data as discussed in the Materials and Methods. We measure fold-change over a range of known IPTG concentrations c , using $n = 2$ inducer binding sites per LacI dimer and approximating the number of non-specific binding sites as the length in base-pairs of the *E. coli* genome, $N_{NS} = 4.6 \times 10^6$.

Our experimental pipeline for determining fold-change using flow cytometry is shown in Fig. 2.3. Briefly, cells were grown to exponential phase, in which gene expression reaches steady state (???), under concentrations of the inducer IPTG ranging between 0 and 5000 μM . We measure YFP fluorescence using flow cytometry and automatically gate the data to include only single-cell measurements (see Materials and Methods). To validate the use of flow cytometry, we also measured the fold-change of a subset of strains using the established method of single-cell microscopy (see Supplemental Information, Chapter 7). We found that the fold-change measurements obtained from microscopy were indistinguishable from that of flow-cytometry and yielded values for the inducer binding constants K_A and K_I that were within error.

Determination of the *in vivo* MWC Parameters

The three parameters that we tune experimentally are shown in , leaving the three allosteric parameters ($\Delta\varepsilon_{AI}$, K_A , and K_I) to be determined by fitting. We used previous LacI fold-change data (Brewster et al., 2014) to infer that $\Delta\varepsilon_{AI} = 4.5 k_B T$ (see Materials & Methods). Rather than fitting K_A and K_I to our entire data set of eighteen unique constructs, we performed Bayesian parameter estimation on data from a single strain with $R = 260$ and an O2 operator [$\Delta\varepsilon_{RA} = -13.9 k_B T$ (Garcia and Phillips, 2011)] shown in Fig. 2.4(D, orange points). Using Markov Chain Monte Carlo, we determine the most likely parameter values to be $K_A = 139^{+29}_{-22} \times 10^{-6} \text{ M}$ and $K_I = 0.53^{+0.04}_{-0.04} \times 10^{-6} \text{ M}$, which are the modes of their respective distributions, where the superscripts and subscripts represent the upper and lower bounds of the 95th percentile of the parameter value distributions [see Fig. 2.4 (B)]. Unfortunately, we are not able to make a meaningful value-for-value comparison of our parameters to those of earlier studies (Daber et al., 2009, 2011) because of uncertainties in both gene copy number and transcription factor copy numbers in these studies, as

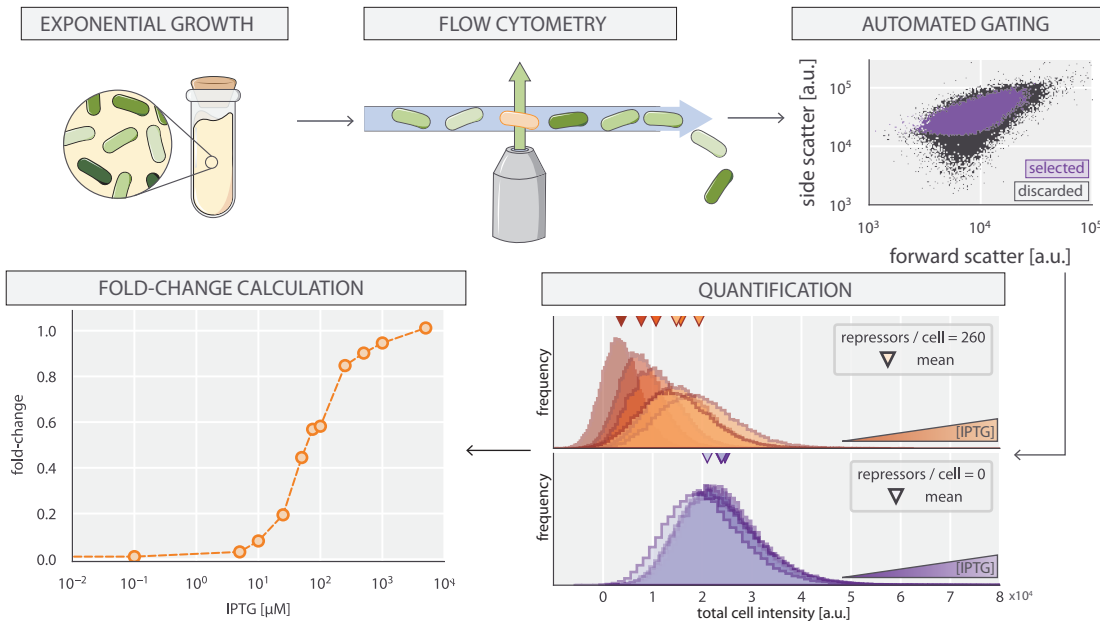


Figure 2.3: An experimental pipeline for high-throughput fold-change measurements. Cells are grown to exponential steady state and their fluorescence is measured using flow cytometry. Automatic gating methods using forward- and side-scattering are used to ensure that all measurements come from single cells (see Methods). Mean expression is then quantified at different IPTG concentrations (top, blue histograms) and for a strain without repressor (bottom, green histograms), which shows no response to IPTG as expected. Fold-change is computed by dividing the mean fluorescence in the presence of repressor by the mean fluorescence in the absence of repressor.

illustrated in Supplemental Chapter 7. We then predicted the fold-change for the remaining seventeen strains with no further fitting [see Fig. 2.4 (C - E)] together with the specific phenotypic properties described in and discussed in detail below [see Fig. ?? (F - J)]. The shaded regions in Fig. 2.4 (C - E) denote the 95% credible regions. Factors determining the width of the credible regions are explored in Supplemental Chapter 7.

We stress that the entire suite of predictions is based upon the induction profile of a single strain. Our ability to make such a broad range of predictions stems from the fact that our parameters of interest such as the repressor copy number and DNA binding energy - appear as distinct physical parameters within our model. While the single data set in Fig. 2.4 could also be fit using a Hill function, such an analysis would be unable to predict any of the other curves in the figure (see Materials & Methods). Phenomenological expressions such as the Hill function

can describe data, but lack predictive power and are thus unable to build our intuition, help us design *de novo* input-output functions, or guide future experiments (Kuhlman et al., 2007; Murphy et al., 2007).

Comparison of Experimental Measurements with Theoretical Predictions

We tested the predictions shown in Fig. 2.4 by measuring fold-change induction profiles in strains with a broad range of repressor copy numbers and repressor binding energies as characterized in Garcia and Phillips (2011). With a few notable exceptions, the results shown in Fig. 2.5 demonstrate agreement between theory and experiment. We note that there was an apparently systematic shift in the O3 $\Delta\epsilon_{RA} = -9.7 k_B T$ strains Fig. 2.5 and all of the $R = 1220$ and $R = 1740$ strains. This may be partially due to imprecise previous determinations of their $\Delta\epsilon_{RA}$ and R values. By performing a global fit where we infer all parameters including the repressor copy number R and the binding energy $\Delta\epsilon_{RA}$, we found better agreement for these strains, although a discrepancy in the steepness of the response for all O3 strains remains (see Materials & Methods). We considered a number of hypotheses to explain these discrepancies such as including other states (e.g. non-negligible binding of the inactive repressor), relaxing the weak promoter approximation, and accounting for variations in gene and repressor copy number throughout the cell cycle, but none explained the observed discrepancies. As an additional test of our model, we considered strains using the synthetic Oid operator which exhibits an especially strong binding energy of $\Delta\epsilon_{RA} = -17 k_B T$ (Garcia and Phillips, 2011). The global fit agrees well with the Oid microscopy data, though it asserts a stronger Oid binding energy of $\Delta\epsilon_{RA} = -17.7 k_B T$ (see Supplemental Chapter 7).

To ensure that the agreement between our predictions and data is not an accident of the strain we used to perform our fitting, we also inferred K_A and K_I from each of the other strains. As discussed in the Materials & Methods and Fig. 2.4, the inferred values of K_A and K_I depend minimally upon which strain is chosen, indicating that these parameter values are highly robust. We also performed a global fit using the data from all eighteen strains in which we fitted for the inducer dissociation constants K_A and K_I , the repressor copy number R , and the repressor DNA binding energy $\Delta\epsilon_{RA}$ (see Materials & Methods). The resulting parameter values were nearly identical to those fitted from any single strain. For the remainder of the text we continue using parameters fitted from the strain with $R = 260$ repressors and an O2 operator.

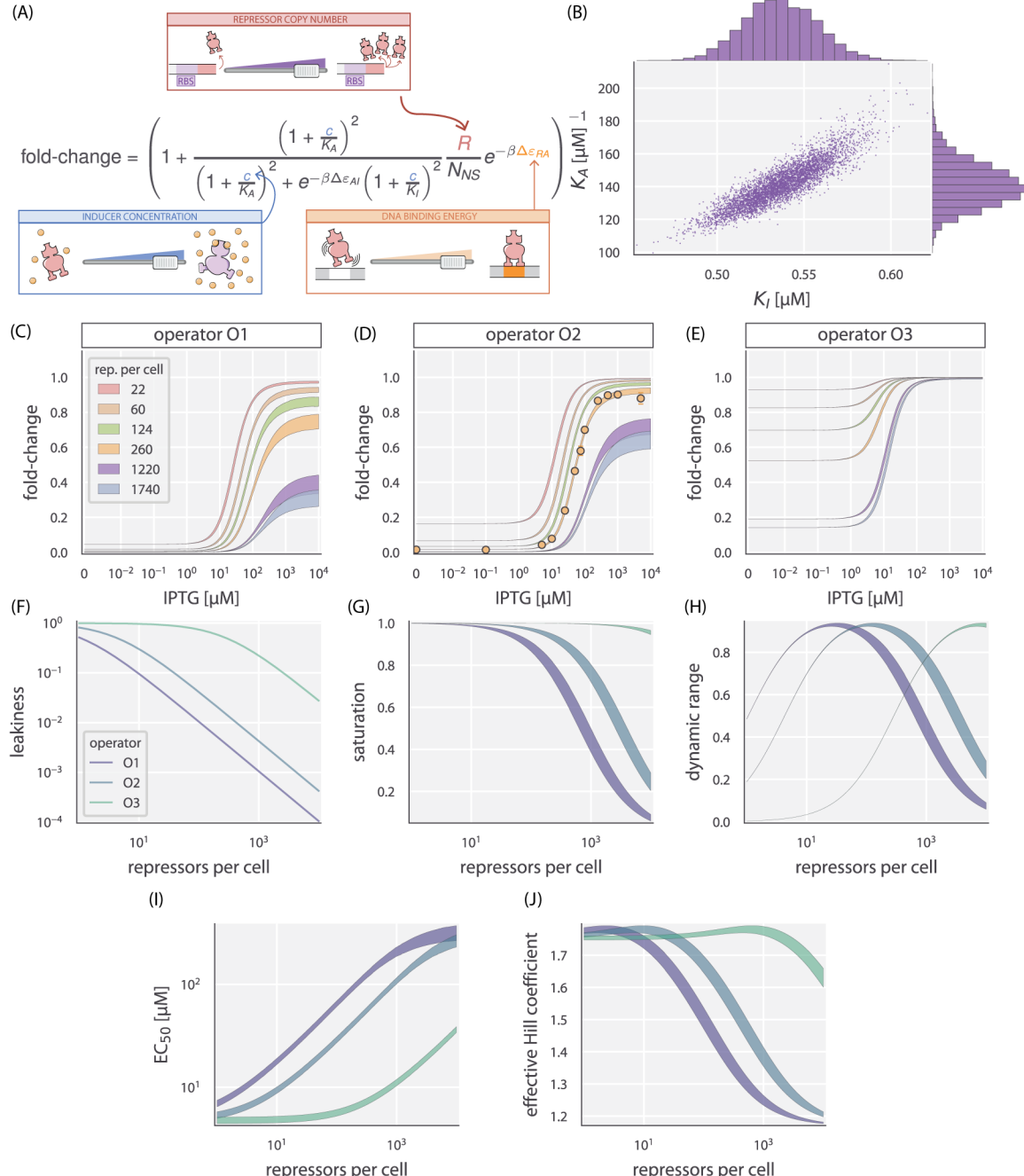


Figure 2.4: Predicting induction profiles for different biological control parameters. (A) Schematic representation of experimentally accessible variables. Repressor copy number R is tuned by changing the sequence of the ribosomal binding site (RBS), DNA binding energy $\Delta\epsilon_{RA}$ is controlled via the sequence of the operator, and the inducer concentration c is controlled via a dilution series. (B) Markov Chain Monte Carlo (MCMC) sampling of the posterior distribution of K_A and K_I . Each point corresponds to a single MCMC sample. Distribution on top and left represent the marginal posterior probability distribution over K_A and K_I , respectively. (C) Predicted induction profiles for strains with various repressor copy numbers and DNA binding energies. White-faced points represent those to which the inducer binding constants K_A and K_I were determined. (D) Predicted properties of the induction profiles in (C) using parameter values known *a priori*. The shaded regions denote the 95% credible region. Region between 0 and $10^{-7} \mu\text{M}$ is scaled linearly with log scaling elsewhere.

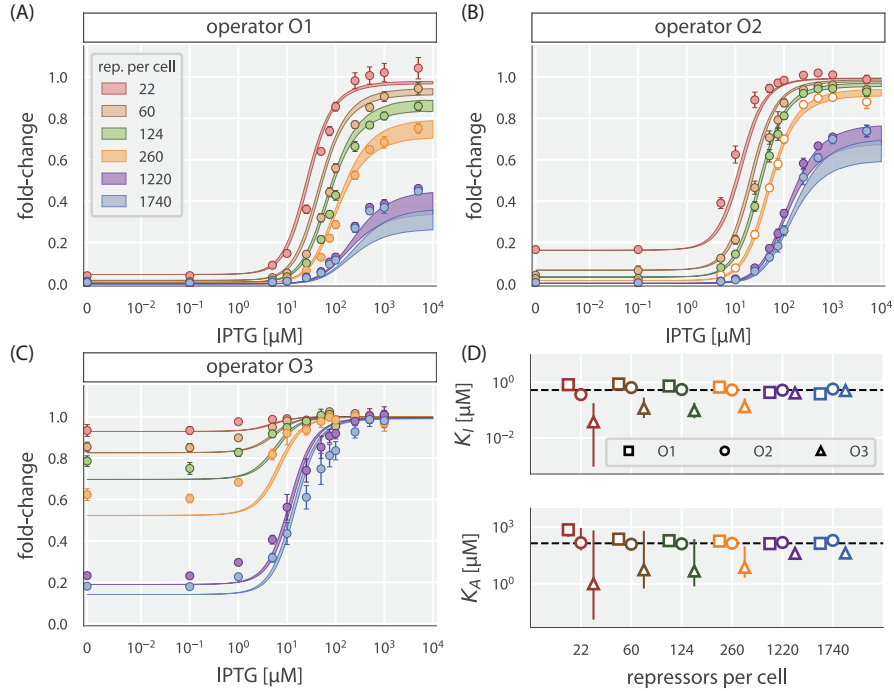


Figure 2.5: Comparison of predictions against measured and inferred data. Flow cytometry measurements of fold-change over a range of IPTG concentrations for O1, O2, and O3 strains at varying repressor copy numbers, overlaid on the predicted responses. Error bars for the experimental data show the standard error of the mean (eight or more replicates). As discussed in Fig. 2.4, all of the predicted induction curves were generated prior to measurement by inferring the MWC parameters using a single data set (O2 $R = 260$, shown by white circles in Panel B). The predictions may therefore depend upon which strain is used to infer the parameters. The inferred parameter values of the dissociation constants K_A and K_I using any of the eighteen strains instead of the O2 $R = 260$ strain. Nearly identical parameter values are inferred from each strain, demonstrating that the same set of induction profiles would have been predicted regardless of which strain was chosen. The points show the mode, and the error bars denote the 95 credible region of the parameter value distribution. Error bars not visible are smaller than the size of the marker.

Predicting the Phenotypic Traits of the Induction Response

A subset of the properties shown in Fig. 2.1 (i.e. the leakiness, saturation, dynamic range, $[EC_{50}]$, and effective Hill coefficient) are of significant interest to synthetic biology. For example, synthetic biology is often focused on generating large responses (i.e. a large dynamic range) or finding a strong binding partner (i.e. a small $[EC_{50}]$) (Brophy and Voigt, 2014; Shis et al., 2014). While these properties are all individually informative, when taken together they capture the essential features of the induction response. We reiterate that a Hill function approach cannot predict these features *a priori* and furthermore requires fitting each curve individually. The MWC model, on the other hand, enables us to quantify how each trait depends upon a single set of physical parameters as shown by Fig. 2.4 (F-J).

We define these five phenotypic traits using expressions derived from the model presented in Eq. ???. These results build upon extensive work by Martins and Swain (2011), who computed many such properties for ligand-receptor binding within the MWC model. We begin by analyzing the leakiness, which is the minimum fold-change observed in the absence of ligand, given by

$$\text{leakiness} = \text{fold-change}(c = 0) = \left(1 + \frac{1}{1 + e^{-\beta\Delta\varepsilon_{AI}}} \frac{R}{N_{NS}} e^{-\beta\Delta\varepsilon_{RA}} \right)^{-1},$$

and the saturation, which is the maximum fold change observed in the presence of saturating ligand,

$$\begin{aligned} \text{saturation} &= \text{fold-change}(c \rightarrow \infty) \\ &= \left(1 + \frac{1}{1 + e^{-\beta\Delta\varepsilon_{AI}}} \left(\frac{K_A}{K_I} \right)^n \frac{R}{N_{NS}} e^{-\beta\Delta\varepsilon_{RA}} \right)^{-1}. \end{aligned}$$

Systems that minimize leakiness repress strongly in the absence of effector while systems that maximize saturation have high expression in the presence of effector. Together, these two properties determine the dynamic range of a system's response, which is given by the difference

$$\text{dynamic range} = \text{saturation} - \text{leakiness} \tag{2.6}$$

These three properties are shown in Fig. 2.4 (F-H). We discuss these properties in greater detail in the Materials & Methods section. Fig. ?? shows that the measure-

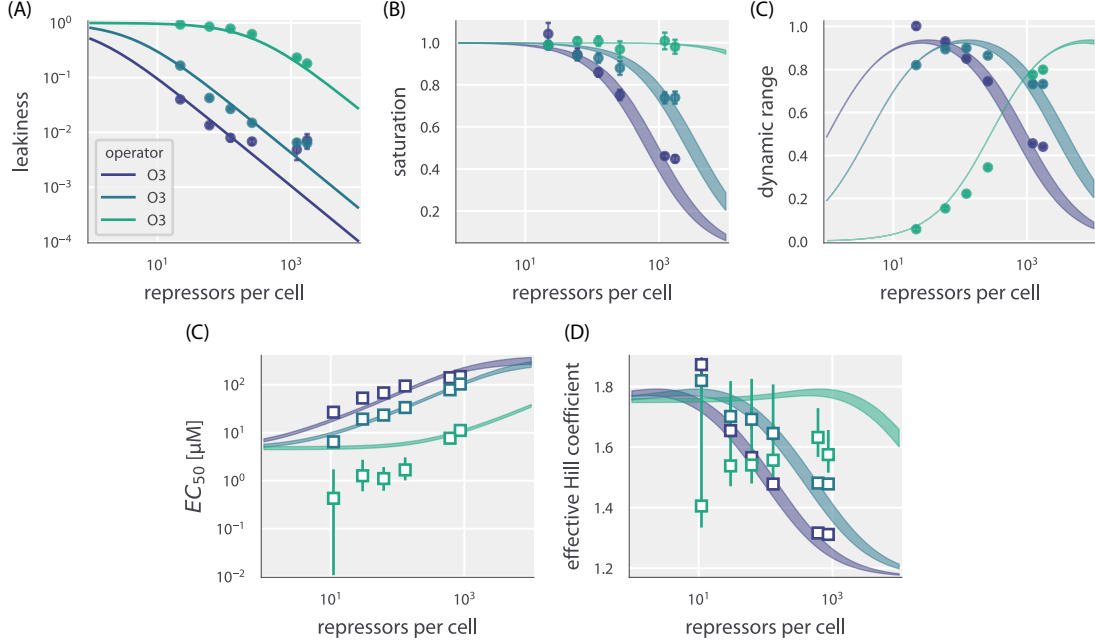


Figure 2.6: Predictions and experimental measurements of key properties of induction profiles. Data for the leakiness, saturation, and dynamic range are obtained from fold-change measurements in the absence of IPTG and at saturating concentrations of IPTG. The three repressor-operator binding energies in the legend correspond to the O1 operator ($-15.3 k_B T$), O2 operator ($-13.9 k_B T$), and O3 operator ($-9.7 k_B T$). Both the $[EC_{50}]$ and effective Hill coefficient are inferred by individually fitting each operator-repressor pairing - separately to in order to smoothly interpolate between the data points. Error bars for - represent the standard error of the mean for eight or more replicates; error bars for - represent the 95% credible region for the parameter found by propagating the credible region of our estimates of K_A and K_I into Eq. ??.

ments of these three properties, derived from the fold-change data in the absence of IPTG and the presence of saturating IPTG, closely match the predictions for all three operators.

Two additional properties of induction profiles are the $[EC_{50}]$ and effective Hill coefficient, which determine the range of inducer concentration in which the system's output goes from its minimum to maximum value. The $[EC_{50}]$ denotes the inducer concentration required to generate a system response halfway between its minimum and maximum value,

$$\text{fold-change}(c = [EC_{50}]) = \frac{\text{leakiness} + \text{saturation}}{2}. \quad (2.7)$$

The effective Hill coefficient h , which quantifies the steepness of the curve at the

$[EC_{50}]$, is given by

$$h = \left(2 \frac{d}{d \log c} \left[\log \left(\frac{\text{fold-change}(c) - \text{leakiness}}{\text{dynamic range}} \right) \right] \right)_{c=[EC_{50}]} . \quad (2.8)$$

shows how the $[EC_{50}]$ and effective Hill coefficient depend on the repressor copy number. In , Section “”, we discuss the analytic forms of these two properties as well as their dependence on the repressor-DNA binding energy.

- shows the estimated values of the $[EC_{50}]$ and the effective Hill coefficient overlaid on the theoretical predictions. Both properties were obtained by fitting to each individual titration curve and computing the $[EC_{50}]$ and effective Hill coefficient using and , respectively. We find that the predictions made with the single strain fit closely match those made for each of the strains with O1 and O2 operators, but the predictions for the O3 operator are markedly off. In the , Section “”, we show that the large, asymmetric error bars for the O3 $R = 22$ strain arise from its nearly flat response, where the lack of dynamic range makes it impossible to determine the value of the inducer dissociation constants K_A and K_I , as can be seen in the uncertainty of both the $[EC_{50}]$ and effective Hill coefficient. Discrepancies between theory and data for O3 are improved, but not fully resolved, by performing a global fit or fitting the MWC model individually to each curve (see , Sections “” and “”). It remains an open question how to account for discrepancies in O3, in particular regarding the significant mismatch between the predicted and fitted effective Hill coefficients.

2.4 Discussion

Since the early work by Monod, Wyman, and Changeux , an array of biological phenomena has been tied to the existence of macromolecules that switch between inactive and active states. Examples can be found in a wide variety of cellular processes, including ligand-gated ion channels , enzymatic reactions , chemotaxis , quorum sensing , G-protein coupled receptors , physiologically important proteins , and beyond. One of the most ubiquitous examples of allostery is in the context of gene expression, where an array of molecular players bind to transcription factors to influence their ability to regulate gene activity . A number of studies have focused on developing a quantitative understanding of allosteric regulatory systems. analytically derived fundamental properties of the MWC model, including the leakiness and dynamic range described in this work, noting the inherent trade-offs in these properties when tuning the model’s parameters. Work in the Church

and Voigt labs, among others, has expanded on the availability of allosteric circuits for synthetic biology . Recently, Daber *et al.* theoretically explored the induction of simple repression within the MWC model and experimentally measured how mutations alter the induction profiles of transcription factors . Vilar and Saiz analyzed a variety of interactions in inducible *lac*-based systems including the effects of oligomerization and DNA folding on transcription factor induction . Other work has attempted to use the *lac* system to reconcile *in vitro* and *in vivo* measurements .

Although this body of work has done much to improve our understanding of allosteric transcription factors, there have been few attempts to explicitly connect quantitative models to experiments. Here, we generate a predictive model of allosteric transcriptional regulation and then test the model against a thorough set of experiments using well-characterized regulatory components. Specifically, we used the MWC model to build upon a well-established thermodynamic model of transcriptional regulation , allowing us to compose the model from a minimal set of biologically meaningful parameters. This model combines both theoretical and experimental insights; for example, rather than considering gene expression directly we analyze the fold-change in expression, where the weak promoter approximation (see) circumvents uncertainty in the RNAP copy number. The resulting model depended upon experimentally accessible parameters, namely, the repressor copy number, the repressor-DNA binding energy, and the concentration of inducer. We tested these predictions on a range of strains whose repressor copy number spanned two orders of magnitude and whose DNA binding affinity spanned $6 k_B T$. We argue that one would not be able to generate such a wide array of predictions by using a Hill function, which abstracts away the biophysical meaning of the parameters into phenomenological parameters .

More precisely, we tested our model in the context of a *lac*-based simple repression system by first determining the allosteric dissociation constants K_A and K_I from a single induction data set (O2 operator with binding energy $\Delta\epsilon_{RA} = -13.9 k_B T$ and repressor copy number $R = 260$) and then using these values to make parameter-free predictions of the induction profiles for seventeen other strains where $\Delta\epsilon_{RA}$ and R were varied significantly (see). We next measured the induction profiles of these seventeen strains using flow cytometry and found that our predictions consistently and accurately captured the primary features for each induction data set, as shown in -. Importantly, we find that fitting K_A and K_I to data from any other

strain would have resulted in nearly identical predictions (see and , Section “ ”). This suggests that a few carefully chosen measurements can lead to a deep quantitative understanding of how simple regulatory systems work without requiring an extensive sampling of strains that span the parameter space. Moreover, the fact that we could consistently achieve reliable predictions after fitting only two free parameters stands in contrast to the common practice of fitting several free parameters simultaneously, which can nearly guarantee an acceptable fit provided that the model roughly resembles the system response, regardless of whether the details of the model are tied to any underlying molecular mechanism.

Beyond observing changes in fold-change as a function of effector concentration, our application of the MWC model allows us to explicitly predict the values of the induction curves’ key parameters, namely, the leakiness, saturation, dynamic range, $[EC_{50}]$, and the effective Hill coefficient (see). We are consistently able to accurately predict the leakiness, saturation, and dynamic range for each of the strains. For both the O1 and O2 data sets, our model also accurately predicts the effective Hill coefficient and $[EC_{50}]$, though these predictions for O3 are noticeably less accurate. While performing a global fit for all model parameters marginally improves the prediction for O3 (see , Section “ ”), we are still unable to accurately predict the effective Hill coefficient or the $[EC_{50}]$. We further tried including additional states (such as allowing the inactive repressor to bind to the operator), relaxing the weak promoter approximation, accounting for changes in gene and repressor copy number throughout the cell cycle , and refitting the original binding energies from , but we were still unable to account for the O3 data. It remains an open question as to how the discrepancy between the theory and measurements for O3 can be reconciled.

The dynamic range, which is of considerable interest when designing or characterizing a genetic circuit, is revealed to have an interesting property: although changing the value of $\Delta\varepsilon_{RA}$ causes the dynamic range curves to shift to the right or left, each curve has the same shape and in particular the same maximum value. This means that strains with strong or weak binding energies can attain the same dynamic range when the value of R is tuned to compensate for the binding energy. This feature is not immediately apparent from the IPTG induction curves, which show very low dynamic ranges for several of the O1 and O3 strains. Without the benefit of models that can predict such phenotypic traits, efforts to engineer genetic circuits with allosteric transcription factors must rely on trial and error to achieve

specific responses .

Despite the diversity observed in the induction profiles of each of our strains, our data are unified by their reliance on fundamental biophysical parameters. In particular, we have shown that our model for fold-change can be rewritten in terms of the free energy , which encompasses all of the physical parameters of the system. This has proven to be an illuminating technique in a number of studies of allosteric proteins . Although it is experimentally straightforward to observe system responses to changes in effector concentration c , framing the input-output function in terms of c can give the misleading impression that changes in system parameters lead to fundamentally altered system responses. Alternatively, if one can find the “natural variable” that enables the output to collapse onto a single curve, it becomes clear that the system’s output is not governed by individual system parameters, but rather the contributions of multiple parameters that define the natural variable. When our fold-change data are plotted against the respective free energies for each construct, they collapse cleanly onto a single curve (see). This enables us to analyze how parameters can compensate each other. For example, rather than viewing strong repression as a consequence of low IPTG concentration c or high repressor copy number R , we can now observe that strong repression is achieved when the free energy $F(c) \leq -5k_B T$, a condition which can be reached in a number of ways.

While our experiments validated the theoretical predictions in the case of simple repression, we expect the framework presented here to apply much more generally to different biological instances of allosteric regulation. For example, we can use this model to study more complex systems such as when transcription factors interact with multiple operators . We can further explore different regulatory configurations such as corepression, activation, and coactivation, each of which are found in *E. coli* (see Appendix supplemental Chapter 6). This work can also serve as a springboard to characterize not just the mean but the full gene expression distribution and thus quantify the impact of noise on the system . Another extension of this approach would be to theoretically predict and experimentally verify whether the repressor-inducer dissociation constants K_A and K_I or the energy difference $\Delta\epsilon_{AI}$ between the allosteric states can be tuned by making single amino acid substitutions in the transcription factor . Finally, we expect that the kind of rigorous quantitative description of the allosteric phenomenon provided here will make it possible to construct biophysical models of fitness for allosteric proteins

similar to those already invoked to explore the fitness effects of transcription factor binding site strengths and protein stability .

To conclude, we find that our application of the MWC model provides an accurate, predictive framework for understanding simple repression by allosteric transcription factors. To reach this conclusion, we analyzed the model in the context of a well-characterized system, in which each parameter had a clear biophysical meaning. As many of these parameters had been measured or inferred in previous studies, this gave us a minimal model with only two free parameters which we inferred from a single data set. We then accurately predicted the behavior of seventeen other data sets in which repressor copy number and repressor-DNA binding energy were systematically varied. In addition, our model allowed us to understand how key properties such as the leakiness, saturation, dynamic range, $[EC_{50}]$, and effective Hill coefficient depended upon the small set of parameters governing this system. Finally, we show that by framing inducible simple repression in terms of free energy, the data from all of our experimental strains collapse cleanly onto a single curve, illustrating the many ways in which a particular output can be targeted. In total, these results show that a thermodynamic formulation of the MWC model supersedes phenomenological fitting functions for understanding transcriptional regulation by allosteric proteins.

2.5 Methods

Bacterial Strains and DNA Constructs

All strains used in these experiments were derived from *E. coli* K12 MG1655 with the *lac* operon removed, adapted from those created and described in Garcia and Phillips (2011). Briefly, the operator variants and YFP reporter gene were cloned into a pZS25 background which contains a *lacUV5* promoter that drives expression as is shown schematically in Fig. 2.2. These constructs carried a kanamycin resistance gene and were integrated into the *galK* locus of the chromosome using λ Red recombineering Sharan et al. (2009). The *lacI* gene was constitutively expressed via a $P_{LtetO-1}$ promoter (Lutz and Bujard, 1997), with ribosomal binding site mutations made to vary the LacI copy number as described in Salis et al. (2009) using site-directed mutagenesis (Quickchange II; Stratagene), with further details in Garcia and Phillips (2011). These *lacI* constructs carried a chloramphenicol resistance gene and were integrated into the *ybcN* locus of the chromosome. Final strain construction was achieved by performing repeated P1 transduction (Thomason et al., 2007) of the different operator and *lacI* constructs to generate each combination used in

this work. Integration was confirmed by PCR amplification of the replaced chromosomal region and by sequencing. Primers and final strain genotypes are listed in supplemental Chapter 7.

It is important to note that the rest of the *lac* operon (*lacZYA*) was never expressed. The LacY protein is a transmembrane protein which actively transports lactose as well as IPTG into the cell. As LacY was never produced in our strains, we assume that the extracellular and intracellular IPTG concentration was approximately equal due to diffusion across the membrane into the cell as is suggested by previous work (Fernández-Castané et al., 2012).

To make this theory applicable to transcription factors with any number of DNA binding domains, we used a different definition for repressor copy number than has been used previously. We define the LacI copy number as the average number of repressor dimers per cell whereas in Garcia and Phillips (2011), the copy number is defined as the average number of repressor tetramers in each cell. To motivate this decision, we consider the fact that the LacI repressor molecule exists as a tetramer in *E. coli* (Lewis et al., 1996) in which a single DNA binding domain is formed from dimerization of LacI proteins, so that wild-type LacI might be described as dimer of dimers. Since each dimer is allosterically independent (i.e. either dimer can be allosterically active or inactive, independent of the configuration of the other dimer) (Daber et al., 2009), a single LacI tetramer can be treated as two functional repressors. Therefore, we have simply multiplied the number of repressors reported in Garcia and Phillips (2011) by a factor of two. This factor is included as a keyword argument in the numerous Python functions used to perform this analysis, as discussed in the code documentation.

A subset of strains in these experiments were measured using fluorescence microscopy for validation of the flow cytometry data and results. To aid in the high-fidelity segmentation of individual cells, the strains were modified to constitutively express an mCherry fluorophore. This reporter was cloned into a pZS4*1 backbone (Lutz and Bujard, 1997) in which mCherry is driven by the *lacUV5* promoter. All microscopy and flow cytometry experiments were performed using these strains.

Growth Conditions for Flow Cytometry Measurements

All measurements were performed with *E. coli* cells grown to mid-exponential phase in standard M9 minimal media (M9 5X Salts, Sigma-Aldrich M6030; 2 mM

magnesium sulfate, Mallinckrodt Chemicals 6066-04; 100 μ M calcium chloride, Fisher Chemicals C79-500) supplemented with 0.5% (w/v) glucose. Briefly, 500 μ L cultures of *E. coli* were inoculated into Lysogeny Broth (LB Miller Powder, BD Medical) from a 50% glycerol frozen stock (-80°C) and were grown overnight in a 2 mL 96-deep-well plate sealed with a breathable nylon cover (Lab Pak - Nitex Nylon, Sefar America Inc. Cat. No. 241205) with rapid agitation for proper aeration. After approximately 12 to 15 hours, the cultures had reached saturation and were diluted 1000-fold into a second 2 mL 96-deep-well plate where each well contained 500 μ L of M9 minimal media supplemented with 0.5% w/v glucose (anhydrous D-Glucose, Macron Chemicals) and the appropriate concentration of IPTG (Isopropyl β -D-1 thiogalactopyranoside Dioxane Free, Research Products International). These were sealed with a breathable cover and were allowed to grow for approximately eight hours. Cells were then diluted ten-fold into a round-bottom 96-well plate (Corning Cat. No. 3365) containing 90 μ L of M9 minimal media supplemented with 0.5% w/v glucose along with the corresponding IPTG concentrations. For each IPTG concentration, a stock of 100-fold concentrated IPTG in double distilled water was prepared and partitioned into 100 μ L aliquots. The same parent stock was used for all experiments described in this work.

Flow Cytometry

Unless explicitly mentioned, all fold-change measurements were collected on a Miltenyi Biotec MACSquant Analyzer 10 Flow Cytometer graciously provided by the Pamela Björkman lab at Caltech. Detailed information regarding the voltage settings of the photo-multiplier detectors can be found in the supplemental Chapter 7.

Prior to each day's experiments, the analyzer was calibrated using MACSQuant Calibration Beads (Cat. No. 130-093-607) such that day-to-day experiments would be comparable. All YFP fluorescence measurements were collected via 488 nm laser excitation coupled with a 525/50 nm emission filter. Unless otherwise specified, all measurements were taken over the course of two to three hours using automated sampling from a 96-well plate kept at approximately 4° - 10°C on a MACS Chill 96 Rack (Cat. No. 130-094-459). Cells were diluted to a final concentration of approximately 4×10^4 cells per μ L which corresponded to a flow rate of 2,000-6,000 measurements per second, and acquisition for each well was halted after 100,000 events were detected. Once completed, the data were extracted and immediately processed using the following methods.

Unsupervised Gating of Flow Cytometry Data

Flow cytometry data will frequently include a number of spurious events or other undesirable data points such as cell doublets and debris. The process of restricting the collected data set to those data determined to be “real” is commonly referred to as gating. These gates are typically drawn manually and restrict the data set to those points which display a high degree of linear correlation between their forward-scatter (FSC) and side-scatter (SSC). The development of unbiased and unsupervised methods of drawing these gates is an active area of research . For our purposes, we assume that the fluorescence level of the population should be log-normally distributed about some mean value. With this assumption in place, we developed a method that allows us to restrict the data used to compute the mean fluorescence intensity of the population to the smallest two-dimensional region of the $\log(\text{FSC})$ vs. $\log(\text{SSC})$ space in which 40% of the data is found. This was performed by fitting a bivariate Gaussian distribution and restricting the data used for calculation to those that reside within the 40th percentile. This procedure is described in more detail in the supplemental Chapter 7.

Experimental Determination of Fold-Change

For each strain and IPTG concentration, the fold-change in gene expression was calculated by taking the ratio of the population mean YFP expression in the presence of LacI repressor to that of the population mean in the absence of LacI repressor. However, the measured fluorescence intensity of each cell also includes the autofluorescence contributed by the weak excitation of the myriad protein and small molecules within the cell. To correct for this background, we computed the fold change as

$$\text{fold-change} = \frac{\langle I_{R>0} \rangle - \langle I_{\text{auto}} \rangle}{\langle I_{R=0} \rangle - \langle I_{\text{auto}} \rangle}, \{ \# \text{eq:induction_image_def} \}$$

where $\langle I_{R>0} \rangle$ is the average cell YFP intensity in the presence of repressor, $\langle I_{R=0} \rangle$ is the average cell YFP intensity in the absence of repressor, and $\langle I_{\text{auto}} \rangle$ is the average cell autofluorescence intensity, as measured from cells that lack the *lac*-YFP construct.

Bayesian Parameter Estimation

In this work, we determine the the most likely parameter values for the inducer dissociation constants K_A and K_I of the active and inactive state, respectively, using Bayesian methods. We compute the probability distribution of the value of each

parameter given the data D , which by Bayes' theorem is given by

$$P(K_A, K_I | D) = \frac{P(D | K_A, K_I)P(K_A, K_I)}{P(D)}, \quad (2.9)$$

where D is all the data composed of independent variables (repressor copy number R , repressor-DNA binding energy $\Delta\epsilon_{RA}$, and inducer concentration c) and one dependent variable (experimental fold-change). $P(D | K_A, K_I)$ is the likelihood of having observed the data given the parameter values for the dissociation constants, $P(K_A, K_I)$ contains all the prior information on these parameters, and $P(D)$ serves as a normalization constant, which we can ignore in our parameter estimation. Eq. ?? assumes a deterministic relationship between the parameters and the data, so in order to construct a probabilistic relationship as required by Eq. 2.9, we assume that the experimental fold-change for the i^{th} datum given the parameters is of the form

$$\text{fold-change}_{\text{exp}}^{(i)} = \left(1 + \frac{\left(1 + \frac{c^{(i)}}{K_A}\right)^2}{\left(1 + \frac{c^{(i)}}{K_A}\right)^2 + e^{-\beta\Delta\epsilon_{AI}} \left(1 + \frac{c^{(i)}}{K_I}\right)^2} \frac{R^{(i)}}{N_{NS}} e^{-\beta\Delta\epsilon_{RA}^{(i)}} \right)^{-1} + \epsilon^{(i)}, \quad (2.10)$$

where $\epsilon^{(i)}$ represents the departure from the deterministic theoretical prediction for the i^{th} data point. If we assume that these $\epsilon^{(i)}$ errors are normally distributed with mean zero and standard deviation σ , the likelihood of the data given the parameters is of the form

$$P(D | K_A, K_I, \sigma) = \frac{1}{(2\pi\sigma^2)^{\frac{n}{2}}} \prod_{i=1}^n \exp \left[-\frac{(\text{fold-change}_{\text{exp}}^{(i)} - \text{fold-change}(K_A, K_I, R^{(i)}, \Delta\epsilon_{RA}^{(i)}, c^{(i)}))^2}{2\sigma^2} \right], \quad (2.11)$$

where $\text{fold-change}_{\text{exp}}^{(i)}$ is the experimental fold-change and $\text{fold-change}(\dots)$ is the theoretical prediction. The product $\prod_{i=1}^n$ captures the assumption that the n data points are independent. Note that the likelihood and prior terms now include the extra unknown parameter σ . In applying Eq. 2.11, a choice of K_A and K_I that provides better agreement between theoretical fold-change predictions and experimental measurements will result in a more probable likelihood.

Both mathematically and numerically, it is convenient to define $\tilde{k}_A = -\log \frac{K_A}{1M}$ and $\tilde{k}_I = -\log \frac{K_I}{1M}$ and fit for these parameters on a log scale. Dissociation constants are scale invariant, so that a change from $10 \mu M$ to $1 \mu M$ leads to an equivalent increase in affinity as a change from $1 \mu M$ to $0.1 \mu M$. With these definitions we assume for the prior $P(\tilde{k}_A, \tilde{k}_I, \sigma)$ that all three parameters are independent. In addition, we assume a uniform distribution for \tilde{k}_A and \tilde{k}_I and a Jeffreys prior for the scale parameter σ . This yields the complete prior

$$P(\tilde{k}_A, \tilde{k}_I, \sigma) \equiv \frac{1}{(\tilde{k}_A^{\max} - \tilde{k}_A^{\min})} \frac{1}{(\tilde{k}_I^{\max} - \tilde{k}_I^{\min})} \frac{1}{\sigma}. \quad (2.12)$$

These priors are maximally uninformative meaning that they imply no prior knowledge of the parameter values. We defined the \tilde{k}_A and \tilde{k}_I ranges uniform on the range of -7 to 7 , although we note that this particular choice does not affect the outcome provided the chosen range is sufficiently wide.

Putting all these terms together we can now sample from $P(\tilde{k}_A, \tilde{k}_I, \sigma \mid D)$ using Markov chain Monte Carlo to compute the most likely parameter as well as the error bars (given by the 95% credible region) for K_A and K_I .

2.6 Data Curation

All of the data used in this work as well as all relevant code can be found at this dedicated website. Data were collected, stored, and preserved using the Git version control software in combination with off-site storage and hosting website GitHub. Code used to generate all figures and complete all processing step as and analyses are available on the GitHub repository. Many analysis files are stored as instructive Jupyter Notebooks. The scientific community is invited to fork our repositories and open constructive issues on the GitHub repository.

2.7 References

Chapter 3

UNKNOWN KNOWNS, KNOWN UNKNOWNS, AND UNFORSEEN CONSEQUENCES: USING FREE ENERGY SHIFTS TO PREDICT MUTANT PHENOTYPES

A version of this chapter originally appeared as Chure, G; Razo-Mejia, M., Beliveau, N.M.; Kaczmarek, Zofii A.; Einav, T.; Barnes, Stephanie L.; Lewis, M., and Phillips, R. (2019). Predictive Shifts in Free Energy Couple Mutations to Their Phenotypic Consequences. *PNAS* 116(37), G.C., M.R.M, N.M.B., Z.A.K., and S.L.B designed the experiments and collected and analyzed data. G.C. developed theoretical treatment of free energy shifts. G.C., M.R.M, N.M.B., Z.A.K., T.E., S.L.B., and R.P. designed the research project. G.C. and R.P. wrote the paper. M.L. provided guidance and advice.

3.1 Introduction

Thermodynamic treatments of transcriptional regulation have been fruitful in their ability to generate quantitative predictions of gene expression as a function of a minimal set of physically meaningful parameters (Ackers and Johnson, 1982; Bintu et al., 2005a, 2005b; Brewster et al., 2014; Buchler et al., 2003; Daber et al., 2009; Garcia and Phillips, 2011; Kuhlman et al., 2007; Razo-Mejia et al., 2014, 2018; Rydenfelt et al., 2014a; Vilar and Leibler, 2003; Weinert et al., 2014). These models quantitatively describe numerous properties of input-output functions, such as the leakiness, saturation, dynamic range, steepness of response, and the EC_{50} – the concentration of inducer at which the response is half maximal. The mathematical forms of these phenotypic properties are couched in terms of a minimal set of experimentally accessible variables, such as the inducer concentration, transcription factor copy number, and the DNA sequence of the binding site (Razo-Mejia et al., 2018). While the amino acid sequence of the transcription factor is another controllable variable, it is seldom implemented in quantitative terms considering mutations with subtle changes in chemistry frequently yield unpredictable physiological consequences. In this work, we examine how a series of mutations in either the DNA binding or inducer binding domains of a transcriptional repressor influence the values of the biophysical parameters which govern its regulatory behavior.

We build upon the results presented in Chapter 1 of this thesis and present a theoretical framework for understanding how mutations in the amino acid sequence of the repressor affect different parameters and alter the free energy of the system. We find that the parameters capturing the allosteric nature of the repressor, the repressor copy number, and the DNA binding specificity contribute independently to the free energy of the system with different degrees of sensitivity. Furthermore, changes restricted to one of these three groups of parameters result in characteristic changes in the free energy relative to the wild-type repressor, providing falsifiable predictions of how different classes of mutations should behave.

Next, we test these descriptions experimentally using the well-characterized transcriptional repressor of the *lac* operon LacI in *E. coli* regulating expression of a fluorescent reporter. We introduce a series of point mutations in either the inducer binding or DNA binding domain. We then measure the full induction profile of each mutant, determine the minimal set of parameters that are affected by the mutation, and predict how each mutation tunes the free energy at different inducer concentrations, repressor copy numbers, and DNA binding strengths. We find in general that mutations in the DNA binding domain only influence DNA binding strength, and that mutations within the inducer binding domain affect only the parameters which dictate the allosteric response. The degree to which these parameters are insulated is notable, as the very nature of allostery suggests that all parameters are intimately connected, thus enabling binding events at one domain to be “sensed” by another.

With knowledge of how a collection of DNA binding and inducer binding single mutants behave, we predict the induction profiles and the free energy changes of pairwise double mutants with quantitative accuracy. We find that the energetic effects of each individual mutation are additive, indicating that epistatic interactions are absent between the mutations examined here. Our model provides a means for identifying and quantifying the extent of epistatic interactions in a more complex set of mutations, and can shed light on how the protein sequence and general regulatory architecture coevolve.

3.2 Theoretical Model

This work considers the inducible simple repression regulatory motif depicted in Fig. fig. ?? (A) from a thermodynamic perspective which has been thoroughly dissected and tested experimentally (Brewster et al., 2014; Garcia and Phillips, 2011;

Razo-Mejia et al., 2018) and is described in depth in Chapter 1. The result of this extensive theory-experiment dialogue is a succinct input-output function schematized in Fig. fig. ?? (B) that computes the fold-change in gene expression relative to an unregulated promoter. This function is of the form

$$\text{fold-change} = \left(1 + \frac{R_A}{N_{NS}} e^{-\beta \Delta \varepsilon_{RA}} \right)^{-1}, \quad (3.1)$$

where R_A is the number of active repressors per cell, N_{NS} is the number of non-specific binding sites for the repressor, $\Delta \varepsilon_{RA}$ is the binding energy of the repressor to its specific binding site relative to the non-specific background, and β is defined as $\frac{1}{k_B T}$ where k_B is the Boltzmann constant and T is the temperature. While this theory requires knowledge of the number of *active* repressors, we often only know the total number R which is the sum total of active and inactive repressors. We can define a prefactor $p_{\text{act}}(c)$ which captures the allosteric nature of the repressor and encodes the probability a repressor is in the active (repressive) state rather than the inactive state for a given inducer concentration c , namely,

$$p_{\text{act}}(c) = \frac{\left(1 + \frac{c}{K_A}\right)^n}{\left(1 + \frac{c}{K_A}\right)^n + e^{-\beta \Delta \varepsilon_{AI}} \left(1 + \frac{c}{K_I}\right)^n}. \quad (3.2)$$

Here, K_A and K_I are the dissociation constants of the inducer to the active and inactive repressor, $\Delta \varepsilon_{AI}$ is the energetic difference between the repressor active and inactive states, and n is the number of allosteric binding sites per repressor molecule ($n = 2$ for LacI). With this in hand, we can define R_A in Eq. eq. 3.1 as $R_A = p_{\text{act}}(c)R$.

A key feature of Eq. eq. 3.1 and Eq. eq. 3.2 is that the diverse phenomenology of the gene expression induction profile can be collapsed onto a single master curve by rewriting the input-output function in terms of the free energy F also called the Bohr parameter (Phillips, 2015),

$$\text{fold-change} = \frac{1}{1 + e^{-\beta F}}, \quad (3.3)$$

where

$$F = -k_B T \log p_{\text{act}}(c) - k_B T \log \left(\frac{R}{N_{NS}} \right) + \Delta \varepsilon_{RA}. \quad (3.4)$$

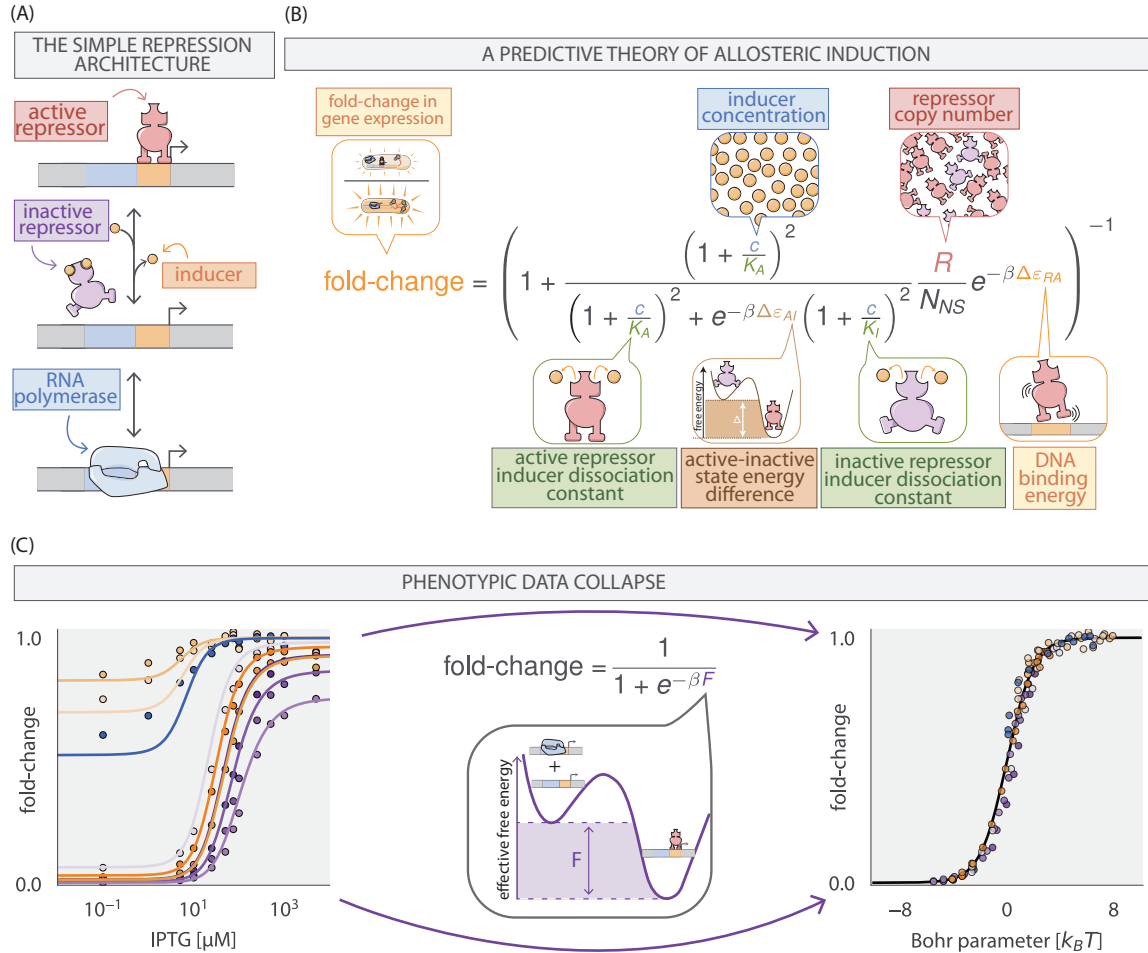


Figure 3.1: A predictive framework for phenotypic and energetic dissection of the simple repression motif. (A) The inducible simple repression architecture. When in the active state, the repressor (red) binds the cognate operator sequence of the DNA (orange box) with high specificity, preventing transcription by occluding binding of the RNA polymerase (blue rectangle). Upon addition of an inducer molecule, the inactive state (purple) becomes energetically preferable, and the repressor no longer binds the operator sequence with appreciable specificity. Once unbound from the operator, binding of the RNA polymerase (blue) is no longer blocked, and transcription can occur. (B) The simple repression input-output function for an allosteric repressor with two inducer binding sites. The key parameters are identified in speech bubbles. (C) The fold change in gene expression collapses as a function of the free energy. Panel (C, left) shows measurements of the fold change in gene expression as a function of inducer concentration from Razo-Mejia et al. (2018). Points and errors correspond to the mean and SEM of at least 10 biological replicates. The thin lines represent the line of best fit given the model shown in (B). This model can be rewritten as a Fermi function with an energetic parameter F , which is the energetic difference between the repressor bound and unbound states of the promoter, schematized in C, Middle. The points in (C), Bottom correspond to the data shown in (C, left) collapsed onto a master curve defined by their calculated free energy F . The solid black line is the master curve defined by the Fermi function shown in (C, Middle)

Hence, if different combinations of parameters yield the same free energy, they will give rise to the same fold-change in gene expression, enabling us to collapse multiple regulatory scenarios onto a single curve. This can be seen in Fig. fig. 3.1 (C) where eighteen unique inducer titration profiles of a LacI simple repression architecture collected and analyzed in Razo-Mejia et al. (2018) collapse onto a single master curve. The tight distribution about this curve reveals that the fold-change across a variety of genetically distinct individuals can be adequately described by a small number of parameters. Beyond predicting the induction profiles of different strains, the method of data collapse inspired by Eq. eq. ?? and Eq. eq. 3.4 can be used as a tool to identify mechanistic changes in the regulatory architecture (Swem et al., 2008). Similar data collapse approaches have been used previously in such a manner and have proved vital for distinguishing between changes in parameter values and changes in the fundamental behavior of the system(??; Swem et al., 2008).

Assuming that a given mutation does not result in a non-functional protein, it is reasonable to say that any or all of the parameters in Eq. eq. 3.1 can be affected by the mutation, changing the observed induction profile and therefore the free energy. To examine how the free energy of a mutant $F^{(\text{mut})}$ differs from that of the wild-type $F^{(\text{wt})}$, we define $\Delta F = F^{(\text{mut})} - F^{(\text{wt})}$, which has the form

$$\Delta F = -k_B T \log \left(\frac{p_{\text{act}}^{(\text{mut})}(c)}{p_{\text{act}}^{(\text{wt})}(c)} \right) - k_B T \log \left(\frac{R^{(\text{mut})}}{R^{(\text{wt})}} \right) + (\Delta \varepsilon_{RA}^{(\text{mut})} - \Delta \varepsilon_{RA}^{(\text{wt})}). \quad (3.5)$$

ΔF describes how a mutation translates a point across the master curve shown in Fig. fig. ?? (C). As we will show in the coming paragraphs (illustrated in Fig. fig. ??), this formulation coarse grains the myriad parameters shown in Eq. eq. 3.1 and Eq. eq. 3.2 into three distinct quantities, each with different sensitivities to parametric changes. By examining how a mutation changes the ΔF as a function of the inducer concentration, one can draw conclusions as to which parameters have been modified based solely on the shape of the curve. To help the reader understand how various perturbations to the parameters tune the free energy, we have hosted an interactive figure on the dedicated website for the publication which makes exploration of parameter space a simpler task.

The first term in Eq. eq. 3.5 is the log ratio of the probability of a mutant repressor being active relative to the wild type at a given inducer concentration c . This

quantity defines how changes to any of the allosteric parameters – such as inducer binding constants K_A and K_I or active/inactive state energetic difference $\Delta\varepsilon_{AI}$ – alter the free energy F , which can be interpreted as the free energy difference between the repressor bound and unbound states of the promoter. Fig. fig. ?? (A) illustrates how changes to the inducer binding constants K_A and K_I alone alter the induction profiles and resulting free energy as a function of the inducer concentration. In the limit where $c = 0$, the values of K_A and K_I do not factor into the calculation of $p_{act}(c)$ given by Eq. eq. 3.2 meaning that $\Delta\varepsilon_{AI}$ is the lone parameter setting the residual activity of the repressor. Thus, if only K_A and K_I are altered by a mutation, then ΔF should be $0 k_B T$ when $c = 0$, illustrated by the overlapping red, purple, and grey curves in the right-hand plot of Fig. fig. ?? (A). However, if $\Delta\varepsilon_{AI}$ is influenced by the mutation (either alone or in conjunction with K_A and K_I), the leakiness will change, resulting in a non-zero ΔF when $c = 0$. This is illustrated in Fig. fig. ?? (B) where $\Delta\varepsilon_{AI}$ is the only parameter affected by the mutation.

It is important to note that for a mutation which perturbs only the inducer binding constants, the dependence of ΔF on the inducer concentration can be non-monotonic. While the precise values of K_A and K_I control the sensitivity of the repressor to inducer concentration, it is the ratio K_A/K_I that defines whether this non-monotonic behavior is observed. This can be seen more clearly when we consider the limit of saturating inducer concentration,

$$\lim_{c \rightarrow \infty} \log \left(\frac{p_{act}^{(mut)}}{p_{act}^{(wt)}} \right) \approx \log \left[\frac{1 + e^{-\beta\Delta\varepsilon_{AI}^{(wt)}} \left(\frac{K_A^{(wt)}}{K_I^{(wt)}} \right)^n}{1 + e^{-\beta\Delta\varepsilon_{AI}^{(wt)}} \left(\frac{K_A^{(mut)}}{K_I^{(mut)}} \right)^n} \right], \quad (3.6)$$

which illustrates that ΔF returns to zero at saturating inducer concentration when the ratio K_A/K_I is the same for both the mutant and wild-type repressors, so long as $\Delta\varepsilon_{AI}$ is unperturbed. Non-monotonicity can *only* be achieved by changing K_A and K_I and therefore serves as a diagnostic for classifying mutational effects reliant solely on measuring the change in free energy. A rigorous proof of this non-monotonic behavior given changing K_A and K_I can be found in supplemental Chapter 7.

The second term in Eq. eq. 3.5 captures how changes in the repressor copy number contributes to changes in free energy. It is important to note that this contribution to the free energy change depends on the total number of repressors in the cell, not just those in the active state. This emphasizes that changes in the expression of

the repressor are energetically divorced from changes to the allosteric nature of the repressor. As a consequence, the change in free energy is constant for all inducer concentrations, as is schematized in Fig. fig. ?? (C). Because the magnitude of the change in free energy scales logarithmically with changing repressor copy number, a mutation which increases expression from 1 to 10 repressors per cell is more impactful from an energetic standpoint ($k_B T \log(10) \approx 2.3 k_B T$) than an increase from 90 to 100 ($k_B T \log(100/90) \approx 0.1 k_B T$). Appreciable changes in the free energy only arise when variations in the repressor copy number are larger than or comparable to an order of magnitude. Changes of this magnitude are certainly possible from a single point mutation, as it has been shown that even synonymous substitutions can drastically change translation efficiency (Frumkin et al., 2018).

The third and final term in Eq. eq. 3.5 is the difference in the DNA binding energy between the mutant and wild-type repressors. All else being equal, if the mutated state binds more tightly to the DNA than the wild type ($\Delta\epsilon_{RA}^{(wt)} > \Delta\epsilon_{RA}^{(mut)}$), the net change in the free energy is negative, indicating that the repressor bound states become more energetically favorable due to the mutation. Much like in the case of changing repressor copy number, this quantity is independent of inducer concentration and is therefore also constant Fig. fig. ?? (D). However, the magnitude of the change in free energy is linear with DNA binding affinity while it is logarithmic with respect to changes in the repressor copy number. Thus, to change the free energy by $1 k_B T$, the repressor copy number must change by a factor of ≈ 2.3 whereas the DNA binding energy must change by $1 k_B T$.

The unique behavior of each quantity in Eq. eq. 3.5 and its sensitivity with respect to the parameters makes ΔF useful as a diagnostic tool to classify mutations. Given a set of fold-change measurements, a simple rearrangement of Eq. eq. ?? permits the direct calculation of the free energy, assuming that the underlying physics of the regulatory architecture has not changed. Thus, it becomes possible to experimentally test the general assertions made in Fig. fig. ??.

3.3 Results

DNA Binding Domain Mutants

With this arsenal of analytic diagnostics, we can begin to explore the mutational space of the repressor and map these mutations to the biophysical parameters they control. As one of the most thoroughly studied transcription factors, LacI has been subjected to numerous crystallographic and mutational studies (??; Daber et al.,

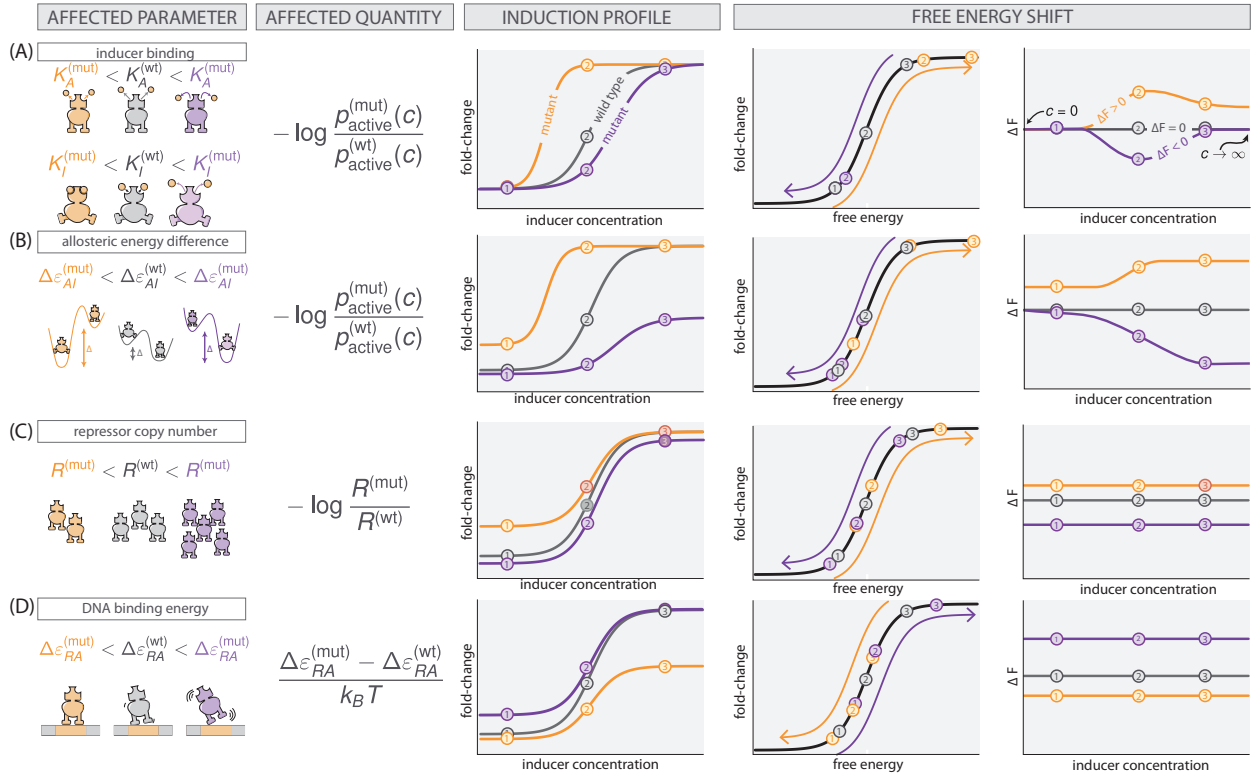


Figure 3.2: Parametric changes due to mutations and the corresponding free-energy changes for (A) perturbations to K_A and K_I , (B) changes to the allosteric energy difference $\Delta\varepsilon_{AI}$, (C) changes to repressor copy number, and (D) changes in DNA binding affinity. The first column schematizes the changed parameters and the second column reflects which quantity in Eq. eq. 3.5 is affected. The third column shows representative induction profiles from mutants which have smaller (purple) and larger (orange) values for the parameters than the wild type (gray). The fourth and fifth columns illustrate how the free energy is changed as a result. Purple and red arrows indicate the direction in which the points are translated about the master curve. Three concentrations (points labeled 1, 2, and 3) are shown to illustrate how each point is moved in free-energy space. An interactive version of this figure can be found on the paper website (https://www.rpgroup.caltech.edu/mwc_mutants).

2009, 2011; Lewis et al., 1996). One such work generated a set of point mutations in the LacI repressor and examined the diversity of the phenotypic response to different allosteric effectors (Daber et al., 2011). However, several experimental variables were unknown, precluding precise calculation of ΔF as presented in the previous section. In Daber et al. (2011), the repressor variants and the fluorescence reporter were expressed from separate plasmids. As the copy numbers of these plasmids fluctuate in the population, both the population average repressor copy number and the number of regulated promoters were unknown. Both of these quantities have been shown previously to significantly alter the measured gene expression and calculation of ΔF is dependent on knowledge of their values. While the approach presented in Daber et al. (2011) considers the Lac repressor as an MWC molecule, the copy numbers of the repressor and the reporter gene were swept into an effective parameter $\frac{R}{K_{DNA}}$, hindering our ability to distinguish between changes in repressor copy number or in DNA binding energy. To test our hypothesis of free energy differences resulting from various parameter perturbations, we used the dataset in Daber et al. (2011) as a guide and chose a subset of the mutations to quantitatively dissect. To control copy number variation, the mutant repressors and the reporter gene were integrated into the *E. coli* chromosome where the copy numbers are known and tightly controlled (Garcia and Phillips, 2011; Razo-Mejia et al., 2018). Furthermore, the mutations were paired with ribosomal binding sites where the level of translation of the wild-type repressor had been directly measured previously (Garcia and Phillips, 2011).

We made three amino acid substitutions (Y17I, Q18A, and Q18M) that are critical for the DNA-repressor interaction. These mutations were introduced into the *lacI* sequence used in Garcia and Phillips (2011) with four different ribosomal binding site sequences that were shown (via quantitative Western blotting) to tune the wild-type repressor copy number across three orders of magnitude. These mutant constructs were integrated into the *E. coli* chromosome harboring a Yellow Fluorescent Protein (YFP) reporter. The YFP promoter included the native O2 LacI operator sequence which the wild-type LacI repressor binds with high specificity ($\Delta\epsilon_{RA} = -13.9 k_B T$). The fold-change in gene expression for each mutant across twelve concentrations of IPTG was measured via flow cytometry. As we mutated only a single amino acid with the minimum number of base pair changes to the codons from the wild-type sequence, we find it unlikely that the repressor copy number was drastically altered from those reported in Garcia and Phillips (2011) for the wild-type sequence paired with the same ribosomal binding site sequence.

In characterizing the effects of these DNA binding mutations, we take the repressor copy number to be unchanged. Any error introduced by this assumption should be manifest as a larger than predicted systematic shift in the free energy change when the repressor copy number is varied.

A naïve hypothesis for the effect of a mutation in the DNA binding domain is that *only* the DNA binding energy is affected. This hypothesis appears to contradict the core principle of allostery in that ligand binding in one domain influences binding in another, suggesting that changing parameter modifies them all. The characteristic curves summarized in Fig. fig. ?? give a means to discriminate between these two hypotheses by examining the change in the free energy. Using a single induction profile (white-faced points in Fig. fig. 3.3), we estimated the DNA binding energy using Bayesian inferential methods, the details of which are thoroughly discussed in the Materials and Methods as well as in the supplemental Chapter 7. The shaded red region for each mutant in Fig. fig. 3.3 represents the 95% credible region of this fit whereas all other shaded regions are 95% credible regions of the predictions for other repressor copy numbers. We find that redetermining only the DNA binding energy accurately captures the majority of the induction profiles, indicating that other parameters are unaffected. One exception is for the lowest repressor copy numbers ($R = 60$ and $R = 124$ per cell) of mutant Q18A at low concentrations of IPTG. However, we note that this disagreement is comparable to that observed for the wild-type repressor binding to the weakest operator in Razo-Mejia et al. (2018), illustrating that our model is imperfect in characterizing weakly repressing architectures. Including other parameters in the fit (such as $\Delta\epsilon_{AI}$) does not significantly improve the accuracy of the predictions. Furthermore, the magnitude of this disagreement also depends on the choice of the fitting strain (see supplemental Chapter 7).

Mutations Y17I and Q18A both weaken the affinity of the repressor to the DNA relative to the wild type strain with binding energies of $-9.9^{+0.1}_{-0.1} k_B T$ and $-11.0^{+0.1}_{-0.1} k_B T$, respectively. Here we report the median of the inferred posterior probability distribution with the superscripts and subscripts corresponding to the upper and lower bounds of the 95% credible region. These binding energies are comparable to that of the wild-type repressor affinity to the native LacI operator sequence O3, with a DNA binding energy of $-9.7 k_B T$. The mutation Q18M increases the strength of the DNA-repressor interaction relative to the wild-type repressor with a binding energy of $-15.43^{+0.07}_{-0.06} k_B T$, comparable to the affinity of the wild-type repressor

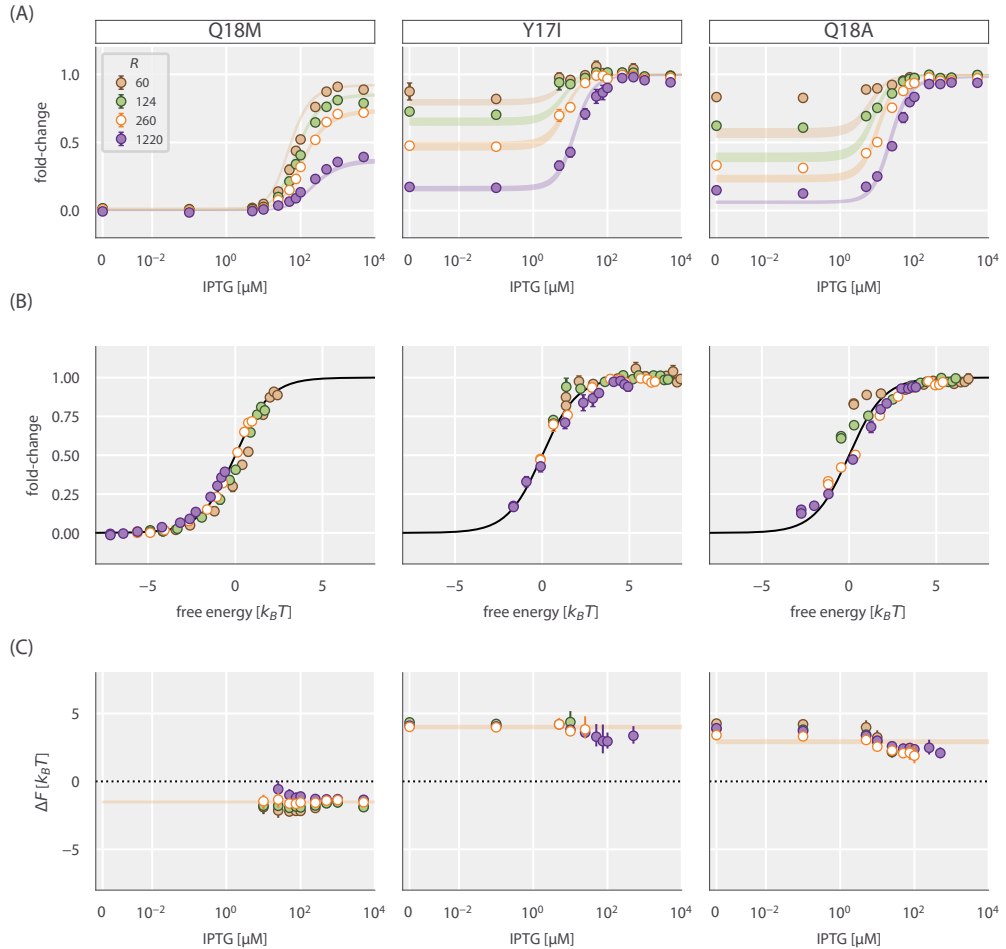


Figure 3.3: Induction profiles and free-energy differences of DNA binding domain mutations. Each column corresponds to the highlighted mutant at the top of the figure. Each strain was paired with the native O2 operator sequence. Open points correspond to the strain for each mutant from which the DNA binding energy was estimated. (A) Induction profiles of each mutant at four different repressor copy numbers as a function of the inducer concentration. Points correspond to the mean fold change in gene expression of 6–10 biological replicates. Error bars are the SEM. Shaded regions demarcate the 95% credible region of the induction profile generated by the estimated DNA binding energy. (B) Data collapse of all points for each mutant shown in A using only the DNA binding energy estimated from a single repressor copy number. Points correspond to the average fold change in gene expression of 6–10 biological replicates. Error bars are SEM. Where error bars are not visible, the relative error in measurement is smaller than the size of the marker. (C) The change in the free energy resulting from each mutation as a function of the inducer concentration. Points correspond to the median of the marginal posterior distribution for the free energy. Error bars represent the upper and lower bounds of the 95% credible region. Points in A at the detection limits of the flow cytometer (near fold-change values of 0 and 1) were neglected for calculation of the ΔF . The IPTG concentration is shown on a symmetric log scale with linear scaling ranging from 0 to $10^{-2} \mu\text{M}$ and log scaling elsewhere. The shaded red lines in C correspond to the 95% credible region of our predictions for ΔF based solely on estimation of $\Delta \varepsilon_{RA}$ from the strain with $R = 260$ repressors per cell.

to the native O1 operator sequence ($-15.3 k_B T$). It is notable that a single amino acid substitution of the repressor is capable of changing the strength of the DNA binding interaction well beyond that of many single base-pair mutations in the operator sequence .

Using the new DNA binding energies, we can collapse all measurements of fold-change as a function of the free energy as shown in Fig. fig. 3.3 (B). This allows us to test the diagnostic power of the decomposition of the free energy described in Fig. fig. ?? . To compute the ΔF for each mutation, we inferred the observed mean free energy of the mutant strain for each inducer concentration and repressor copy number (see Materials and Methods as well as the SI text for a detailed explanation of the inference). We note that in the limit of extremely low or high fold-change, the inference of the free energy is either over- or under-estimated, respectively, introducing a systematic error. Thus, points which are close to these limits are omitted in the calculation of ΔF . We direct the reader to the SI text for a detailed discussion of this systematic error. With a measure of $F^{(\text{mut})}$ for each mutant at each repressor copy number, we compute the difference in free energy relative to the wild-type strain with the same repressor copy number and operator sequence, restricting all variability in ΔF solely to changes in $\Delta \varepsilon_{RA}$.

The change in free energy for each mutant is shown in Fig. fig. 3.3 (C). It can be seen that the ΔF for each mutant is constant as a function of the inducer concentration and is concordant with the prediction generated from fitting $\Delta \varepsilon_{RA}$ to a single repressor copy number red lines Fig. 3.3. This is in line with the predictions outlined in Fig. fig. ?? (C) and (D), indicating that the allosteric parameters are “insulated”, meaning they are not affected by the DNA binding domain mutations. As the ΔF for all repressor copy numbers collapses onto the prediction, we can say that the expression of the repressor itself is the same or comparable with that of the wild type. If the repressor copy number were perturbed in addition to $\Delta \varepsilon_{RA}$, one would expect a shift away from the prediction that scales logarithmically with the change in repressor copy number. However, as the ΔF is approximately the same for each repressor copy number, it can be surmised that the mutation does not significantly change the expression or folding efficiency of the repressor itself. These results allow us to state that the DNA binding energy $\Delta \varepsilon_{RA}$ is the only parameter modified by the DNA mutants examined. ### Inducer Binding Domain Mutants

Much as in the case of the DNA binding mutants, we cannot safely assume *a priori* that a given mutation in the inducer binding domain affects only the inducer

binding constants K_A and K_I . While it is easy to associate the inducer binding constants with the inducer binding domain, the critical parameter in our allosteric model $\Delta\epsilon_{AI}$ is harder to restrict to a single spatial region of the protein. As K_A , K_I , and $\Delta\epsilon_{AI}$ are all parameters dictating the allosteric response, we consider two hypotheses in which inducer binding mutations alter either all three parameters or only K_A and K_I .

We made four point mutations within the inducer binding domain of LacI (F161T, Q291V, Q291R, and Q291K) that have been shown previously to alter binding to multiple allosteric effectors (Daber et al., 2009). In contrast to the DNA binding domain mutants, we paired the inducer binding domain mutations with the three native LacI operator sequences (which have various affinities for the repressor) and a single ribosomal binding site sequence. This ribosomal binding site sequence, as reported in Garcia and Phillips (2011), expresses the wild-type LacI repressor to an average copy number of approximately 260 per cell. As the free energy differences resulting from point mutations in the DNA binding domain can be described solely by changes to $\Delta\epsilon_{RA}$, we continue under the assumption that the inducer binding domain mutations do not significantly alter the repressor copy number.

The induction profiles for these four mutants are shown in Fig. fig. 3.4 (A). Of the mutations chosen, Q291R and Q291K appear to have the most significant impact, with Q291R abolishing the characteristic sigmoidal titration curve entirely. It is notable that both Q291R and Q291K have elevated expression in the absence of inducer compared to the other two mutants paired with the same operator sequence. Panel (A) in Fig. fig. ?? illustrates that if only K_A and K_I were being affected by the mutations, the fold-change should be identical for all mutants in the absence of inducer. This discrepancy in the observed leakiness immediately suggests that more than K_A and K_I are affected for Q291K and Q291R.

Using a single induction profile for each mutant (shown in Fig. fig. 3.4 as white-faced circles), we inferred the parameter combinations for both hypotheses and drew predictions for the induction profiles with other operator sequences. We find that the simplest hypothesis (in which only K_A and K_I are altered) does not permit accurate prediction of most induction profiles. These curves, shown as dotted lines in Fig. fig. 3.4 (A), fail spectacularly in the case of Q291R and Q291K, and undershoot the observed profiles for F161T and Q291V, especially when paired with the weak operator sequence O3. The change in the leakiness for Q291R and Q291K is particularly evident as the expression at $c = 0$ should be identical to

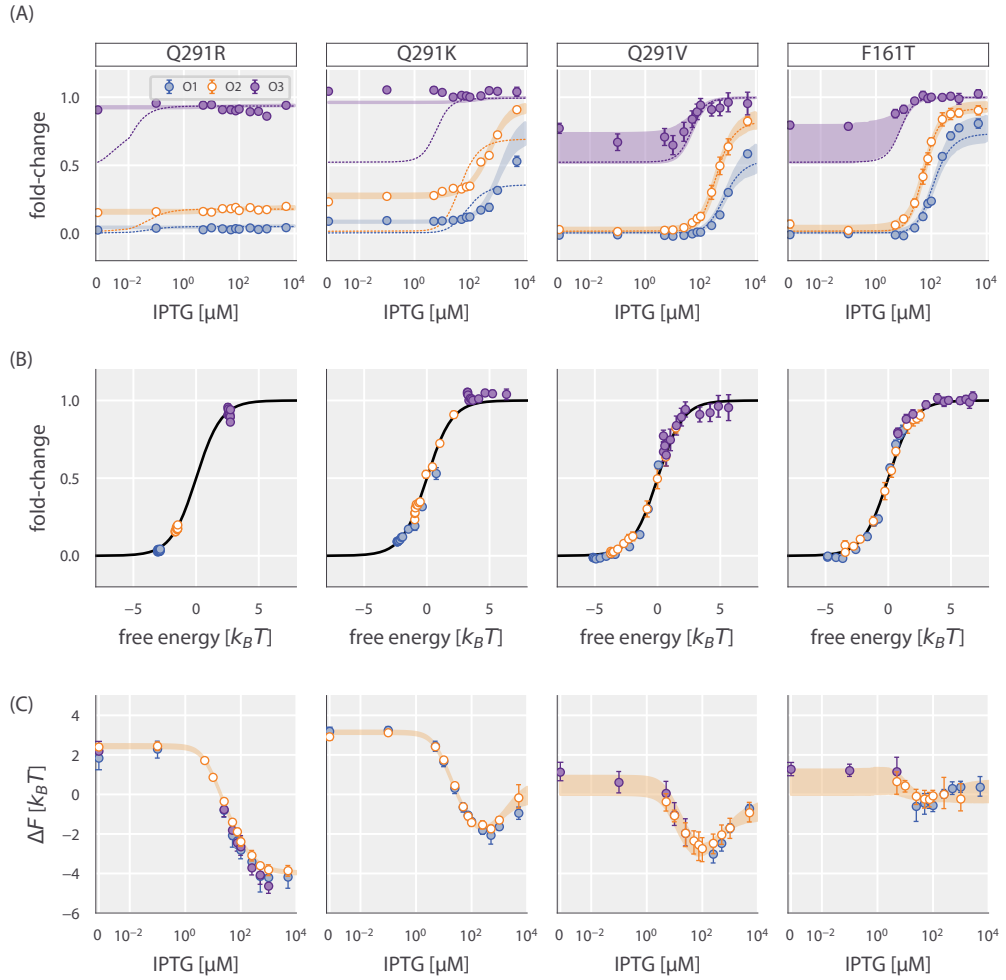


Figure 3.4: Induction profiles and free-energy differences of inducer binding domain mutants. Open points represent the strain to which the parameters were fit — namely, the O2 operator sequence. Each column corresponds to the mutant highlighted at the top of the figure. All strains have $R = 260$ per cell. (A) The fold change in gene expression as a function of the inducer concentration for three operator sequences of varying strength. Dashed lines correspond to the curve of best fit resulting from fitting K_A and K_I alone. Shaded curves correspond to the 95% credible region of the induction profile determined from fitting K_A , K_I , and $\Delta\varepsilon_{AI}$. Points correspond to the mean measurement of 6–12 biological replicates. Error bars are the SEM. (B) Points in A collapsed as a function of the free energy calculated from redetermining K_A , K_I , and $\Delta\varepsilon_{AI}$. (C) Change in free energy resulting from each mutation as a function of the inducer concentration. Points correspond to the median of the posterior distribution for the free energy. Error bars represent the upper and lower bounds of the 95% credible region. Shaded curves are the predictions. IPTG concentration is shown on a symmetric log scaling axis with the linear region spanning from 0 to $10^{-2} \mu\text{M}$ and log scaling elsewhere.

the wild-type repressor under this hypothesis. Altering only K_A and K_I is not sufficient to accurately predict the induction profiles for F161T and Q291V, but not to the same degree as Q291K and Q291R. The disagreement is most evident for the weakest operator O3 green lines in Fig. 3.4, though we have discussed previously that the induction profiles for weak operators are difficult to accurately describe and can result in comparable disagreement for the wild-type repressor (Razo-Mejia et al., 2018).

Including $\Delta\epsilon_{AI}$ as a perturbed parameter in addition to K_A and K_I improves the predicted profiles for all four mutants. By fitting these three parameters to a single strain, we are able to accurately predict the induction profiles of other operators as seen by the shaded lines in Fig. fig. 3.4 (A). With these modified parameters, all experimental measurements collapse as a function of their free energy as prescribed by Eq. eq. ??, Fig. 3.4. All four mutations significantly diminish the binding affinity of both states of the repressor to the inducer, as seen by the estimated parameter values reported in Tab. tbl. 3.1. As evident in the data alone, Q291R abrogates inducibility outright ($K_A \approx K_I$). For Q291K, the active state of the repressor can no longer bind inducer whereas the inactive state binds with weak affinity. The remaining two mutants, Q291V and F161T, both show diminished binding affinity of the inducer to both the active and inactive states of the repressor relative to the wild-type.

Table 3.1: Inferred values of K_A , K_I , and $\Delta\epsilon_{AI}$ for inducer binding mutants

Mutant	K_A	K_I	$\Delta\epsilon_{AI} [k_B T]$	Reference
WT	$139^{+29}_{-22} \mu M$	$0.53^{+0.04}_{-0.04} \mu M$	4.5	Razo-Mejia et al. (2018)
F161T	$165^{+90}_{-65} \mu M$	$3^{+6}_{-3} \mu M$	1^{+5}_{-2}	This study
Q291V	$650^{+450}_{-250} \mu M$	$8^{+8}_{-8} \mu M$	3^{+6}_{-3}	This study
Q291K	$> 1 mM$	$310^{+70}_{-60} \mu M$	$-3.11^{+0.07}_{-0.07}$	This study
Q291R	$9^{+20}_{-9} \mu M$	$8^{+20}_{-8} \mu M$	$-2.35^{+0.01}_{-0.09}$	This study

Given the collection of fold-change measurements, we computed the ΔF relative to the wild-type strain with the same operator and repressor copy number. This leaves differences in $p_{act}(c)$ as the sole contributor to the free energy difference, assuming our hypothesis that K_A , K_I , and $\Delta\epsilon_{AI}$ are the only perturbed parameters is correct. The change in free energy can be seen in Fig. fig. 3.4 (C). For all mutants,

the free energy difference inferred from the observed fold-change measurements falls within error of the predictions generated under the hypothesis that K_A , K_I , and $\Delta\varepsilon_{AI}$ are all affected by the mutation [shaded curves in Fig. fig. 3.4 (C)]. The profile of the free energy change exhibits some of the rich phenomenology illustrated in Fig. fig. ?? (A) and (B). Q291K, F161T, and Q291V exhibit a non-monotonic dependence on the inducer concentration, a feature that can only appear when K_A and K_I are altered. The non-zero ΔF at $c = 0$ for Q291R and Q291K coupled with an inducer concentration dependence is a telling sign that $\Delta\varepsilon_{AI}$ must be significantly modified. This shift in ΔF is positive in all cases, indicating that $\Delta\varepsilon_{AI}$ must have decreased, and that the inactive state has become more energetically favorable for these mutants than for the wild-type protein. Indeed the estimates for $\Delta\varepsilon_{AI}$ (Tab. tbl. 3.1) reveal both mutations Q291R and Q291K make the inactive state more favorable than the active state. Thus, for these two mutations, only $\approx 10\%$ of the repressors are active in the absence of inducer, whereas the basal active fraction is $\approx 99\%$ for the wild-type repressor (Razo-Mejia et al., 2018).

We note that the parameter values reported here disagree with those reported in Daber et al. (2011). This disagreement stems from different assumptions regarding the residual activity of the repressor in the absence of inducer and the parametric degeneracy of the MWC model without a concrete independent measure of $\Delta\varepsilon_{AI}$. A detailed discussion of the difference in parameter values between our previous work (??; Garcia and Phillips, 2011), that of Daber et al. (2011), and those of other seminal works can be found in the supplemental Chapter 7.

Taken together, these parametric changes diminish the response of the regulatory architecture as a whole to changing inducer concentrations. They furthermore reveal that the parameters which govern the allosteric response are interdependent and no single parameter is insulated from the others. However, as *only* the allosteric parameters are changed, one can say that the allosteric parameters as a whole are insulated from the other components which define the regulatory response, such as repressor copy number and DNA binding affinity.

Predicting Effects of Pairwise Double Mutations

Given full knowledge of each individual mutation, we can draw predictions of the behavior of the pairwise double mutants with no free parameters based on the simplest null hypothesis of no epistasis. The formalism of ΔF defined by Eq. eq:delF explicitly states that the contribution to the free energy of the system from

the difference in DNA binding energy and the allosteric parameters are strictly additive. Thus, deviations from the predicted change in free energy would suggest epistatic interactions between the two mutations.

To test this additive model, we constructed nine double mutant strains, each having a unique inducer binding (F161T, Q291V, Q291K) and DNA binding mutation (Y17I, Q18A, Q18M). To make predictions with an appropriate representation of the uncertainty, we computed a large array of induction profiles given random draws from the posterior distribution for the DNA binding energy (determined from the single DNA binding mutants) as well as from the joint posterior for the allosteric parameters (determined from the single inducer binding mutants). These predictions, shown in Fig. fig. 3.5 (A) and (B) as shaded blue curves, capture all experimental measurements of the fold-change Fig. 3.5 and the inferred difference in free energy Fig. 3.5. The latter indicates that there are no epistatic interactions between the mutations queried in this work, though if there were, systematic deviations from these predictions would shed light on how the epistasis is manifest.

The precise agreement between the predictions and measurements for Q291K paired with either Q18A or Q18M is striking as Q291K drastically changed $\Delta\varepsilon_{AI}$ in addition to K_A and K_I . Our ability to predict the induction profile and free energy change underscores the extent to which the DNA binding energy and the allosteric parameters are insulated from one another. Despite this insulation, the repressor still functions as an allosteric molecule, emphasizing that the mutations we have inserted do not alter the pathway of communication between the two domains of the protein. As the double mutant Y17I-Q291K exhibits fold-change of approximately 1 across all IPTG concentrations Fig. 3.5, these mutations in tandem make repression so weak it is beyond the limits which are detectable by our experiments. As a consequence, we are unable to estimate ΔF nor experimentally verify the corresponding prediction grey box in Fig. 3.5. However, as the predicted fold-change in gene expression is also approximately 1 for all c , we believe that the prediction shown for ΔF is likely accurate. One would be able to infer the ΔF to confirm these predictions using a more sensitive method for measuring the fold-change, such as single-cell microscopy or colorimetric assays.

3.4 Discussion

Allosteric regulation is often couched as “biological action at a distance”. Despite extensive knowledge of protein structure and function, it remains difficult to

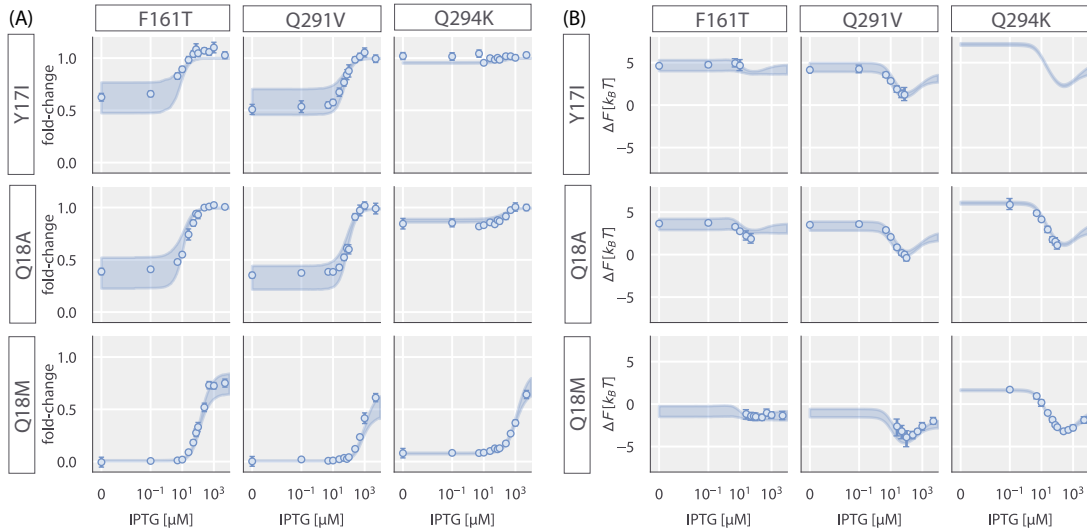


Figure 3.5: Induction and free-energy profiles of DNA binding and inducer binding double mutants. (A) Fold change in gene expression for each double mutant as a function of IPTG. Points and errors correspond to the mean and SE of 6–10 biological replicates. Where not visible, error bars are smaller than the corresponding marker. Shaded regions correspond to the 95% credible region of the prediction given knowledge of the single mutants. These were generated by drawing 10^4 samples from the $\Delta\epsilon_{RA}$ posterior distribution of the single DNA binding domain mutants and the joint probability distribution of K_A , K_I , and $\Delta\epsilon_{AI}$ from the single inducer binding domain mutants. (B) The difference in free energy of each double mutant as a function of the reference free energy. Points and errors correspond to the median and bounds of the 95% credible region of the posterior distribution for the inferred ΔF . Shaded lines region are the predicted change in free energy, generated in the same manner as the shaded lines in A. All measurements were taken from a strain with 260 repressors per cell paired with a reporter with the native O2 LacI operator sequence. In all plots, the IPTG concentration is shown on a symmetric log axis with linear scaling between 0 and $10^{-2} \mu\text{M}$ and log scaling elsewhere.

translate the coordinates of the atomic constituents of a protein to the precise parameter values which define the functional response, making each mutant its own intellectual adventure. Bioinformatic approaches to understanding the sequence-structure relationship have permitted us to examine how the residues of allosteric proteins evolve, revealing conserved regions which hint to their function. Co-evolving residues reveal sectors of conserved interactions which traverse the protein that act as the allosteric communication channel between domains (??; ???; Reynolds et al., 2011). Elucidating these sectors has advanced our understanding of how distinct domains “talk” to one another and has permitted direct engineering of allosteric responses into non-allosteric enzymes (??; Poelwijk et al., 2011; Raman et al., 2016). Even so, we are left without a quantitative understanding of how these admittedly complex networks set the energetic difference between active and inactive states or how a given mutation influences binding affinity. In this context, a biophysical model in which the various parameters are intimately connected to the molecular details can be of use and can lead to quantitative predictions of the interplay between amino-acid identity and system-level response.

By considering how each parameter contributes to the observed change in free energy, we are able to tease out different classes of parameter perturbations which result in stereotyped responses to changing inducer concentration. These characteristic changes to the free energy can be used as a diagnostic tool to classify mutational effects. For example, we show in Fig. fig. ?? that modulating the inducer binding constants K_A and K_I results in non-monotonic free energy changes that are dependent on the inducer concentration, a feature observed in the inducer binding mutants examined in this work. Simply looking at the inferred ΔF as a function of inducer concentration, which requires no fitting of the biophysical parameters, indicates that K_A and K_I must be modified considering those are the only parameters which can generate such a response.

Another key observation is that a perturbation to only K_A and K_I requires that the $\Delta F = 0 k_B T$ at $c = 0$. Deviations from this condition imply that more than the inducer binding constants must have changed. If this shift in ΔF off of $0 k_B T$ at $c = 0$ is not constant across all inducer concentrations, we can surmise that the energy difference between the allosteric states $\Delta \varepsilon_{AI}$ must also be modified. We again see this effect for all of our inducer mutants. By examining the inferred ΔF , we can immediately say that in addition to K_A and K_I , $\Delta \varepsilon_{AI}$ must decrease relative to the wild-type value as $\Delta F > 0$ at $c = 0$. When the allosteric parameters are fit to

the induction profiles, we indeed see that this is the case, with all four mutations decreasing the energy gap between the active and inactive states. Two of these mutations, Q291R and Q291K, make the inactive state of the repressor *more* stable than the active state, which is not the case for the wild-type repressor (Razo-Mejia et al., 2018).

Our formulation of ΔF indicates that shifts away from $0 k_B T$ that are independent of the inducer concentration can only arise from changes to the repressor copy number and/or DNA binding specificity, indicating that the allosteric parameters are untouched. We see that for three mutations in the DNA binding domain, ΔF is the same irrespective of the inducer concentration. Measurements of ΔF for these mutants with repressor copy numbers across three orders of magnitude yield approximately the same value, revealing that $\Delta\varepsilon_{RA}$ is the sole parameter altered via the mutations.

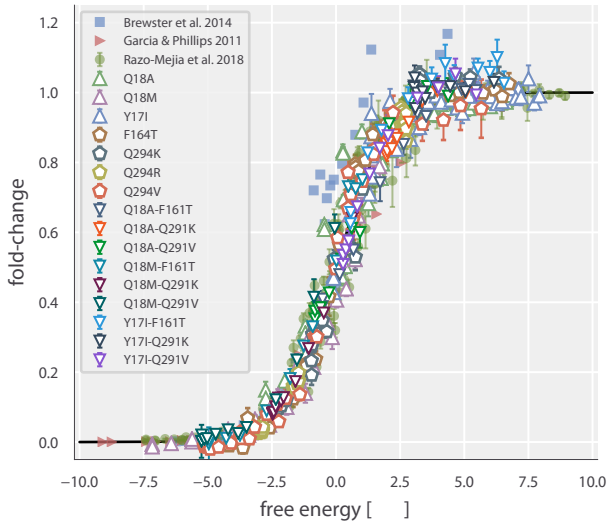
We note that the conclusions stated above can be qualitatively drawn without resorting to fitting various parameters and measuring the goodness-of-fit. Rather, the distinct behavior of ΔF is sufficient to determine which parameters are changing. Here, these conclusions are quantitatively confirmed by fitting these parameters to the induction profile, which results in accurate predictions of the fold-change and ΔF for nearly every strain across different mutations, repressor copy numbers, and operator sequence, all at different inducer concentrations. With a collection of evidence as to what parameters are changing for single mutations, we put our model to the test and drew predictions of how double mutants would behave both in terms of the titration curve and free energy profile.

A hypothesis that arises from our formulation of ΔF is that a simple summation of the energetic contribution of each mutation should be sufficient to predict the double mutants (so long as they are in separate domains). We find that such a calculation permits precise and accurate predictions of the double mutant phenotypes, indicating that there are no epistatic interactions between the mutations examined in this work. With an expectation of what the free energy differences should be, epistatic interactions could be understood by looking at how the measurements deviate from the prediction. For example, if epistatic interactions exist which appear as a systematic shift from the predicted ΔF independent of inducer concentration, one could conclude that DNA binding energy is not equal to that of the single mutation in the DNA binding domain alone. Similarly, systematic shifts that are dependent on the inducer concentration (i.e. not constant) indicate that the

allosteric parameters must be influenced. If the expected difference in free energy is equal to $0 k_B T$ when $c = 0$, one could surmise that the modified parameter must not be $\Delta\epsilon_{AI}$ nor $\Delta\epsilon_{RA}$ as these would both result in a shift in leakiness, indicating that K_A and K_I are further modified.

Ultimately, we present this work as a proof-of-principle for using biophysical models to investigate how mutations influence the response of allosteric systems. We emphasize that such a treatment allows one to boil down the complex phenotypic responses of these systems to a single-parameter description which is easily interpretable as a free energy. The general utility of this approach is illustrated in Fig. fig. ?? where gene expression data from previous work along with all of the measurements presented in this work collapse onto the master curve defined by Eq. eq. ???. While our model coarse grains many of the intricate details of transcriptional regulation into two states (one in which the repressor is bound to the promoter and one where it is not), it is sufficient to describe a swath of regulatory scenarios. As discussed in the supplemental Chapter 7, any architecture in which the transcription-factor bound and transcriptionally active states of the promoter can be separated into two distinct coarse-grained states can be subjected to such an analysis.

Given enough parametric knowledge of the system, it becomes possible to examine how modifications to the parameters move the physiological response along this reduced one-dimensional parameter space. This approach offers a glimpse at how mutational effects can be described in terms of energy rather than Hill coefficients and arbitrary prefactors. While we have explored a very small region of sequence space in this work, coupling of this approach with high-throughput sequencing-based methods to query a library of mutations within the protein will shed light on the phenotypic landscape centered at the wild-type sequence. Furthermore, pairing libraries of protein and operator sequence mutants will provide insight as to how the protein and regulatory sequence coevolve, a topic rich with opportunity for a dialogue between theory and experiment.



Materials & Methods

Bacterial Strains and DNA Constructs

All wild-type strains from which the mutants were derived were generated in previous work from the Phillips group (Garcia and Phillips, 2011; Razo-Mejia et al., 2018). Briefly, mutations were first introduced into the *lacI* gene of our pZS3*1-lacI plasmid (Garcia and Phillips, 2011) using a combination of overhang PCR Gibson assembly as well as QuickChange mutagenesis (Agilent Technologies). The oligonucleotide sequences used to generate each mutant as well as the method are provided in the supplemental Chapter 7.

For mutants generated through overhang PCR and Gibson assembly, oligonucleotide primers were purchased containing an overhang with the desired mutation and used to amplify the entire plasmid. Using the homology of the primer overhang, Gibson assembly was performed to circularize the DNA prior to electroporation into MG1655 *E. coli* cells. Integration of LacI mutants was performed with λ Red recombineering as described in Sharan et al. (2009) and Garcia and Phillips (2011).

The mutants studied in this work were chosen from data reported in Daber et al. (2011). In selecting mutations, we looked for mutants which suggested moderate to strong deviations from the behavior of the wild-type repressor. We note that the variant of LacI used in this work has an additional three amino acids (Met-Val-Asn) added to the N-terminus than the canonical LacI sequence reported in (???). To remain consistent with the field, we have identified the mutations with respect to their positions in the canonical sequence and those in Daber et al. (2011). However, their positions in the raw data files correspond to that of our LacI variant

and is noted in the README files associated with the data.

Flow Cytometry

All fold-change measurements were performed on a MACSQuant flow cytometer as described in Razo-Mejia et al. (2018). Briefly, saturated overnight cultures 500 μ L in volume were grown in deep-well 96 well plates covered with a breathable nylon cover (Lab Pak - Nitex Nylon, Sefar America, Cat. No. 241205). After approximately 12 to 15 hr, the cultures reached saturation and were diluted 1000-fold into a second 2 mL 96-deep-well plate where each well contained 500 μ L of M9 minimal media supplemented with 0.5% w/v glucose (anhydrous D-Glucose, Macron Chemicals) and the appropriate concentration of IPTG (Isopropyl β -D-1-thiogalactopyranoside, Dioxane Free, Research Products International). These were sealed with a breathable cover and were allowed to grow for approximately 8 hours until the $OD_{600nm} \approx 0.3$. Cells were then diluted ten-fold into a round-bottom 96-well plate (Corning Cat. No. 3365) containing 90 μ L of M9 minimal media supplemented with 0.5% w/v glucose along with the corresponding IPTG concentrations.

The flow cytometer was calibrated prior to use with MACSQuant Calibration Beads (Cat. No. 130-093-607). During measurement, the cultures were held at approximately 4° C by placing the 96-well plate on a MACSQuant ice block. All fluorescence measurements were made using a 488 nm excitation wavelength with a 525/50 nm emission filter. The photomultiplier tube voltage settings for the instrument are the same as those used in Razo-Mejia et al. (2018) and are listed in supplemental Chapter 6.

The data was processed using an automatic unsupervised gating procedure based on the front and side-scattering values, where we fit a two-dimensional Gaussian function to the \log_{10} forward-scattering (FSC) and the \log_{10} side-scattering (SSC) data. Here we assume that the region with highest density of points in these two channels corresponds to single-cell measurements and consider data points that fall within 40% of the highest density region of the two-dimensional Gaussian function. We direct the reader to Reference (Razo-Mejia et al., 2018) for further detail and comparison of flow cytometry with single-cell microscopy.

Bayesian Parameter Estimation

We used a Bayesian definition of probability in the statistical analysis of all mutants in this work. In the SI text, we derive in detail the statistical models used for the

various parameters as well as multiple diagnostic tests. Here, we give a generic description of our approach. To be succinct in notation, we consider a generic parameter θ which represents $\Delta\varepsilon_{RA}$, K_A , K_I , and/or $\Delta\varepsilon_{AI}$ depending on the specific LacI mutant.

As prescribed by Bayes' theorem, we are interested in the posterior probability distribution

$$g(\theta | y) \propto f(y | \theta)g(\theta), \quad (3.7)$$

where we use g and f to represent probability densities over parameters and data, respectively, and y to represent a set of fold-change measurements. The likelihood of observing our dataset y given a value of θ is captured by $f(y | \theta)$. All prior information we have about the possible values of θ are described by $g(\theta)$.

In all inferential models used in this work, we assumed that all experimental measurements at a given inducer concentration were normally distributed about a mean value μ dictated by Eq. eq. 3.1 with a variance σ^2 ,

$$f(y | \theta) = \frac{1}{(2\pi\sigma^2)^{N/2}} \prod_i^N \exp \left[-\frac{(y_i - \mu(\theta))^2}{2\sigma^2} \right], \quad (3.8)$$

where N is the number of measurements in the data set y .

This choice of likelihood is justified as each individual measurement at a given inducer concentration is a biological replicate and independent of all other experiments. By using a Gaussian likelihood, we introduce another parameter σ . As σ must be positive and greater than zero, we define as a prior distribution a half-normal distribution with a standard deviation ϕ ,

$$g(\sigma) = \frac{1}{\phi} \sqrt{\frac{2}{\pi}} \exp \left[-\frac{x}{2\phi^2} \right]; x \geq 0, \quad (3.9)$$

where x is a given range of values for σ . A standard deviation of $\phi = 0.1$ was chosen given our knowledge of the scale of our measurement error from other experiments. As the absolute measurement of fold-change is restricted between 0 and 1.0, and given our knowledge of the sensitivity of the experiment, it is reasonable to assume that the error will be closer to 0 than to 1.0. Further justification

of this choice of prior through simulation based methods are given in the supplemental Chapter 7. The prior distribution for θ is dependent on the parameter and its associated physical and physiological restrictions. Detailed discussion of our chosen prior distributions for each model can also be found in the supplemental Chapter 7.

All statistical modeling and parameter inference was performed using Markov chain Monte Carlo (MCMC). Specifically, Hamiltonian Monte Carlo sampling was used as is implemented in the Stan probabilistic programming language (Carpenter et al., 2017). All statistical models saved as .stan models and can be accessed at the GitHub repository associated with this work (DOI: 10.5281/zenodo.2721798) or can be downloaded directly from the paper website.

Inference of Free Energy From Fold-Change Data

While the fold-change in gene expression is restricted to be between 0 and 1, experimental noise can generate fold-change measurements beyond these bounds. To determine the free energy for a given set of fold-change measurements (for one unique strain at a single inducer concentration), we modeled the observed fold-change measurements as being drawn from a normal distribution with a mean μ and standard deviation σ . Using Bayes' theorem, we can write the posterior distribution as

$$g(\mu, \sigma | y) \propto g(\mu)g(\sigma) \frac{1}{(2\pi\sigma^2)^{N/2}} \prod_i^N \exp \left[\frac{-(y_i - \mu)^2}{2\sigma^2} \right] \quad (3.10)$$

where y is a collection of fold-change measurements. The prior distribution for μ was chosen to be uniform between 0 and 1 while the prior on σ was chosen to be half normal, as written in Eq. @eq:sigma_prior. The posterior distribution was sampled independently for each set of fold-change measurements using MCMC. The .stan model for this inference is available on the paper website.

For each MCMC sample of μ , the free energy was calculated as

$$F = -\log (\mu^{-1} - 1) \quad (3.11)$$

which is simply the rearrangement of Eq. eq. ???. Using simulated data, we determined that when $\mu < \sigma$ or $(1 - \mu) < \sigma$, the mean fold-change in gene expression was over or underestimated for the lower and upper limit, respectively. This

means that there are maximum and minimum levels of fold-change that can be detected using flow cytometry which are set by the distribution of fold-change measurements resulting from various sources of day-to-day variation. This results in a systematic error in the calculation of the free energy, making proper inference beyond these limits difficult. This bounds the range in which we can confidently infer this quantity with flow cytometry. We hypothesize that more sensitive methods, such as single cell microscopy, colorimetric assays, or direct counting of mRNA transcripts via Fluorescence *In Situ* Hybridization (FISH) would improve the measurement of ΔF . We further discuss details of this limitation in the supplemental Chapter 7.

Data and Code Availability

All data was collected, stored, and preserved using the Git version control software. Code for data processing, analysis, and figure generation is available on the GitHub repository (https://www.github.com/rpgroup-pboc/mwc_mutants%7D%7Bhttps://www.github.com/rpgroup-pboc/mwc_mutants) or can be accessed via the paper website. Raw flow cytometry data is stored on the CaltechDATA data repository and can be accessed via DOI 10.22002/D1.1241.

3.5 References

Chapter 4

IGNORANCE IS BLISS: PHYSIOLOGICAL ADAPTABILITY OF A SIMPLE GENETIC CIRCUIT

A version of this chapter is currently under review. A preprint is released as Chure, G; Kaczmarek, Z. A.; Phillips, R. *The Physiological Adaptability of a Simple Genetic Circuit.* bioRxiv 2019. G.C. and R.P. designed experiments and developed theoretical models. G.C. and Z.A.K. collected and analyzed data. G.C. and R.P. wrote the paper.

4.1 Introduction

Cellular physiology is inextricably tied to the extracellular environment. Fluctuations in nutrient availability and variations in temperature, for example, can drastically modulate the cell's growth rate, which is often used as a measure of the evolutionary fitness (???). In response to such environmental insults, cells have evolved myriad clever mechanisms by which they can adapt to their changing surroundings, many of which involve restructuring their proteome such that critical processes (i.e. protein translation) are allocated the necessary resources. Recent work exploring this level of adaptation using mass spectrometry, ribosomal profiling, and RNA sequencing have revealed that various classes of genes (termed "sectors") are tuned such that the protein mass fraction of the translational machinery is prioritized over the metabolic and catabolic machinery in nutrient replete environments (Hui et al., 2015; Klumpp and Hwa, 2014; Li et al., 2014; Schmidt et al., 2016; Scott et al., 2014). This drastic reorganization is mediated by the regulation of gene expression, relying on the concerted action of myriad transcription factors. Notably, each gene in isolation is regulated by only one or a few components (Gama-Castro et al., 2016). The most common regulatory architecture in *Escherichia coli* is the simple repression motif in which a transcriptional repressor binds to a single site in the promoter region, occluding binding of an RNA polymerase (Phillips et al., 2019; Rydenfelt et al., 2014b). The simple activation architecture, in which the simultaneous binding of an activator and an RNA polymerase amplifies gene expression, is another common mode of regulation. Combinatorial regulation such as dual repression, dual activation, or combined activation and repression can also be found throughout the genome, albeit with lower frequency(Phillips et al.,

2019). The ubiquity of the simple repression and simple activation motifs illustrate that, for many genes, the complex systems-level response to a physiological perturbation boils down the binding and unbinding of a single regulator to its cognate binding sites.

Despite our knowledge of these modes of regulation, there remains a large disconnect between concrete, physical models of their behavior and experimental validation. The simple repression motif is perhaps the most thoroughly explored theoretically and experimentally (Phillips et al., 2019) where equilibrium thermodynamic (Barnes et al., 2019; Brewster et al., 2014; Garcia and Phillips, 2011; Garcia et al., 2012; Razo-Mejia et al., 2018) and kinetic (Jones et al., 2014; Kepler and Elston, 2001; Ko, 1991; Michel, 2010) models have been shown to accurately predict the level of gene expression in a variety of contexts. While these experiments involved variations of repressor copy number, operator sequence, concentration of an external inducer, and amino acid substitutions, none have explored how the physiological state of the cell as governed by external factors influences gene expression. This is arguably one of the most critical variables one can experimentally tune to understand the role of these regulatory architectures play in cellular physiology writ large.

In this work, we interrogate the adaptability of a simple genetic circuit to various physiological stressors, namely carbon source quality and growth temperature. Following the aforementioned thermodynamic models, we build upon this theory-experiment dialogue by using environmental conditions as an experimentally tunable variable and determine their influence on various biophysical parameters. Specifically, we use physiological stressors to tune the growth rate. One mechanism by which we modulate the growth rate is by exchanging glucose in the growth medium for the poorer carbon sources glycerol and acetate, which decrease the growth rate by a factor of ≈ 1.5 and ≈ 4 compared to glucose, respectively. We hypothesize that different carbon sources should, if anything, only modulate the repressor copy number seeing as the relationship between growth rate and total protein content has been rigorously quantified (???: Jun et al., 2018; Li et al., 2014; Schmidt et al., 2016). Using single-cell time-lapse fluorescence microscopy, we directly measure the copy number of the repressor in each condition. Under a simple hypothesis, all other parameters should be unperturbed, and we can thus rely on previously determined values to make parameter-free predictions of the fold-change in gene expression.

Despite the decrease in growth rate, both the fold-change in gene expression and the repressor copy number remains largely unaffected. We confirm this is the case by examining how the effective free energy of the system changes between carbon sources, a method we have used previously to elucidate parametric changes due to mutations within a transcription factor (Chure et al., 2019) and has been extensively discussed in Chapter 3. This illustrates that the energetic parameters defining the fraction of active repressors and their affinity for the DNA are ignorant of the carbon-dependent physiological states of the cell. Thus, in this context, the values of the biophysical parameters determined in one condition can be used to draw predictions in others.

We then examine how variations in temperature influence the transcriptional output. Unlike in the case of carbon source variation, temperature dependence is explicit in our model: the repressor-DNA binding energy and the energetic difference between the active and inactive states of the repressor are scaled to the thermal energy of the system at 37° C. This is defined via the Boltzmann distribution which states that the probability of a state p_{state} is related to the energy of that state ϵ_{state} as

$$p_{state} \propto e^{-\epsilon_{state}/k_B T}, \quad (4.1)$$

where k_B is the Boltzmann constant and T is the temperature of the system. Given knowledge of T for a particular experiment, we can easily draw predictions of the fold-change in gene expression. However, we find the fold-change in gene expression is inconsistent with this simple model, revealing an incomplete description of the energetics. We then examine how entropic effects neglected in the initial estimation of the energetic parameters may play an important role; a hypothesis that is supported when we examine the change in the effective free energy.

The results presented here are, to our knowledge, the first attempts to systematically characterize the growth-dependent effects on biophysical parameters in thermodynamic models of transcription. While some parameters of our model are affected by changing the growth rate, they change in ways that are expected or fall close within our *a priori* predictions, suggesting that such modeling can still be powerful in understanding how adaptive processes influence physiology at the level of molecular interactions.

Chapter 5

'WATER, WATER EVERYWHERE, NOR ANY DROP TO DRINK': HOW BACTERIA ADAPT TO CHANGES IN OSMOLARITY

A version of this chapter was published as Chure, G.* , Lee, H.J.* , Rasmussen, A., and Phillips, R. (2018). *Connecting the Dots between Mechanosensitive Channel Abundance, Osmotic Shock, and Survival at Single-Cell Resolution*. Journal of Bacteriology 200. (* contributed equally). G.C., H.J.L, and R.P. designed and planned experiments. G.C. and H.J.L performed experiments. H.J.L constructed bacterial strains. A.R. performed electrophysiology experiments. G.C. performed data analysis and figure generation. G.C. and R.P. wrote the manuscript

5.1 Introduction

Changes in the extracellular osmolarity can be a fatal event for the bacterial cell. Upon a hypo-osmotic shock, water rushes into the cell across the membrane, leaving the cell with no choice but to equalize the pressure. This equalization occurs either through damage to the cell membrane (resulting in death) or through the regulated flux of water molecules through transmembrane protein channels (Fig 1A). Such proteinaceous pressure release valves have been found across all domains of life, with the first bacterial channel being described in 1987 (Martinac et al., 1987). Over the past thirty years, several more channels have been discovered, described, and (in many cases) biophysically characterized. *E. coli*, for example, has seven of these channels (one MscL and six MscS homologs) which have varied conductance, gating mechanisms, and expression levels. While they have been the subject of much experimental and theoretical dissection, much remains a mystery with regard to the roles their abundance and interaction with other cellular processes play in the greater context of physiology (Bavi et al., 2016; Bialecka-Fornal et al., 2012, 2015; Edwards et al., 2012; Naismith and Booth, 2012; Ursell et al., 2008; van den Berg et al., 2016).

Of the seven channels in *E. coli*, the mechanosensitive channel of large conductance (MscL) is one of the most abundant and the best characterized. This channel has a large conductance (3 nS) and mediates the flux of water molecules across the membrane via a ~3 nm wide pore in the open state (Cruickshank et al., 1997; Haswell et al., 2011). Molecular dynamics simulations indicate that a single

open MscL channel permits the flux of 4×10^9 water molecules per second, which is an order of magnitude larger than a single aquaporin channel (BNID 100479) (Louhivuori et al., 2010; Milo et al., 2010). This suggests that having only a few channels per cell could be sufficient to relieve even large changes in membrane tension. Electrophysiological experiments have suggested a small number of channels per cell (Booth et al., 2005; Hase et al., 1997), however, more recent approaches using quantitative Western blotting, fluorescence microscopy, and proteomics have measured several hundred MscL per cell (Bialecka-Fornal et al., 2012; Schmidt et al., 2016; Soufi et al., 2015). To further complicate matters, the expression profile of MscL appears to depend on growth phase, available carbon source, and other environmental challenges (Bialecka-Fornal et al., 2012; Soufi et al., 2015; Stokes et al., 2003). While there are likely more than just a few channels per cell, why cells seem to need so many and the biological rationale behind their condition-dependent expression both remain a mystery.

While their biochemical and biophysical characteristics have received much attention, their connection to cell survival is understudied. Drawing such a direct connection between channel copy number and survival requires quantitative *in vivo* experiments. To our knowledge, the work presented in van den Berg et al. 2016 (van den Berg et al., 2016) is the first attempt to simultaneously measure channel abundance and survivability for a single species of mechanosensitive channel. While the measurement of channel copy number was performed at the level of single cells using super-resolution microscopy, survivability after a hypoosmotic shock was assessed in bulk plating assays which rely on serial dilutions of a shocked culture followed by counting the number of resulting colonies after incubation. Such bulk assays have long been the standard for querying cell viability after an osmotic challenge. While they have been highly informative, they reflect only the mean survival rate of the population, obfuscating the variability in survival of the population. The stochastic nature of gene expression results in a noisy distribution of MscL channels rather than a single value, meaning those found in the long tails of the distribution have quite different survival rates than the mean but are lost in the final calculation of survival probability.

In this work, we present an experimental system to quantitatively probe the interplay between MscL copy number and survival at single-cell resolution, as is seen in Fig. 5.1B. We generated an *E. coli* strain in which all seven mechanosensitive channels had been deleted from the chromosome followed by a chromosomal

integration of a single gene encoding an MscL-super-folder GFP (sfGFP) fusion protein. To explore copy number regimes beyond those of the wild-type expression level, we modified the Shine-Dalgarno sequence of this integrated construct, allowing us to cover nearly three decades of MscL copy number. To probe survivability, we exposed cells to a large hypo-osmotic shock at controlled rates in a flow cell under a microscope, allowing the observation of the single-cell channel copy number and the resulting survivability of single cells. With this large set of single cell measurements, we approach the calculation of survival probability in a manner that is free of binning bias which allows the reasonable extrapolation of survival probability to copy numbers outside of the observed range. In addition, we show that several hundred channels are needed to convey high rates of survival and observe a minimum number of channels needed to permit any degree of survival.

5.2 Results

Quantifying the single-cell MscL copy number

The principal goal of this work is to examine the contribution of a single mechanosensitive channel species to cell survival under a hypo-osmotic shock. While this procedure could be performed for any species of channel, we chose MscL as it is the most well characterized and one of the most abundant species in *E. coli*. To probe the contribution of MscL alone, we integrated an *mscL* gene encoding an MscL super-folder GFP (sfGFP) fusion into a strain in which all seven known mechanosensitive channel genes were deleted from the chromosome (Edwards et al., 2012). Chromosomal integration imposes strict control on the gene copy number compared to plasmid borne expression systems, which is important to minimize variation in channel expression across the population and provide conditions more representative of native cell physiology. Abrogation of activity, mislocalization, or cytotoxicity are all inherent risks associated with creating chimeric reporter constructs. In Supplement A, we carefully dissect the functionality of this protein through electrophysiology (Fig. S1), measure the rate of fluorophore maturation (Fig. S2), and quantify potential aggregates (Figs. S3 and S4). To the best of our knowledge, the MscL-sfGFP fusion protein functions identically to the wild-type, allowing us to confidently draw conclusions about the physiological role this channel plays in wild-type cells.

To modulate the number of MscL channels per cell, we developed a series of mutants which were designed to decrease the expression relative to wild-type. These

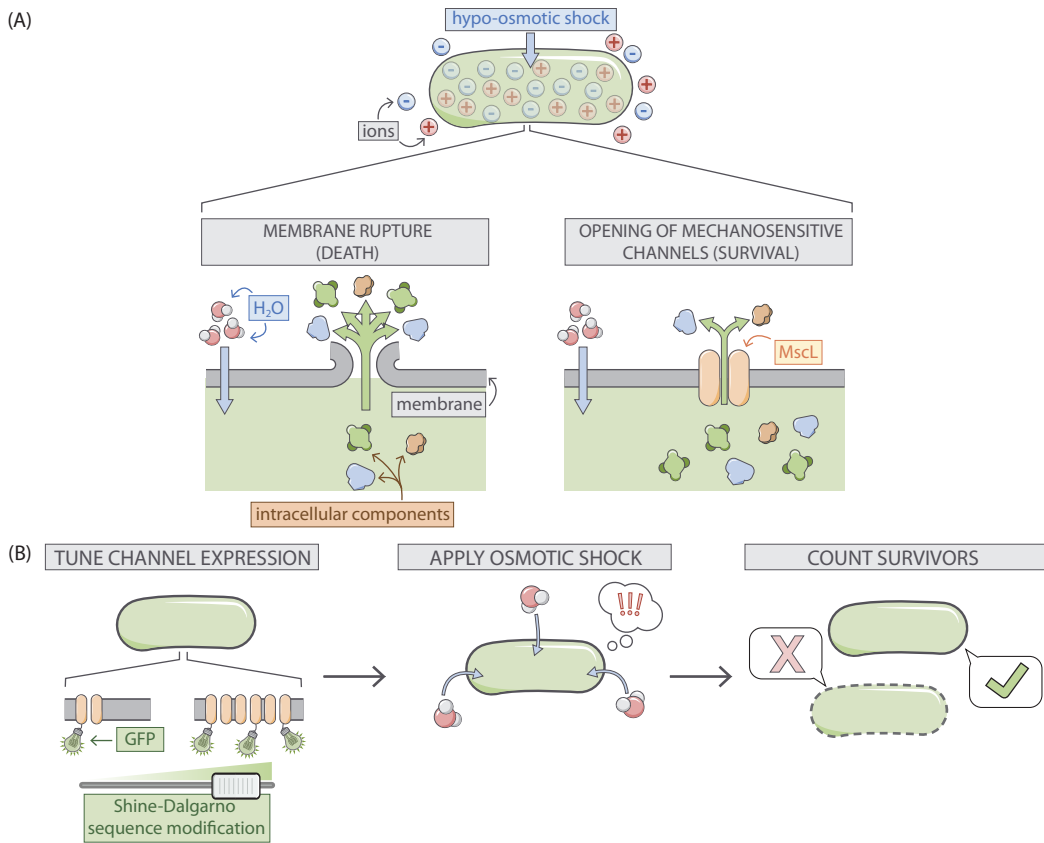


Figure 5.1: Role of mechanosensitive channels during hypo-osmotic shock. (A) A hypo-osmotic shock results in a large difference in the osmotic strength between the intracellular and extracellular spaces. As a result, water rushes into the cell to equalize this gradient increasing the turgor pressure and tension in the cell membrane. If no mechanosensitive channels are present and membrane tension is high (left panel), the membrane ruptures releasing intracellular content into the environment resulting in cell death . If mechanosensitive channels are present (right panel) and membrane tension is beyond the gating tension, the mechanosensitive channel MscL opens, releasing water and small intracellular molecules into the environment thus relieving pressure and membrane tension. (B) The experimental approach undertaken in this work. The number of mechanosensitive channels tagged with a fluorescent reporter is tuned through modification of the Shine-Dalgarno sequence of the *mscL* gene. The cells are then subjected to a hypo-osmotic shock and the number of surviving cells are counted, allowing the calculation of a survival probability.

changes involved direct alterations of the Shine-Dalgarno sequence as well as the inclusion of AT hairpins of varying length directly upstream of the start codon which influences the translation rate and hence the number of MscL proteins produced Fig. 5.2. The six Shine-Dalgarno sequences used in this work were chosen using the RBS binding site strength calculator from the Salis Laboratory at the Pennsylvania State University (Espah Borujeni et al., 2014; Salis et al., 2009). While the designed Shine-Dalgarno sequence mutations decreased the expression relative to wild-type as intended, the distribution of expression is remarkably wide spanning an order of magnitude.

To measure the number of MscL channels per cell, we determined a fluorescence calibration factor to translate arbitrary fluorescence units per cell to protein copy number. While there have been numerous techniques developed over the past decade to directly measure this calibration factor, such as quantifying single-molecule photobleaching constants or measuring the binomial partitioning of fluorescent proteins upon cell division (Bialecka-Fornal et al., 2012; Elowitz et al., 2002), we used *a priori* knowledge of the mean MscL-sfGFP expression level of a particular *E. coli* strain to estimate the average fluorescence of a single channel. In Bialecka-Fornal et al. 2012 (Bialecka-Fornal et al., 2012), the authors used single-molecule photobleaching and quantitative Western blotting to probe the expression of MscL-sfGFP under a wide range of growth conditions. To compute a calibration factor, we used the strain MLG910 (*E. coli* K12 MG1655 $\phi(mscL\text{-sfGFP})$) as a “standard candle”, highlighted in white in Fig. fig. 5.2 (B). This standard candle strain was grown and imaged in identical conditions in which the MscL count was determined through fluorescence microscopy. The calibration factor was computed by dividing the mean total cell fluorescence by the known MscL copy number, resulting in a measure of arbitrary fluorescence units per MscL channel. Details regarding this calculation and appropriate propagation of error as well as its sensitivity to varying growth media can be found in the Materials & Methods as well as Supplement B (Fig. S5 - S8).

While it is seemingly straightforward to use this calibration factor to determine the total number of channels per cell for wild-type or highly expressing strains, the calculation for the lowest expressing strains is complicated by distorted cell morphology. We observed that as the channel copy number decreases, cellular morphology becomes increasingly aberrant with filamentous, bulging, and branched cells becoming more abundant (Fig. S7A). This morphological defect has been ob-

served when altering the abundance of several species of mechanosensitive channels, suggesting that they play an important role in general architectural stability (Bialecka-Fornal et al., 2012, 2015). As these aberrant morphologies can vary widely in size and shape, calculating the number of channels per cell becomes a more nuanced endeavor. For example, taking the total MscL copy number for these cells could skew the final calculation of survival probability as a large but severely distorted cell would be interpreted as having more channels than a smaller, wild-type shaped cell (Fig. S7B). To correct for this pathology, we computed the average expression level per unit area for each cell and multiplied this by the average cellular area of our standard candle strain which is morphologically indistinguishable from wild-type *E. coli*, allowing for the calculation of an effective channel copy number. The effect of this correction can be seen in Fig. S7C and D, which illustrate that there is no other correlation between cell area and channel expression.

Our calculation of the effective channel copy number for our suite of Shine-Dalgarno mutants is shown in Fig. fig. 5.2(B). The expression of these strains cover nearly three orders of magnitude with the extremes ranging from approximately four channels per cell to nearly one thousand. While the means of each strain are somewhat distinct, the distributions show a large degree of overlap, making one strain nearly indistinguishable from another. This variance is a quantity that is lost in the context of bulk scale experiments but can be accounted for via single-cell methods.

Performing a single-cell hypo-osmotic challenge assay

To measure the channel copy number of a single cell and query its survival after a hypo-osmotic shock, we used a custom-made flow cell in which osmotic shock and growth can be monitored in real time using video microscopy Fig. 5.3. The design and characterization of this device has been described in depth previously and is briefly described in the Materials & Methods (Bialecka-Fornal et al., 2015). Using this device, cells were exposed to a large hypo-osmotic shock by switching between LB Lennox medium supplemented with 500 mM NaCl and LB Lennox media alone. All six Shine-Dalgarno modifications shown in Fig. fig. 5.2(B) (excluding MLG910) were subjected to a hypo-osmotic shock at controlled rates while under observation. After the application of the osmotic shock, the cells were imaged every sixty seconds for four to six hours. Each cell was monitored over the outgrowth period and was manually scored as either a survivor, fatality, or inconclusive observation. The criteria used for scoring death were the same as those

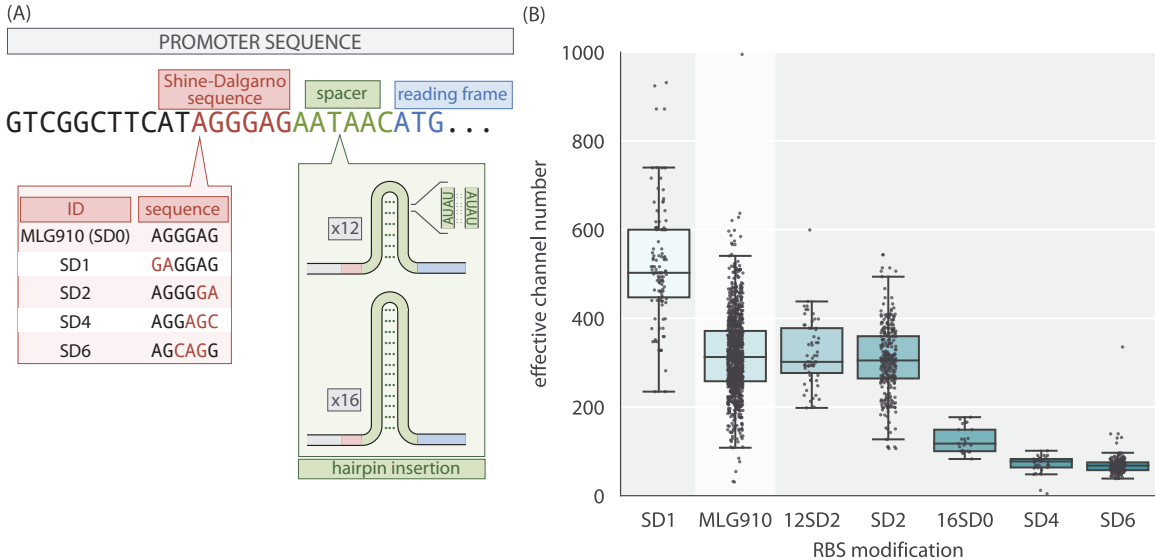


Figure 5.2: Control of MscL expression and calculation of channel copy number. (A) Schematic view of the expression modifications performed in this work. The beginning portion of the native *mscL* sequence is shown with the Shine-Dalgarno sequence, spacer region, and start codon shaded in red, green, and blue, respectively. The Shine-Dalgarno sequence was modified through the Salis lab Ribosomal Binding Strength calculator (Espah Borujeni et al., 2014; Salis et al., 2009). The wild-type sequence (MLG910) is shown in black with mutations for the other four Shine-Dalgarno mutants highlighted in red. Expression was further modified by the insertion of repetitive AT bases into the spacer region, generating hairpins of varying length which acted as a thermodynamic barrier for translation initiation. (B) Variability in effective channel copy number is computed using the standard candle. The boxes represent the interquartile region of the distribution, the center line displays the median, and the whiskers represent 1.5 times the maximum and minimum of the interquartile region. Individual measurements are denoted as black points. The strain used for calibration of channel copy number (MLG910) is highlighted in yellow.

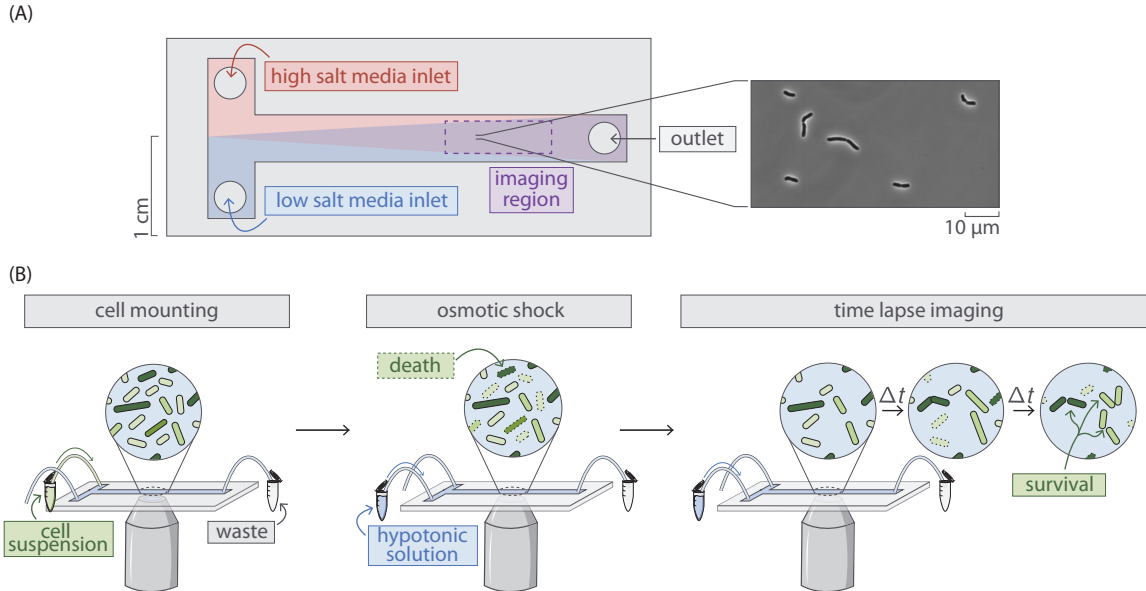


Figure 5.3: Experimental approach to measuring survival probability. (A) Layout of a home-made flow cell for subjecting cells to osmotic shock. Cells are attached to a polyethylenimine functionalized surface of a glass coverslip within the flow chamber by loading a dilute cell suspension through one of the inlets. (B) The typical experimental procedure. Cells are loaded into a flow chamber as shown in (A) and mounted to the glass coverslip surface. Cells are subjected to a hypo-osmotic shock by flowing hypotonic medium into the flow cell. After shock, the cells are monitored for several hours and surviving cells are identified.

previously described in Bialecka-Fornal et al. 2015 (Bialecka-Fornal et al., 2015). Survivors were defined as cells that underwent multiple divisions post-shock. To qualify as survivors, cells must undergo at least two divisions, although more typically, four to eight divisions are observed without any signs of slowing down. Imaging is stopped when the survivors cells begin to go out of focus or overlap each other. Survivors do not show any sign of ceasing division. More information regarding this classification can be found in the Materials and Methods as well as the Supplementary Information (Fig. S9 - S10 and Table S1 - S2). The brief experimental protocol can be seen in Fig. fig. 5.3(B).

Due to the extensive overlap in expression between the different Shine-Dalgarno mutants see Fig. 5.2, computing the survival probability by treating each mutant as an individual bin obfuscates the relationship between channel abundance and survival. To more thoroughly examine this relationship, all measurements were pooled together with each cell being treated as an individual experiment. The hypo-osmotic shock applied in these experiments was varied across a range of

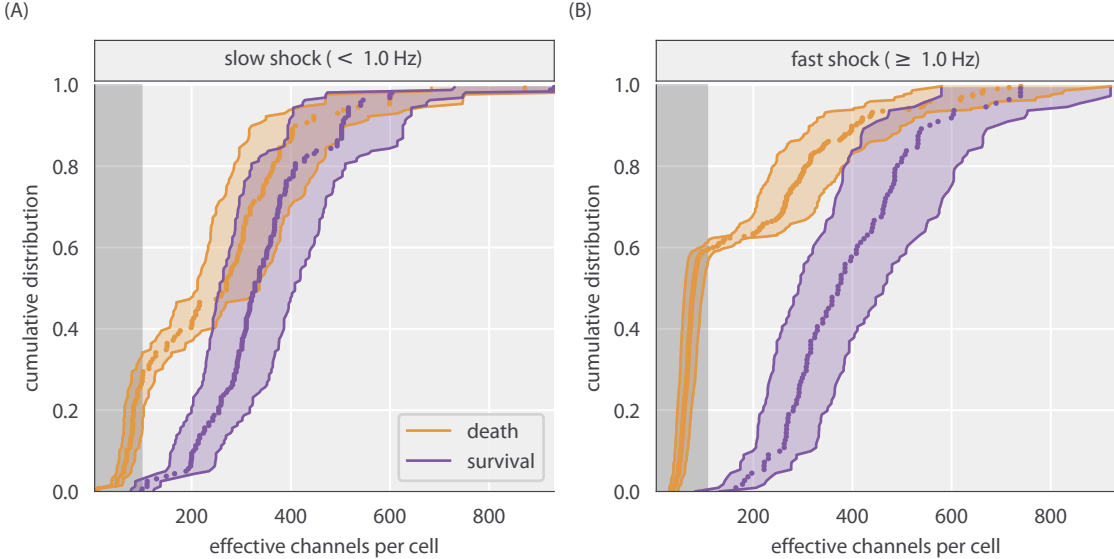


Figure 5.4: Distributions of survival and death as a function of effective channel number. (A) Empirical cumulative distributions of channel copy number separated by survival (green) or death (purple) after a slow ($< 1.0 \text{ Hz}$) osmotic shock. (B) The empirical cumulative distribution for a fast ($\geq 1.0 \text{ Hz}$) osmotic shock. Shaded green and purple regions represent the 95% credible region of the effective channel number calculation for each cell. Shaded red stripe signifies the range of channels in which no survival was observed.

0.02 Hz (complete exchange in 50 s) to 2.2 Hz (complete exchange in 0.45 s). Rather than pooling this wide range of shock rates into a single data set, we chose to separate the data into “slow shock” ($< 1.0 \text{ Hz}$) and “fast shock” ($\geq 1.0 \text{ Hz}$) classes. Other groupings of shock rate were explored and are discussed in Supplement D (Fig. S11 and S12). The cumulative distributions of channel copy number separated by survival are shown in Fig. fig. 5.4. In these experiments, survival was never observed for a cell containing less than approximately 100 channels per cell, indicated by the red stripe in Fig. fig. 5.4. This suggests that there is a minimum number of channels needed for survival on the order of 100 per cell. We also observe a slight shift in the surviving fraction of the cells towards higher effective copy number, which matches our intuition that including more mechanosensitive channels increases the survival probability.

Prediction of survival probability as a function of channel copy number

There are several ways by which the survival probability can be calculated. The most obvious approach would be to group each individual Shine-Dalgarno

mutant as a single bin and compute the average MsCL copy number and the survival probability. Binning by strain is the most frequently used approach for such measurements and has provided valuable insight into the qualitative relationship of survival on other physiological factors (Bialecka-Fornal et al., 2015; van den Berg et al., 2016). However the copy number distribution for each Shine-Dalgarno mutant Fig. 5.2 is remarkably wide and overlaps with the other strains. We argue that this coarse-grained binning negates the benefits of performing single-cell measurements as two strains with different means but overlapping quartiles would be treated as distinctly different distributions.

Another approach would be to pool all data together, irrespective of the Shine-Dalgarno mutation, and bin by a defined range of channels. Depending on the width of the bin, this could allow for finer resolution of the quantitative trend, but the choice of the bin width is arbitrary with the *a priori* knowledge that is available. Drawing a narrow bin width can easily restrict the number of observed events to small numbers where the statistical precision of the survival probability is lost. On the other hand, drawing wide bins increases the precision of the estimate, but becomes further removed from a true single-cell measurement and represents a population mean, even though it may be a smaller population than binning by the Shine-Dalgarno sequence alone. In both of these approaches, it is difficult to extrapolate the quantitative trend outside of the experimentally observed region of channel copy number. Here, we present a method to estimate the probability of survival for any channel copy number, even those that lie outside of the experimentally queried range.

To quantify the survival probability while maintaining single-cell resolution, we chose to use a logistic regression model which does not require grouping data into arbitrary bins and treats each cell measurement as an independent experiment. Logistic regression is an inferential method to model the probability of a Boolean or categorical event (such as survival or death) given one or several predictor variables and is commonly used in medical statistics to compute survival rates and dose response curves (Anderson et al., 2003; Mishra et al., 2016). The primary assumption of logistic regression is that the log-odds probability of survival p_s is linearly dependent on the predictor variable, in our case the log channels per cell N_c with a dimensionless intercept β_0 and slope β_1 ,

$$\log \frac{p_s}{1 - p_s} = \beta_0 + \beta_1 \log N_c. \quad (5.1)$$

Under this assumption of linearity, β_0 is the log-odds probability of survival with no MscL channels. The slope β_1 represents the change in the log-odds probability of survival conveyed by a single channel. As the calculated number of channels in this work spans nearly three orders of magnitude, it is better to perform this regression on $\log N_c$ as regressing on N_c directly would give undue weight for lower channel copy numbers due to the sparse sampling of high-copy number cells. The functional form shown in Eq. eq. 5.1 can be derived directly from Bayes' theorem and is shown in Supplement E. If one knows the values of β_0 and β_1 , the survival probability can be expressed as

$$p_s = \frac{1}{1 + N_c^{-\beta_1} e^{-\beta_0}}. \quad (5.2)$$

In this analysis, we used Bayesian inferential methods to determine the most likely values of the coefficients and is described in detail in the Supplement E (Fig. S13 and S14).

The results of the logistic regression are shown in Fig. fig. 5.5. We see a slight rightward shift the survival probability curve under fast shock relative to the slow shock case, reaffirming the conclusion that survival is also dependent on the rate of osmotic shock (Bialecka-Fornal et al., 2015). This rate dependence has been observed for cells expressing MscL alongside other species of mechanosensitive channels, but not for MscL alone. This suggests that MscL responds differently to different rates of shock, highlighting the need for further study of rate dependence and the coordination between different species of mechanosensitive channels. Fig. fig. 5.5 also shows that several hundred channels are required to provide appreciable protection from osmotic shock. For a survival probability of 80%, a cell must have approximately 500 to 700 channels per cell for a fast and slow shock, respectively. The results from the logistic regression are showed as continuous colored curves. The individual cell measurements separated by survival and death are shown at the top and bottom of each plot, respectively, and are included to provide a sense of sampling density.

Over the explored range of MscL copy number, we observed a maximum of 80% survival for any binning method. The remaining 20% survival may be attained when the other species of mechanosensitive channels are expressed alongside MscL. However, it is possible that the flow cell method performed in this work lowers the maximal survival fraction as the cells are exposed to several, albeit minor, mechanical stresses such as loading into the flow cell and chemical adherence to the glass

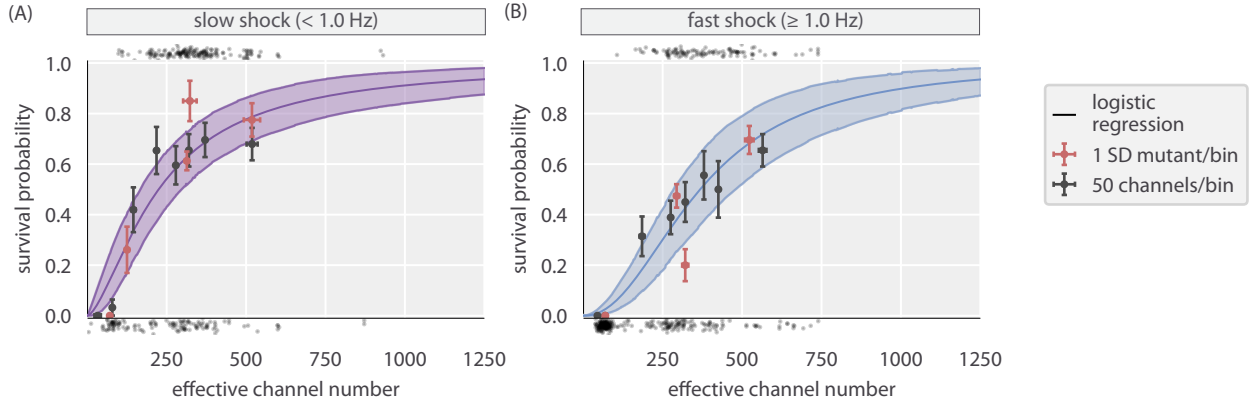


Figure 5.5: Probability of survival as a function of *MscL* copy number. (A) Estimated survival probability for survival under slow shock as a function of channel copy number. (B) The estimated survival probability of survival under a fast shock as a function of channel copy number. Solid curves correspond to the most probable survival probability from a one-dimensional logistic regression. Shaded regions represent the 95% credible regions. Points at the top and bottom of plots represent individual cell measurements which survived and perished, respectively. The red and black points correspond to the survival probability estimated via binning by Shine-Dalgarno sequence and binning by groups of 50 channels per cell, respectively. Horizontal error bars represent the standard error of the mean from at least 25 measurements. Vertical error bars represent the certainty of the probability estimate given n survival events from N total observations.

surface. To ensure that the results from logistic regression accurately describe the data, we can compare the survival probabilities to those using the binning methods described earlier (red and black points, Fig. fig. 5.5). Nearly all binned data fall within error of the prediction (see Materials and Methods for definition of error bar on probability), suggesting that this approach accurately reflects the survival probability and gives license to extrapolate the estimation of survival probability to regions of outside of our experimentally explored copy number regime.

Thus far, we've dictated that for a given rate of osmotic shock (i.e. "fast" or "slow"), the survival probability is dependent only on the number of channels. In Fig. S13, we show the result of including other predictor variables, such as area and shock rate alone. In such cases, including other predictors resulted in pathological curves showing that channel copy number is the most informative out of the available predictor variables.

5.3 Discussion

One of the most challenging endeavors in the biological sciences is linking the microscopic details of cellular components to the macro-scale physiology of the organism. This formidable task has been met repeatedly in the recent history of biology, especially in the era of DNA sequencing and single molecule biochemistry. For example, the scientific community has been able to connect sickle-cell anemia to a single amino acid substitution in Hemoglobin which promotes precipitation under a change in O₂ partial pressure (Feeling-Taylor et al., 2004; Finch et al., 1973; Perutz and Mitchison, 1950). Others have assembled a physical model that quantitatively describes chemosensation in bacteria (Berg and Purcell, 1977) in which the arbiter of sensory adaptation is the repeated methylation of chemoreceptors (Colin and Sourjik, 2017; Krembel et al., 2015a, 2015b; Sourjik and Berg, 2002). In the past ~50 years alone, numerous biological and physical models of the many facets of the central dogma have been assembled that give us a sense of the interplay between the genome and physiology. For example, the combination of biochemical experimentation and biophysical models have given us a picture of how gene dosage affects furrow positioning in *Drosophila* (Liu et al., 2013), how recombination of V(D)J gene segments generates an extraordinarily diverse antibody repertoire (Lovely et al., 2015; Schatz and Baltimore, 2004; Schatz and Ji, 2011), and how telomere shortening through DNA replication is intrinsically tied to cell senescence (Herbig et al., 2004; Victorelli and Passos, 2017), to name just a few of many such examples.

By no means are we “finished” with any of these topics. Rather, it’s quite the opposite in the sense that having a handle on the biophysical knobs that tune the behavior opens the door to a litany of new scientific questions. In the case of mechanosenstation and osmoregulation, we have only recently been able to determine some of the basic facts that allow us to approach this fascinating biological phenomenon biophysically. The dependence of survival on mechanosensitive channel abundance is a key quantity that is missing from our collection of critical facts. To our knowledge, this work represents the first attempt to quantitatively control the abundance of a single species of mechanosensitive channel and examine the physiological consequences in terms of survival probability at single-cell resolution. Our results reveal two notable quantities. First, out of the several hundred single-cell measurements, we never observed a cell which had less than approximately 100 channels per cell and survived an osmotic shock, irrespective of the shock rate. The second is that between 500 and 700 channels per cell are needed

to provide $\geq 80\%$ survival, depending on the shock rate.

Only recently has the relationship between the MscL copy number and the probability of survival been approached experimentally. In van den Berg et al. (2016), the authors examined the contribution of MscL to survival in a genetic background where all other known mechanosensitive channels had been deleted from the chromosome and plasmid-borne expression of an MscL-mEos3.2 fusion was tuned through an IPTG inducible promoter (van den Berg et al., 2016). In this work, they measured the single-cell channel abundance through super-resolution microscopy and queried survival through bulk assays. They report a nearly linear relationship between survival and copy number, with approximately 100 channels per cell conveying 100% survival. This number is significantly smaller than our observation of approximately 100 channels as the *minimum* number needed to convey an observable degree of survival.

The disagreement between the numbers reported in this work and in van den Berg et al. may partially arise from subtle differences in the experimental approach. The primary practical difference is the magnitude of the osmotic shock. van den Berg et al. applied an approximately 600 mOsm downshock in bulk whereas we applied a 1 Osm downshock, which would lead to lower survival (Levina et al., 1999). In their work, the uncertainty in both the MscL channel count and survival probability is roughly 30% (Fig. S14). Given this uncertainty, it is reasonable to interpret that the number of channels needed for complete protection from osmotic downshock is between 100 and 250 per cell. The uncertainty in determining the number of channels per cell is consistent with the observed width of the channel number distribution of the Shine-Dalgarno sequence mutants used in this work Fig. 5.2. A unique property of the single-cell measurements performed in this work allow is the direct observation of survival or death of individual cells. We find that morphological classification and classification through a propidium iodide staining agree within 1% (Supplement C). The bulk plating assays, as are used in van den Berg et al., rely on colony formation and outgrowth to determine survival probability. As is reported in their supplemental information, the precision in this measurement is around 30% (Fig. S14). Accounting for this uncertainty brings both measurements within a few fold where we still consistently observe lower survival for a given channel number. This remaining disagreement may be accounted for by systematic uncertainty in both experimental methods.

For example, variation in the length of outgrowth, variable shock rate, and count-

ing statistics could bias towards higher observed survival rates in ensemble plating assays. During the outgrowth phase, the control sample not exposed to an osmotic shock is allowed to grow for approximately 30 minutes in a high-salt medium before plating. The shocked cells, however, are allowed to grow in a low-salt medium. We have found that the difference between the growth rates in these two conditions can be appreciable (approximately 35 minutes versus 20 minutes, respectively) as can be seen in Fig S2. Cells that survived an osmotic shock may have a growth advantage relative to the control sample if the shock-induced lag phase is less than the outgrowth, leading to higher observed survival rates (Levina et al., 1999). This is one possible explanation for the survival rates which are reported in excess of 100%. Cells that survived an osmotic shock may have a growth advantage relative to the normalization sample if the shock-induced lag phase is less than the outgrowth, leading to higher observed survival rates, even surpassing 100%. We have performed these assays ourselves and have observed survival rates above of 100% (ranging from 110% to 125%) with an approximate 30% error (see Fig. S3 in Bialecka-Fornal et al. 2012 (Bialecka-Fornal et al., 2012)) which we concluded to arise from differences in growth rate. We also note that survival rates greater than 100% are observed in van den Berg et al. (Fig. S14). For strains that have survival rates between 80% and 100% the uncertainty is typically large, making it difficult to make precise statements regarding when full survival is achieved.

It has been shown that there is a strong inverse relationship between the rate of osmotic shock and survival probability (Bialecka-Fornal et al., 2015). Any experiment in which the shock was applied more slowly or quickly than another would bias toward higher or lower survivability, respectively. The shocks applied in bulk assays are often performed manually which can be highly variable. We note that in our experiments, we frequently observe cells which do not separate and form chains of two or more cells (Fig. S9 and S10). In plating assays, it is assumed that colonies arise from a single founding cell however a colony formed by a cluster of living and dead cells would be interpreted as a single surviving cell, effectively masking the death of the others in the colony forming unit. This too could bias the measurement toward higher survival rates. Single-cell shock experiments can also have systematic errors which can bias the results towards lower survival rates. Such errors are associated with handling of the cells such as shear damage from loading into the flow cell, adhering the cells to the coverslip, and any chemical perturbations introduced by the dye used to measure the shock rate.

Despite these experimental differences, the results of this work and van den Berg et al., are in agreement that MscL must be present at the level of 100 or more channels per cell in wild-type cells to convey appreciable survival. As both of these works were performed in a strain in which the only mechanosensitive channel was MscL, it remains unknown how the presence of the other channel species would alter the number of MscL needed for complete survival. In our experiments, we observed a maximum survival probability of approximately 80% even with close to 1000 MscL channels per cell. It is possible that the combined effort of the six other mechanosensitive channels would make up for some if not all of the remaining 20%. To explore the contribution of another channel to survival, van den Berg et al. also queried the contribution of MscS, another mechanosensitive channel, to survival in the absence of any other species of mechanosensitive channel. It was found that over the explored range of MscS channel copy numbers, the maximum survival rate was approximately 50%, suggesting that different mechanosensitive channels have an upper limit to how much protection they can confer. Both van den Berg et al. and our work show that there is still much to be learned with respect to the interplay between the various species of mechanosensitive channel as well as their regulation.

Recent work has shown that both magnitude and the rate of osmotic down shock are important factors in determining cell survival (Bialecka-Fornal et al., 2015). In this work, we show that this finding holds true for a single species of mechanosensitive channel, even at high levels of expression. One might naïvely expect that this rate-dependent effect would disappear once a certain threshold of channels had been met. Our experiments, however, show that even at nearly 1000 channels per cell the predicted survival curves for a slow (< 1.0 Hz) and fast (≥ 1.0 Hz) are shifted relative to each other with the fast shock predicting lower rates of survival. This suggests either we have not reached this threshold in our experiments or there is more to understand about the relationship between abundance, channel species, and the shock rate.

Some experimental and theoretical treatments suggest that only a few copies of MscL or MscS should be necessary for 100% protection given our knowledge of the conductance and the maximal water flux through the channel in its open state (Booth, 2014; Louhivuori et al., 2010). However, recent proteomic studies have revealed average MscL copy numbers to be in the range of several hundred per cell, depending on the condition, as can be seen in Table 1 (Li et al., 2014; Schmidt et

al., 2016; Soufi et al., 2015). Studies focusing solely on MscL have shown similar counts through quantitative Western blotting and fluorescence microscopy (Bialecka-Fornal et al., 2012). Electrophysiology studies have told another story with copy number estimates ranging between 4 and 100 channels per cell (Blount et al., 1999; Booth et al., 2005; Stokes et al., 2003). These measurements, however, measure the active number of channels. The factors regulating channel activity in these experiments could be due to perturbations during the sample preparation or reflect some unknown mechanism of regulation, such as the presence or absence of interacting cofactors (Schumann et al., 2010). The work described here, on the other hand, measures the *maximum* number of channels that could be active and may be able to explain why the channel abundance is higher than estimated by theoretical means. There remains much more to be learned about the regulation of activity in these systems. As the *in vivo* measurement of protein copy number becomes accessible through novel single-cell and single-molecule methods, we will continue to collect more facts about this fascinating system and hopefully connect the molecular details of mechanosensation with perhaps the most important physiological response – life or death.

Table 5.1: Measured cellular copy numbers of MscL.
Asterisk (*) Indicates inferred MscL channel copy number from the total number of detected MscL peptides.

Reported channels per cell	Method	Reference
480 ± 103	Western blotting	Bialecka-Fornal et al. (2012)
560*	Ribosomal profiling	Li et al. (2014)
331*	Mass spectrometry	Schmidt et al. (2016)
583*	Mass spectrometry	Soufi et al. (2015)
4 - 5	Electrophysiology	Stokes et al. (2003)
10 - 100	Electrophysiology	Booth et al. (2005)
10 - 15	Electrophysiology	Blount et al. (1999)

5.4 Materials & Methods

Bacterial strains and growth conditions

The bacterial strains are described in Table S1. The parent strain for the mutants used in this study was MJF641 (Edwards et al., 2012), a strain which had all seven mechanosensitive channels deleted. The MscL-sfGFP coding region from MLG910

(Bialecka-Fornal et al., 2012) was integrated into MJF641 by P1 transduction, creating the strain D6LG-Tn10. Selection pressure for MscL integration was created by incorporating an osmotic shock into the transduction protocol, which favored the survival of MscL-expressing stains relative to MJF641 by ~100-fold. Screening for integration candidates was based on fluorescence expression of plated colonies. Successful integration was verified by sequencing. Attempts to transduce RBS-modified MscL-sfGFP coding regions became increasingly inefficient as the targeted expression level of MscL was reduced. This was due to the decreasing fluorescence levels and survival rates of the integration candidates. Consequently, Shine-Dalgarno sequence modifications were made by inserting DNA oligos with lambda Red-mediated homologous recombination, i.e., recombineering (Sharan et al., 2009). The oligos had a designed mutation (Fig. fig. 5.2) flanked by ~25 base pairs that matched the targeted MscL region (Table S2). A two-step recombineering process of selection followed by counter selection using a *tetA-sacB* gene fusion cassette (Li et al., 2013) was chosen because of its capabilities to integrate with efficiencies comparable to P1 transduction and not leave antibiotic resistance markers or scar sequences in the final strain. To prepare the strain D6LG-Tn10 for this scheme, the Tn10 transposon containing the *tetA* gene needed to be removed to avoid interference with the *tetA-sacB* cassette. Tn10 was removed from the middle of the *ycjM* gene with the primer Tn10delR (Table S2) by recombineering, creating the strain D6LG (SD0). Counter selection against the *tetA* gene was promoted by using agar media with fusaric acid (Bochner et al., 1980; Li et al., 2013). The *tetA-sacB* cassette was PCR amplified out of the strain XTL298 using primers MscLSP-Sac and MscLSPSSacR (Table S2). The cassette was integrated in place of the spacer region in front of the MscL start codon of D6LG (SD0) by recombineering, creating the intermediate strain D6LTetSac. Positive selection for cassette integration was provided by agar media with tetracycline. Finally, the RBS modifying oligos were integrated into place by replacing the *tetA-sacB* cassette by recombineering. Counter selection against both *tetA* and *sacB* was ensured by using agar media with fusaric acid and sucrose (Li et al., 2013), creating the Shine-Dalgarno mutant strains used in this work.

Strain cultures were grown in 5 mL of LB-Lennox media with antibiotic (apramycin) overnight at 37°C. The next day, 50 µL of overnight culture was inoculated into 5 mL of LB-Lenox with antibiotic and the culture was grown to OD_{600nm} ~0.25. Subsequently, 500 µL of that culture was inoculated into 5 mL of LB-Lennox supplemented with 500mM of NaCl and the culture was regrown to OD_{600nm} ~0.25.

A 1 mL aliquot was taken and used to load the flow cell.

Flow cell

All experiments were conducted in a home-made flow cell as is shown in Fig. fig. 5.3(A). This flow cell has two inlets which allow media of different osmolarity to be exchanged over the course of the experiment. The imaging region is approximately 10 mm wide and 100 μm in depth. All imaging took place within 1 – 2 cm of the outlet to avoid imaging cells within a non-uniform gradient of osmolarity. The interior of the flow cell was functionalized with a 1:400 dilution of polyethylenimine prior to addition of cells with the excess washed away with water. A dilute cell suspension in LB Lennox with 500 mM NaCl was loaded into one inlet while the other was connected to a vial of LB medium with no NaCl. This hypotonic medium was clamped during the loading of the cells.

Once the cells had adhered to the polyethylenimine coated surface, the excess cells were washed away with the 500 mM NaCl growth medium followed by a small (~20 μL) air bubble. This air bubble forced the cells to lay flat against the imaging surface, improving the time-lapse imaging. Over the observation period, cells not exposed to an osmotic shock were able to grow for 4 – 6 divisions, showing that the flow cell does not directly impede cell growth.

Imaging conditions

All imaging was performed in a flow cell held at 30°C on a Nikon Ti-Eclipse microscope outfitted with a Perfect Focus system enclosed in a Haison environmental chamber (approximately 1°C regulation efficiency). The microscope was equipped with a 488 nm laser excitation source (CrystaLaser) and a 520/35 laser optimized filter set (Semrock). The images were collected on an Andor iXon EM+ 897 EM-CCD camera and all microscope and acquisition operations were controlled via the open source μ Manager microscope control software (Edelstein et al., 2014). Once cells were securely mounted onto the surface of the glass coverslip, between 15 and 20 positions containing 5 to 10 cells were marked and the coordinates recorded. At each position, a phase contrast and GFP fluorescence image was acquired for segmentation and subsequent measurement of channel copy number. To perform the osmotic shock, LB media containing no NaCl was pulled into the flow cell through a syringe pump. To monitor the media exchange, both the high salt and no salt LB media were supplemented with a low-affinity version of the calcium-sensitive dye Rhod-2 (250 nM; TEF Labs) which fluoresces when bound to Ca^{2+} . The no

salt medium was also supplemented with $1\mu\text{M}$ CaCl_2 to make the media mildly fluorescent and the exchange rate was calculated by measuring the fluorescence increase across an illuminated section of one of the positions. These images were collected in real time for the duration of the shock. The difference in measured fluorescence between the pre-shock images and those at the end of the shock set the scale of a 500 mM NaCl down shock. The rate was calculated by fitting a line to the middle region of this trace. Further details regarding this procedure can be found in Bialecka-Fornal et al. (2015).

Image Processing

Images were processed using a combination of automated and manual methods. First, expression of MscL was measured via segmenting individual cells or small clusters of cells in phase contrast and computing the mean pixel value of the fluorescence image for each segmented object. The fluorescence images were passed through several filtering operations which reduced high-frequency noise as well as corrected for uneven illumination of the excitation wavelength.

Survival or death classification was performed manually using the CellProfiler plugin for ImageJ software (NIH). A survivor was defined as a cell which was able to undergo at least two division events after the osmotic down shock. Cell death was recognized by stark changes in cell morphology including loss of phase contrast through ejection of cytoplasmic material, structural decomposition of the cell wall and membrane, and the inability to divide. To confirm that these morphological cues corresponded with cell death, we probed cell viability on a subset of our strains after osmotic shock through staining with propidium iodide, a DNA intercalating dye commonly used to identifying dead cells (LIVE/DEAD BacLight Bacterial Cell Viability Assay, Thermo Fisher). We found that our classification based on morphology agreed with that based off of staining within 1%. More information regarding these experiments can be found in the Supplement C. Cells which detached from the surface during the post-shock growth phase or those which became indistinguishable from other cells due to clustering were not counted as survival or death and were removed from the dataset completely. A region of the cell was manually marked with 1.0 (survival) or 0.0 (death) by clicking on the image. The xy coordinates of the click as well as the assigned value were saved as an .xml file for that position.

The connection between the segmented cells and their corresponding manual mark-

ers was automated. As the manual markings were made on the first phase contrast image after the osmotic shock, small shifts in the positions of the cell made one-to-one mapping with the segmentation mask non-trivial. The linkages between segmented cell and manual marker were made by computing all pairwise distances between the manual marker and the segmented cell centroid, taking the shortest distance as the true pairing. The linkages were then inspected manually and incorrect mappings were corrected as necessary.

All relevant statistics about the segmented objects as well as the sample identity, date of acquisition, osmotic shock rate, and camera exposure time were saved as .csv files for each individual experiment. A more in-depth description of the segmentation procedure as well as the relevant code can be accessed as a Jupyter Notebook at (http://rpgroup.caltech.edu/mscl_survival).

Calculation of effective channel copy number

To compute the MscL channel copy number, we relied on measuring the fluorescence level of a bacterial strain in which the mean MscL channel copy number was known via fluorescence microscopy (Bialecka-Fornal et al., 2012). *E. coli* strain MLG910, which expresses the MscL-sfGFP fusion protein from the wild-type SD sequence, was grown under identical conditions to those described in Bialecka-Fornal et al. 2015 in LB Miller medium (BD Medical Sciences) to an OD_{600nm} of ~0.3. The cells were then diluted ten fold and immobilized on a rigid 2% agarose substrate and placed onto a glass bottom petri dish and imaged in the same conditions as described previously.

Images were taken of six biological replicates of MLG910 and were processed identically to those in the osmotic shock experiments. A calibration factor between the average cell fluorescence level and mean MscL copy number was then computed. We assumed that all measured fluorescence (after filtering and background subtraction) was derived from the MscL-sfGFP fusion,

$$\langle I_{\text{tot}} \rangle = \alpha \langle N \rangle, \quad (5.3)$$

in which α is the calibration factor and $\langle N \rangle$ is the mean cellular MscL-sfGFP copy number as reported in Bialecka-Fornal et al. 2012 (Bialecka-Fornal et al., 2012). To correct for errors in segmentation, the intensity was computed as an areal density $\langle I_A \rangle$ and was multiplied by the average cell area $\langle A \rangle$ of the population. The

calibration factor was therefore computed as

$$\alpha = \frac{\langle I_A \rangle \langle A \rangle}{\langle N \rangle}. \quad (5.4)$$

We used Bayesian inferential methods to compute this calibration factor taking measurement error and replicate-to-replicate variation into account. The resulting average cell area and calibration factor was used to convert the measured cell intensities from the osmotic shock experiments to cell copy number. The details of this inference are described in depth in the supplemental information (*Standard Candle Calibration*).

Logistic regression

We used Bayesian inferential methods to find the most probable values of the coefficients β_0 and β_1 and the appropriate credible regions and is described in detail in the supplemental information (*Logistic Regression*). Briefly, we used Markov chain Monte Carlo (MCMC) to sample from the log posterior distribution and took the most probable value as the mean of the samples for each parameter. The MCMC was performed using the Stan probabilistic programming language (Carpenter et al., 2017) and all models can be found on the GitHub repository (http://github.com/rpgroup-pboc/mscl_survival).

Calculation of survival probability error

The vertical error bars for the points shown in Fig. fig. 5.5 represent our uncertainty in the survival probability given our measurement of n survivors out of a total N single-cell measurements. The probability distribution of the survival probability p_s given these measurements can be written using Bayes' theorem as

$$g(p_s | n, N) = \frac{f(n | p_s, N)g(p_s)}{f(n | N)}, \quad (5.5)$$

where g and f represent probability density functions over parameters and data, respectively. The likelihood $f(n | p_s, N)$ represents the probability of measuring n survival events, given a total of N measurements each with a probability of survival p_s . This matches the story for the Binomial distribution and can be written as

$$f(n | p_s, N) = \frac{N!}{n!(N-n)!} p_s^n (1 - p_s)^{N-n}. \quad (5.6)$$

To maintain maximal ignorance we can assume that any value for p_s is valid, such that is in the range $[0, 1]$. This prior knowledge, represented by $g(p_s)$, can be written as

$$g(p_s) = \begin{cases} 1 & 0 \leq p_s \leq 1 \\ 0 & \text{otherwise} \end{cases}. \quad (5.7)$$

We can also assume maximal ignorance for the total number of survival events we could measure given N observations, $f(n | N)$. Assuming all observations are equally likely, this can be written as

$$f(n | N) = \frac{1}{N+1} \quad (5.8)$$

where the addition of one comes from the possibility of observing zero survival events. Combining Eq. eq. 5.6; eq. 5.7; and eq. 5.8, the posterior distribution $g(p_s | n, N)$ is

$$g(p_s | n, N) = \frac{(N+1)!}{n!(N-n)!} p_s^n (1-p_s)^{N-n}. \quad (5.9)$$

The most probable value of p_s , where the posterior probability distribution given by Eq. eq. 5.9 is maximized, can be found by computing the point at which derivative of the log posterior with respect to p_s goes to zero,

$$\frac{d \log g(p_s | n, N)}{dp_s} = \frac{n}{p_s} - \frac{N-n}{1-p_s} = 0. \quad (5.10)$$

Solving Eq. eq. 5.10 for p_s gives the most likely value for the probability,

$$p_s^* = \frac{n}{N}. \quad (5.11)$$

So long as $N \gg np_s^*$, Eq. eq. 5.9 can be approximated as a Gaussian distribution with a mean p_s^* and a variance $\sigma_{p_s}^2$. By definition, the variance of a Gaussian distribution is computed as the negative reciprocal of the second derivative of the log posterior evaluated at $p_s = p_s^*$,

$$\sigma_{p_s}^2 = - \left(\frac{d^2 \log g(p_s | n, N)}{dp_s^2} \Bigg|_{p_s=p_s^*} \right)^{-1}. \quad (5.12)$$

Evaluating Eq. eq. 5.12 yields

$$\sigma_{p_s}^2 = \frac{n(N-n)}{N^3}. \quad (5.13)$$

Given Eq. eq. 5.11 and Eq. eq. 5.13, the most-likely survival probability and estimate of the uncertainty can be expressed as

$$p_s = p_s^* \pm \sigma_{p_s}. \quad (5.14)$$

Data and software availability

All raw image data is freely available and is stored on the CaltechDATA Research Data Repository (Chure et al., 2018a). The raw Markov chain Monte Carlo samples are stored as .csv files on CaltechDATA (Chure et al., 2018b). All processed experimental data, Python, and Stan code used in this work are freely available through our GitHub repository (http://github.com/rpgroup-pboc/mscl_survival) (Chure et al., 2018c) accessible through DOI: 10.5281/zenodo.1252524. The scientific community is invited to fork our repository and open constructive issues.

5.5 Acknowledgements

We thank Nathan Belliveau, Maja Bialecka-Fornal, Justin Bois, Soichi Hirokawa, Jaspar Landman, Manuel Razo-Mejia, Muir Morrison, and Shyam Saladi for useful advice and discussion. We thank Don Court for strain XTL298 and Samantha Miller for strain MJF641. This work was supported by the National Institutes of Health DP1 OD000217 (Director's Pioneer Award), R01 GM085286, GM084211-A1, GM118043-01, and La Fondation Pierre Gilles de Gennes. ## References # Supplemental Information For Chapter 2: Signal Processing Via Allosteric Transcription Factors {#sec:ch2_si} A version of this chapter originally appeared as Razo-Mejia, M.* , Barnes, S.L.* , Belliveau, N.M.* , Chure, G.* , Einav, T.* , Lewis, M., and Phillips, R. (2018). Tuning Transcriptional Regulation through Signaling: A Predictive Theory of Allosteric Induction. *Cell Systems* 6, 456-469.e10. (* contributed equally). M.R.M, S.L.B, N.M.B, G.C., and T.E. contributed equally to this work from the theoretical underpinnings to the experimental design and execution. M.R.M, S.L.B, N.M.B, G.C, T.E., and R.P. wrote the paper. M.L. provided extensive guidance and advice. ## Inferring Allosteric Parameters from Previous Data {#sec:ch2_si_epAI}

The fold-change profile described by features three unknown parameters K_A , K_I , and $\Delta\varepsilon_{AI}$. In this section, we explore different conceptual approaches to determining these parameters. We first discuss how the induction titration profile of the simple repression constructs used in this paper are not sufficient to determine all three MWC parameters simultaneously, since multiple degenerate sets of parameters can produce the same fold-change response. We then utilize an additional data set from Brewster et al. (2014) to determine the parameter $\Delta\varepsilon_{AI} = 4.5 k_B T$, after which the remaining parameters K_A and K_I can be extracted from any induction profile with no further degeneracy.

Degenerate Parameter Values

In this section, we discuss how multiple sets of parameters may yield identical fold-change profiles. More precisely, we shall show that if we try to fit the data in to the fold-change and extract the three unknown parameters (K_A , K_I , and $\Delta\varepsilon_{AI}$), then multiple degenerate parameter sets would yield equally good fits. In other words, this data set alone is insufficient to uniquely determine the actual physical parameter values of the system. This problem persists even when fitting multiple data sets simultaneously as in Section “”.

In , we fit the $R = 260$ data by fixing $\Delta\varepsilon_{AI}$ to the value shown on the x -axis and determine the parameters K_A and K_I given this constraint. We use the fold-change function but with $\beta\Delta\varepsilon_{RA}$ modified to the form $\beta\Delta\varepsilon_{RA}$ in to account for the underlying assumptions used when fitting previous data (see Section “” for a full explanation of why this modification is needed).

The best-fit curves for several different values of $\Delta\varepsilon_{AI}$ are shown in . Note that these fold-change curves are nearly overlapping, demonstrating that different sets of parameters can yield nearly equivalent responses. Without more data, the relationships between the parameter values shown in represent the maximum information about the parameter values that can be extracted from the data. Additional experiments which independently measure any of these unknown parameters could resolve this degeneracy. For example, NMR measurements could be used to directly measure the fraction $(1 + e^{-\beta\Delta\varepsilon_{AI}})^{-1}$ of active repressors in the absence of IPTG (??; Gardino et al., 2003).

Computing $\Delta\varepsilon_{AI}$

As shown in the previous section, the fold-change response of a single strain is not sufficient to determine the three MWC parameters (K_A , K_I , and $\Delta\varepsilon_{AI}$), since

degenerate sets of parameters yield nearly identical fold-change responses. To circumvent this degeneracy, we now turn to some previous data from the *lac* system in order to determine the value of $\Delta\epsilon_{AI}$ in for the induction of the Lac repressor. Specifically, we consider two previous sets of work from: (1) Garcia and Phillips (2011) and (2) Brewster et al. (2014), both of which measured fold-change with the same simple repression system in the absence of inducer ($c = 0$) but at various repressor copy numbers R . The original analysis for both data sets assumed that in the absence of inducer all of the Lac repressors were in the active state. As a result, the effective binding energies they extracted were a convolution of the DNA binding energy $\Delta\epsilon_{RA}$ and the allosteric energy difference $\Delta\epsilon_{AI}$ between the Lac repressor's active and inactive states. We refer to this convoluted energy value as $\tilde{\Delta\epsilon}_{RA}$. We first disentangle the relationship between these parameters in Garcia and Phillips and then use this relationship to extract the value of $\Delta\epsilon_{AI}$ from Brewster et al. (2014).

Garcia and Phillips determined the total repressor copy numbers R of different strains using quantitative Western blots. Then they measured the fold-change at these repressor copy numbers for simple repression constructs carrying the O1, O2, O3, and Oid *lac* operators integrated into the chromosome. These data were then fit to the following thermodynamic model to determine the repressor-DNA binding energies $\tilde{\Delta\epsilon}_{RA}$ for each operator,

$$\text{fold-change}(c = 0) = \left(1 + \frac{R}{N_{NS}} e^{-\beta\tilde{\Delta\epsilon}_{RA}}\right)^{-1}. \quad (5.15)$$

Note that this functional form does not exactly match our fold-change in the limit $c = 0$,

$$\text{fold-change}(c = 0) = \left(1 + \frac{1}{1 + e^{-\beta\Delta\epsilon_{AI}}} \frac{R}{N_{NS}} e^{-\beta\Delta\epsilon_{RA}}\right)^{-1}, \quad (5.16)$$

since it is missing the factor $\frac{1}{1 + e^{-\beta\Delta\epsilon_{AI}}}$ which specifies what fraction of repressors are in the active state in the absence of inducer,

$$\frac{1}{1 + e^{-\beta\Delta\epsilon_{AI}}} = p_A(0). \quad (5.17)$$

In other words, Garcia and Phillips assumed that in the absence of inducer, all repressors were active. In terms of our notation, the convoluted energy values

$\Delta\tilde{\varepsilon}_{RA}$ extracted by Garcia and Phillips (namely, $\Delta\tilde{\varepsilon}_{RA} = -15.3 k_B T$ for O1 and $\Delta\tilde{\varepsilon}_{RA} = -17.0 k_B T$ for Oid) represent

$$\beta\Delta\tilde{\varepsilon}_{RA} = \beta\Delta\varepsilon_{RA} - \log\left(\frac{1}{1 + e^{-\beta\Delta\varepsilon_{AI}}}\right). \quad (5.18)$$

Note that if $e^{-\beta\Delta\varepsilon_{AI}} \ll 1$, then nearly all of the repressors are active in the absence of inducer so that $\Delta\tilde{\varepsilon}_{RA} \approx \Delta\varepsilon_{RA}$. In simple repression systems where we definitively know the value of $\Delta\varepsilon_{RA}$ and R , we can use to determine the value of $\Delta\varepsilon_{AI}$ by comparing with experimentally determined fold-change values. However, the binding energy values that we use from Garcia and Phillips (2011) are effective parameters $\Delta\tilde{\varepsilon}_{RA}$. In this case, we are faced with an undetermined system in which we have more variables than equations, and we are thus unable to determine the value of $\Delta\varepsilon_{AI}$. In order to obtain this parameter, we must turn to a more complex regulatory scenario which provides additional constraints that allow us to fit for $\Delta\varepsilon_{AI}$.

A variation on simple repression in which multiple copies of the promoter are available for repressor binding (for instance, when the simple repression construct is on plasmid) can be used to circumvent the problems that arise when using $\Delta\tilde{\varepsilon}_{RA}$. This is because the behavior of the system is distinctly different when the number of active repressors $p_A(0)R$ is less than or greater than the number of available promoters N . Repression data for plasmids with known copy number N allows us to perform a fit for the value of $\Delta\varepsilon_{AI}$.

To obtain an expression for a system with multiple promoters N , we follow Weinert et al. (2014), writing the fold-change in terms of the the grand canonical ensemble as

$$\text{fold-change} = \frac{1}{1 + \lambda_r e^{-\beta\Delta\varepsilon_{RA}}}, \quad (5.19)$$

where $\lambda_r = e^{\beta\mu}$ is the fugacity and μ is the chemical potential of the repressor. The fugacity will enable us to easily enumerate the possible states available to the repressor.

To determine the value of λ_r , we first consider that the total number of repressors

in the system, R_{tot} , is fixed and given by

$$R_{\text{tot}} = R_S + R_{NS}, \quad (5.20)$$

where R_S represents the number of repressors specifically bound to the promoter and R_{NS} represents the number of repressors nonspecifically bound throughout the genome. The value of R_S is given by

$$R_S = N \frac{\lambda_r e^{-\beta \Delta \varepsilon_{RA}}}{1 + \lambda_r e^{-\beta \Delta \varepsilon_{RA}}}, \quad (5.21)$$

where N is the number of available promoters in the cell. Note that in counting N , we do not distinguish between promoters that are on plasmid or chromosomally integrated provided that they both have the same repressor-operator binding energy (Weinert et al. 2014). The value of R_{NS} is similarly give by

$$R_{NS} = N_{NS} \frac{\lambda_r}{1 + \lambda_r}, \quad (5.22)$$

where N_{NS} is the number of non-specific sites in the cell (recall that we use $N_{NS} = 4.6 \times 10^6$ for *E. coli*).

Substituting in into the modified yields the form

$$p_A(0)R_{\text{tot}} = \frac{1}{1 + e^{-\beta \Delta \varepsilon_{AI}}} \left(N \frac{\lambda_r e^{-\beta \Delta \varepsilon_{RA}}}{1 + \lambda_r e^{-\beta \Delta \varepsilon_{RA}}} + N_{NS} \frac{\lambda_r}{1 + \lambda_r} \right), \quad (5.23)$$

where we recall from that $\beta \Delta \varepsilon_{RA} = \beta \Delta \tilde{\varepsilon}_{RA} + \log \left(\frac{1}{1 + e^{-\beta \Delta \varepsilon_{AI}}} \right)$. Numerically solving for λ_r and plugging the value back into yields a fold-change function in which the only unknown parameter is $\Delta \varepsilon_{AI}$.

With these calculations in hand, we can now determine the value of the $\Delta \varepsilon_{AI}$ parameter. shows how different values of $\Delta \varepsilon_{AI}$ lead to significantly different fold-change response curves. Thus, analyzing the specific fold-change response of any strain with a known plasmid copy number N will fix $\Delta \varepsilon_{AI}$. Interestingly, the inflection point of occurs near $p_A(0)R_{\text{tot}} = N$ (as shown by the triangles in), so that merely knowing where the fold-change response transitions from concave down to concave up is sufficient to obtain a rough value for $\Delta \varepsilon_{AI}$. We note, however, that for $\Delta \varepsilon_{AI} \geq 5 k_B T$, increasing $\Delta \varepsilon_{AI}$ further does not affect the fold-change because

essentially every repressors will be in the active state in this regime. Thus, if the $\Delta\varepsilon_{AI}$ is in this regime, we can only bound it from below.

We now analyze experimental induction data for different strains with known plasmid copy numbers to determine $\Delta\varepsilon_{AI}$. shows experimental measurements of fold-change for two O1 promoters with $N = 64$ and $N = 52$ copy numbers and one Oid promoter with $N = 10$ from Brewster et al. (2014). By fitting these data to , we extracted the parameter value $\Delta\varepsilon_{AI} = 4.5 k_B T$. Substituting this value into shows that 99% of the repressors are in the active state in the absence of inducer and $\Delta\tilde{\varepsilon}_{RA} \approx \Delta\varepsilon_{RA}$, so that all of the previous energies and calculations made by Garcia and Phillips (2011) and Brewster et al. (2014) were accurate.

REFERENCES

- Ackers, G.K., and Johnson, A.D. (1982). Quantitative model for gene regulation by A phage repressor. *Proc. Natl. Acad. Sci. USA* 5.
- Anderson, R.P., Jin, R., and Grunkemeier, G.L. (2003). Understanding logistic regression analysis in clinical reports: An introduction. *The Annals of Thoracic Surgery* 75, 753–757.
- Barnes, S.L., Belliveau, N.M., Ireland, W.T., Kinney, J.B., and Phillips, R. (2019). Mapping DNA sequence to transcription factor binding energy in vivo. *PLOS Computational Biology* 15, e1006226.
- Bavi, N., Cortes, D.M., Cox, C.D., Rohde, P.R., Liu, W., Deitmer, J.W., Bavi, O., Strop, P., Hill, A.P., Rees, D., et al. (2016). The role of MscL amphipathic N terminus indicates a blueprint for bilayer-mediated gating of mechanosensitive channels. *Nature Communications* 7, 11984.
- Berg, H.C., and Purcell, E.M. (1977). Physics of chemoreception. *Biophysical Journal* 20, 193–219.
- Bialecka-Fornal, M., Lee, H.J., DeBerg, H.A., Gandhi, C.S., and Phillips, R. (2012). Single-Cell Census of Mechanosensitive Channels in Living Bacteria. *PLoS ONE* 7, e33077.
- Bialecka-Fornal, M., Lee, H.J., and Phillips, R. (2015). The Rate of Osmotic Down-shock Determines the Survival Probability of Bacterial Mechanosensitive Channel Mutants. *Journal of Bacteriology* 197, 231–237.
- Bintu, L., Buchler, N.E., Garcia, H.G., Gerland, U., Hwa, T., Kondev, J., Kuhlman, T., and Phillips, R. (2005a). Transcriptional regulation by the numbers: Applications. *Current Opinion in Genetics & Development* 15, 125–135.
- Bintu, L., Buchler, N.E., Garcia, H.G., Gerland, U., Hwa, T., Kondev, J., and Phillips, R. (2005b). Transcriptional regulation by the numbers: Models. *Current Opinion in Genetics & Development* 15, 116–124.
- Blount, P., Sukharev, S.I., Moe, P.C., Martinac, B., and Kung, C. (1999). Mechanosensitive channels of bacteria. *Methods in Enzymology* 294, 458–482.
- Bochner, B.R., Huang, H.-C., Schieven, G.L., and Ames, B.N. (1980). Positive selection for loss of tetracycline resistance. *Journal of Bacteriology* 143, 926–933.

- Boedicker, J.Q., Garcia, H.G., Johnson, S., and Phillips, R. (2013a). DNA sequence-dependent mechanics and protein-assisted bending in repressor-mediated loop formation. *Physical Biology* *10*, 066005.
- Boedicker, J.Q., Garcia, H.G., and Phillips, R. (2013b). Theoretical and Experimental Dissection of DNA Loop-Mediated Repression. *Physical Review Letters* *110*, 018101.
- Booth, I.R. (2014). Bacterial mechanosensitive channels: Progress towards an understanding of their roles in cell physiology. *Current Opinion in Microbiology* *18*, 16–22.
- Booth, I.R., Edwards, M.D., Murray, E., and Miller, S. (2005). The role of bacterial ion channels in cell physiology. In *Bacterial Ion Channels and Their Eukaryotic Homologs*, A. Kubalsi, and B. Martinac, eds. (Washington DC: American Society for Microbiology), pp. 291–312.
- Brewster, R.C., Jones, D.L., and Phillips, R. (2012). Tuning Promoter Strength through RNA Polymerase Binding Site Design in *Escherichia coli*. *PLoS Computational Biology* *8*, e1002811.
- Brewster, R.C., Weinert, F.M., Garcia, H.G., Song, D., Rydenfelt, M., and Phillips, R. (2014). The Transcription Factor Titration Effect Dictates Level of Gene Expression. *Cell* *156*, 1312–1323.
- Brophy, J.A.N., and Voigt, C.A. (2014). Principles of genetic circuit design. *Nature Methods* *11*, 508–520.
- Buchler, N.E., Gerland, U., and Hwa, T. (2003). On schemes of combinatorial transcription logic. *Proceedings of the National Academy of Sciences* *100*, 5136–5141.
- Carpenter, B., Gelman, A., Hoffman, M.D., Lee, D., Goodrich, B., Betancourt, M., Brubaker, M., Guo, J., Li, P., and Riddell, A. (2017). Stan: A Probabilistic Programming Language. *Journal of Statistical Software* *76*, 1–32.
- Chure, G., Lee, H.J., and Phillips, R. (2018a). Image data for "Connecting the Dots between Mechanosensitive Channel Abundance, Osmotic Shock, and Survival at Single-Cell Resolution" accessible through DOI: 10.22002/D1.941.
- Chure, G., Lee, H.J., and Phillips, R. (2018b). MCMC chains generated in "Connecting the Dots between Mechanosensitive Channel Abundance, Osmotic Shock, and Survival at Single-Cell Resolution" accessible through DOI 10.22002/D1.942.

- Chure, G., Lee, H.J., and Phillips, R. (2018c). Github repository for "Connecting the Dots between Mechanosensitive Channel Abundance, Osmotic Shock, and Survival at Single-Cell Resolution" accessible through DOI: 10.5281/Zenodo.1252524.
- Chure, G., Razo-Mejia, M., Belliveau, N.M., Einav, T., Kaczmarek, Z.A., Barnes, S.L., and Phillips, R. (2019). Predictive Shifts in Free Energy Couple Mutations to Their Phenotypic Consequences. *Proceedings of the National Academy of Sciences* *116*.
- Colin, R., and Sourjik, V. (2017). Emergent properties of bacterial chemotaxis pathway. *Current Opinion in Microbiology* *39*, 24–33.
- Cruickshank, C.C., Minchin, R.F., Le Dain, A.C., and Martinac, B. (1997). Estimation of the pore size of the large-conductance mechanosensitive ion channel of *Escherichia Coli*. *Biophysical Journal* *73*, 1925–1931.
- Daber, R., Sharp, K., and Lewis, M. (2009). One Is Not Enough. *Journal of Molecular Biology* *392*, 1133–1144.
- Daber, R., Sochor, M.A., and Lewis, M. (2011). Thermodynamic Analysis of Mutant lac Repressors. *Journal of Molecular Biology* *409*, 76–87.
- Edelstein, A.D., Tsuchida, M.A., Amodaj, N., Pinkard, H., Vale, R.D., and Stuurman, N. (2014). Advanced methods of microscope control using μ Manager software. *Journal of Biological Methods* *1*, 10.
- Edwards, M.D., Black, S., Rasmussen, T., Rasmussen, A., Stokes, N.R., Stephen, T.L., Miller, S., and Booth, I.R. (2012). Characterization of three novel mechanosensitive channel activities in *Escherichia Coli*. *Channels (Austin)* *6*, 272–281.
- Elowitz, M.B., Levine, A.J., Siggia, E.D., and Swain, P.S. (2002). Stochastic gene expression in a single cell. *Science* *297*, 1183–1186.
- Espah Borujeni, A., Channarasappa, A.S., and Salis, H.M. (2014). Translation rate is controlled by coupled trade-offs between site accessibility, selective RNA unfolding and sliding at upstream standby sites. *Nucleic Acids Research* *42*, 2646–2659.
- Feeling-Taylor, A.R., Yau, S.-T., Petsev, D.N., Nagel, R.L., Hirsch, R.E., and Vekilov, P.G. (2004). Crystallization Mechanisms of Hemoglobin C in the R State. *Biophysical Journal* *87*, 2621–2629.
- Fernández-Castané, A., Vine, C.E., Caminal, G., and López-Santín, J. (2012). Evidencing the role of lactose permease in IPTG uptake by *Escherichia coli* in fed-

- batch high cell density cultures. *Journal of Biotechnology* 157, 391–398.
- Finch, J.T., Perutz, M.F., Bertles, J.F., and Dobler, J. (1973). Structure of Sickled Erythrocytes and of Sickle-Cell Hemoglobin Fibers. *Proceedings of the National Academy of Sciences* 70, 718–722.
- Frumkin, I., Lajoie, M.J., Gregg, C.J., Hornung, G., Church, G.M., and Pilpel, Y. (2018). Codon usage of highly expressed genes affects proteome-wide translation efficiency. *Proceedings of the National Academy of Sciences* 115, E4940–E4949.
- Gama-Castro, S., Salgado, H., Santos-Zavaleta, A., Ledezma-Tejeida, D., Muñiz-Rascado, L., García-Sotelo, J.S., Alquicira-Hernández, K., Martínez-Flores, I., Panner, L., Castro-Mondragón, J.A., et al. (2016). RegulonDB version 9.0: High-level integration of gene regulation, coexpression, motif clustering and beyond. *Nucleic Acids Research* 44, D133–D143.
- Garcia, H.G., and Phillips, R. (2011). Quantitative dissection of the simple repression input-output function. *Proceedings of the National Academy of Sciences* 108, 12173–12178.
- Garcia, H.G., Lee, H.J., Boedicker, J.Q., and Phillips, R. (2011). Comparison and Calibration of Different Reporters for Quantitative Analysis of Gene Expression. *Biophysical Journal* 101, 535–544.
- Garcia, H.G., Sanchez, A., Boedicker, J.Q., Osborne, M., Gelles, J., Kondev, J., and Phillips, R. (2012). Operator Sequence Alters Gene Expression Independently of Transcription Factor Occupancy in Bacteria. *Cell Reports* 2, 150–161.
- Gardino, A.K., Volkman, B.F., Cho, H.S., Lee, S.-Y., Wemmer, D.E., and Kern, D. (2003). The NMR Solution Structure of BeF₃-Activated SpoOF Reveals the Conformational Switch in a Phosphorelay System. *Journal of Molecular Biology* 331, 245–254.
- Harman, J.G. (2001). Allosteric regulation of the cAMP receptor protein. *Biochimica et Biophysica Acta (BBA) - Protein Structure and Molecular Enzymology* 1547, 1–17.
- Hase, C.C., Minchin, R.F., Kloda, A., and Martinac, B. (1997). Cross-linking studies and membrane localization and assembly of radiolabelled large mechanosensitive ion channel (MscL) of *Escherichia Coli*. *Biochem Biophys Res Commun* 232, 777–782.

- Haswell, E.S., Phillips, R., and Rees, D.C. (2011). Mechanosensitive Channels: What Can They Do and How Do They Do It? *Structure* *19*, 1356–1369.
- Herbig, U., Jobling, W.A., Chen, B.P.C., Chen, D.J., and Sedivy, J.M. (2004). Telomere Shortening Triggers Senescence of Human Cells through a Pathway Involving ATM, p53, and p21CIP1, but Not p16INK4a. *Molecular Cell* *14*, 501–513.
- Hui, S., Silverman, J.M., Chen, S.S., Erickson, D.W., Basan, M., Wang, J., Hwa, T., and Williamson, J.R. (2015). Quantitative proteomic analysis reveals a simple strategy of global resource allocation in bacteria. *Molecular Systems Biology* *11*.
- Jones, D.L., Brewster, R.C., and Phillips, R. (2014). Promoter architecture dictates cell-to-cell variability in gene expression. *Science* *346*, 1533–1536.
- Jun, S., Si, F., Pugatch, R., and Scott, M. (2018). Fundamental principles in bacterial physiologyHistory, recent progress, and the future with focus on cell size control: A review. *Reports on Progress in Physics* *81*, 056601.
- Kepler, T.B., and Elston, T.C. (2001). Stochasticity in Transcriptional Regulation: Origins, Consequences, and Mathematical Representations. *Biophysical Journal* *81*, 3116–3136.
- Klumpp, S., and Hwa, T. (2008). Growth-rate-dependent partitioning of RNA polymerases in bacteria. *Proceedings of the National Academy of Sciences* *105*, 20245–20250.
- Klumpp, S., and Hwa, T. (2014). Bacterial growth: Global effects on gene expression, growth feedback and proteome partition. *Current Opinion in Biotechnology* *28*, 96–102.
- Ko, M.S.H. (1991). A stochastic model for gene induction. *Journal of Theoretical Biology* *153*, 181–194.
- Krembel, A., Colin, R., and Sourjik, V. (2015a). Importance of Multiple Methylation Sites in *Escherichia Coli* Chemotaxis. *PLoS ONE* *10*.
- Krembel, A.K., Neumann, S., and Sourjik, V. (2015b). Universal Response-Adaptation Relation in Bacterial Chemotaxis. *Journal of Bacteriology* *197*, 307–313.
- Kuhlman, T., Zhang, Z., Saier, M.H., and Hwa, T. (2007). Combinatorial transcriptional control of the lactose operon of *Escherichia coli*. *Proceedings of the National Academy of Sciences* *104*, 6043–6048.

- Lanfranco, M.F., Gárate, F., Engdahl, A.J., and Maillard, R.A. (2017). Asymmetric configurations in a reengineered homodimer reveal multiple subunit communication pathways in protein allostery. *Journal of Biological Chemistry* 292, 6086–6093.
- Levina, N., Totemeyer, S., Stokes, N.R., Louis, P., Jones, M.A., and Booth, I.R. (1999). Protection of *Escherichia Coli* cells against extreme turgor by activation of MscS and Mscl mechanosensitive channels: Identification of genes required for MscS activity. *EMBO J* 18, 1730–1737.
- Lewis, M., Chang, G., Horton, N.C., Kercher, M.A., Pace, H.C., Schumacher, M.A., Brennan, R.G., and Lu, P. (1996). Crystal Structure of the Lactose Operon Repressor and Its Complexes with DNA and Inducer. *Science* 271, 1247–1254.
- Li, G.-W., Burkhardt, D., Gross, C., and Weissman, J.S. (2014). Quantifying Absolute Protein Synthesis Rates Reveals Principles Underlying Allocation of Cellular Resources. *Cell* 157, 624–635.
- Li, X.-t., Thomason, L.C., Sawitzke, J.A., Costantino, N., and Court, D.L. (2013). Positive and negative selection using the tetA-sacB cassette: Recombineering and P1 transduction in *Escherichia Coli*. *Nucleic Acids Research* 41, e204–e204.
- Lindsley, J.E., and Rutter, J. (2006). Whence cometh the allosterome? *Proceedings of the National Academy of Sciences* 103, 10533–10535.
- Liu, F., Morrison, A.H., and Gregor, T. (2013). Dynamic interpretation of maternal inputs by the *Drosophila* segmentation gene network. *Proceedings of the National Academy of Sciences of the United States of America* 110, 6724–6729.
- Louhivuori, M., Risselada, H.J., van der Giessen, E., and Marrink, S.J. (2010). Release of content through mechano-sensitive gates in pressurized liposomes. *Proc Natl Acad Sci U S A* 107, 19856–19860.
- Lovely, G.A., Brewster, R.C., Schatz, D.G., Baltimore, D., and Phillips, R. (2015). Single-molecule analysis of RAG-Mediated V(D)J DNA cleavage. *Proceedings of the National Academy of Sciences* 112, E1715–E1723.
- Lutz, R., and Bujard, H. (1997). Independent and Tight Regulation of Transcriptional Units in *Escherichia Coli* Via the LacR/O, the TetR/O and AraC/I1-I2 Regulatory Elements. *Nucleic Acids Research* 25, 1203–1210.
- Martinac, B., Buechner, M., Delcour, A.H., Adler, J., and Kung, C. (1987). Pressure-sensitive ion channel in *Escherichia Coli*. *Proc Natl Acad Sci U S A* 84, 2297–2301.

- Martins, B.M.C., and Swain, P.S. (2011). Trade-Offs and Constraints in Allosteric Sensing. *PLOS Computational Biology* 7, e1002261.
- Marzen, S., Garcia, H.G., and Phillips, R. (2013). Statistical Mechanics of Monod-WymanChangeux (MWC) Models. *Journal of Molecular Biology* 425, 1433–1460.
- Michel, D. (2010). How transcription factors can adjust the gene expression flood-gates. *Progress in Biophysics and Molecular Biology* 102, 16–37.
- Milo, R., Jorgensen, P., Moran, U., Weber, G., and Springer, M. (2010). BioNumbers—the database of key numbers in molecular and cell biology. *Nucleic Acids Research* 38, D750–D753.
- Mishra, V., Skotak, M., Schuetz, H., Heller, A., Haorah, J., and Chandra, N. (2016). Primary blast causes mild, moderate, severe and lethal TBI with increasing blast overpressures: Experimental rat injury model. *Scientific Reports* 6, 26992.
- Monod, J., Wyman, J., and Changeux, J.-P. (1965). On the nature of allosteric transitions: A plausible model. *Journal of Molecular Biology* 12, 88–118.
- Murphy, K.F., Balázsi, G., and Collins, J.J. (2007). Combinatorial promoter design for engineering noisy gene expression. *Proceedings of the National Academy of Sciences* 104, 12726–12731.
- Naismith, J.H., and Booth, I.R. (2012). Bacterial mechanosensitive channelsMscS: Evolution’s solution to creating sensitivity in function. *Annu Rev Biophys* 41, 157–177.
- Oehler, S., Amouyal, M., Kolkhof, P., von Wilcken-Bergmann, B., and Müller-Hill, B. (1994). Quality and position of the three lac operators of E. Coli define efficiency of repression. *The EMBO Journal* 13, 3348–3355.
- O’Gorman, R.B., Rosenberg, J.M., Kallai, O.B., Dickerson, R.E., Itakura, K., Riggs, A.D., and Matthews, K.S. (1980). Equilibrium binding of inducer to lac repressor operator DNA complex. *Journal of Biological Chemistry* 255, 10107–10114.
- Perutz, M.F., and Mitchison, J.M. (1950). State of Hæmoglobin in Sickle-Cell Anæmia. *Nature* 166, 677–679.
- Phillips, R. (2015). Napoleon Is in Equilibrium. *Annual Review of Condensed Matter Physics* 6, 85–111.
- Phillips, R., Belliveau, N.M., Chure, G., Garcia, H.G., Razo-Mejia, M., and Scholes,

- C. (2019). Figure 1 Theory Meets Figure 2 Experiments in the Study of Gene Expression. *Annual Review of Biophysics* 48, 121–163.
- Poelwijk, F.J., Heyning, P.D., de Vos, M.G., Kiviet, D.J., and Tans, S.J. (2011). Optimality and evolution of transcriptionally regulated gene expression. *BMC Systems Biology* 5, 128.
- Raman, A.S., White, K.I., and Ranganathan, R. (2016). Origins of Allostery and Evolvability in Proteins: A Case Study. *Cell* 166, 468–480.
- Razo-Mejia, M., Boedicker, J.Q., Jones, D., DeLuna, A., Kinney, J.B., and Phillips, R. (2014). Comparison of the theoretical and real-world evolutionary potential of a genetic circuit. *Physical Biology* 11, 026005.
- Razo-Mejia, M., Barnes, S.L., Belliveau, N.M., Chure, G., Einav, T., Lewis, M., and Phillips, R. (2018). Tuning Transcriptional Regulation through Signaling: A Predictive Theory of Allosteric Induction. *Cell Systems* 6, 456–469.e10.
- Reynolds, K.A., McLaughlin, R.N., and Ranganathan, R. (2011). Hot Spots for Allosteric Regulation on Protein Surfaces. *Cell* 147, 1564–1575.
- Rogers, J.K., Guzman, C.D., Taylor, N.D., Raman, S., Anderson, K., and Church, G.M. (2015). Synthetic biosensors for precise gene control and real-time monitoring of metabolites. *Nucleic Acids Research* 43, 7648–7660.
- Rohlhill, J., Sandoval, N.R., and Papoutsakis, E.T. (2017). Sort-Seq Approach to Engineering a Formaldehyde-Inducible Promoter for Dynamically Regulated Escherichia coli Growth on Methanol. *ACS Synthetic Biology* 6, 1584–1595.
- Rydenfelt, M., Cox, R.S., Garcia, H., and Phillips, R. (2014a). Statistical mechanical model of coupled transcription from multiple promoters due to transcription factor titration. *Physical Review E* 89, 012702.
- Rydenfelt, M., Garcia, H.G., Cox, R.S., and Phillips, R. (2014b). The Influence of Promoter Architectures and Regulatory Motifs on Gene Expression in Escherichia coli. *PLoS ONE* 9, e114347.
- Salis, H.M., Mirsky, E.A., and Voigt, C.A. (2009). Automated design of synthetic ribosome binding sites to control protein expression. *Nature Biotechnology* 27, 946–950.
- Schatz, D.G., and Baltimore, D. (2004). Uncovering the V(D)J recombinase. *Cell* 116, S103–S108.

- Schatz, D.G., and Ji, Y. (2011). Recombination centres and the orchestration of V(D)J recombination. *Nature Reviews Immunology* 11, 251–263.
- Schmidt, A., Kochanowski, K., Vedelaar, S., Ahrné, E., Volkmer, B., Callipo, L., Knoops, K., Bauer, M., Aebersold, R., and Heinemann, M. (2016). The quantitative and condition-dependent *Escherichia coli* proteome. *Nature Biotechnology* 34, 104–110.
- Schumann, U., Edwards, M.D., Rasmussen, T., Bartlett, W., van West, P., and Booth, I.R. (2010). YbdG in *Escherichia Coli* is a threshold-setting mechanosensitive channel with MscM activity. *Proc Natl Acad Sci U S A* 107, 12664–12669.
- Scott, M., Klumpp, S., Mateescu, E.M., and Hwa, T. (2014). Emergence of robust growth laws from optimal regulation of ribosome synthesis. *Molecular Systems Biology* 10, 747–747.
- Setty, Y., Mayo, A.E., Surette, M.G., and Alon, U. (2003). Detailed map of a cis-regulatory input function. *Proceedings of the National Academy of Sciences* 100, 7702–7707.
- Sharan, S.K., Thomason, L.C., Kuznetsov, S.G., and Court, D.L. (2009). Recombi-neering: A homologous recombination-based method of genetic engineering. *Nat Protoc* 4, 206–223.
- Shis, D.L., Hussain, F., Meinhardt, S., Swint-Kruse, L., and Bennett, M.R. (2014). Modular, Multi-Input Transcriptional Logic Gating with Orthogonal LacI/GalR Family Chimeras. *ACS Synthetic Biology* 3, 645–651.
- Sivia, D., and Skilling, J. (2006). *Data Analysis: A Bayesian Tutorial* (OUP Oxford).
- Sochor, M.A. (2014). In vitro transcription accurately predicts lac repressor phenotype in vivo in *Escherichia coli*. *PeerJ* 2, e498.
- Soufi, B., Krug, K., Harst, A., and Macek, B. (2015). Characterization of the *E. coli* proteome and its modifications during growth and ethanol stress. *Frontiers in Microbiology* 6.
- Sourjik, V., and Berg, H.C. (2002). Receptor sensitivity in bacterial chemotaxis. *Proceedings of the National Academy of Sciences* 99, 123–127.
- Stokes, N.R., Murray, H.D., Subramaniam, C., Gourse, R.L., Louis, P., Bartlett, W., Miller, S., and Booth, I.R. (2003). A role for mechanosensitive channels in survival

of stationary phase: Regulation of channel expression by RpoS. *Proceedings of the National Academy of Sciences* 100, 15959–15964.

Swem, L.R., Swem, D.L., Wingreen, N.S., and Bassler, B.L. (2008). Deducing Receptor Signaling Parameters from In Vivo Analysis: LuxN/AI-1 Quorum Sensing in *Vibrio harveyi*. *Cell* 134, 461–473.

Thomason, L.C., Costantino, N., and Court, D.L. (2007). E. Coli Genome Manipulation by P1 Transduction. *Current Protocols in Molecular Biology* 79, 1.17.1–1.17.8.

Ursell, T., Phillips, R., Kondev, J., Reeves, D., and Wiggins, P.A. (2008). The role of lipid bilayer mechanics in mechanosensation. In *Mechanosensitivity in Cells and Tissues 1: Mechanosensitive Ion Channels*, A. Kamkin, and I. Kiseleva, eds. (Springer-Verlag), pp. 37–70.

van den Berg, J., Galbiati, H., Rasmussen, A., Miller, S., and Poolman, B. (2016). On the mobility, membrane location and functionality of mechanosensitive channels in *Escherichia Coli*. *Scientific Reports* 6.

Victorelli, S., and Passos, J.F. (2017). Telomeres and Cell Senescence - Size Matters Not. *EBioMedicine* 21, 14–20.

Vilar, J.M.G., and Leibler, S. (2003). DNA Looping and Physical Constraints on Transcription Regulation. *Journal of Molecular Biology* 331, 981–989.

Vilar, J.M.G., and Saiz, L. (2013). Reliable Prediction of Complex Phenotypes from a Modular Design in Free Energy Space: An Extensive Exploration of the lac Operon. *ACS Synthetic Biology* 2, 576–586.

Weinert, F.M., Brewster, R.C., Rydenfelt, M., Phillips, R., and Kegel, W.K. (2014). Scaling of Gene Expression with Transcription-Factor Fugacity. *Physical Review Letters* 113.

*Chapter 6***QUESTIONNAIRE**

Chap ter 7

CONSENT FORM